Structure and dynamics of filaments formed by bacterial cell division protein FtsZ on flat surfaces

Memoria presentada para optar al grado de Doctor en Ciencias Físicas por

Pablo Mateos Gil

Directora

Marisela Vélez Tirado

Instituto Universitario de Ciencias de Materiales Nicolás Cabrera

Facultad de Ciencias

Universidad Autónoma de Madrid

Enero de 2013

Jabberwocky

Twas brillig, and the slithy toves
Did gyre and gimble in the wabe;
All mimsy were the borogoves,
And the mome raths outgrabe.

'Beware the Jabberwock, my son!
The jaws that bite, the claws that catch!
Beware the Jubjub bird, and shun
The frumious Bandersnatch!'

He took his vorpal sword in hand:
Long time the manxome foe he sought-
So rested he by the Tumtum tree,
And stood awhile in thought.

And as in uffish thought he stood,
The Jabberwock, with eyes of flame,
Came whiffling through the tulgey wood,
And burbled as it came!

One, two! One, two! And through and through
The vorpal blade went snicker-snack!
He left it dead, and with its head
He went galumphing back.

'And hast thou slain the Jabberwock?

Come to my arms, my beamish boy!
O frabjous day! Callooh! Callay!'
He chortled in his joy.

'Twas brillig, and the slithy toves
Did gyre and gimble in the wabe;
All mimsy were the borogoves,
And the mome raths outgrabe.

'Through the Looking-Glass, and What Alice Found There'
Lewis Carroll

Galimatazo

Brillaba, brumeando negro, el sol;
agiliscosos giroscaban los limazones
banerrando por las váparas lejanas;
mimosos se fruncían los borogobios
mientras el momio rantas murgiflaba.

Cuidate del Galimatazo, hijo mío!
Guárdate de los dientes que trituran
Y de las zarpas que desgarran!
Cuidate del pájaro Jubo-Jubo y
que no te agarre el frumioso Zamarrajo!

Valiente empuñó el gladio vorpal;
a la hueste manzona acometió sin descanso;
luego, reposóse bajo el árbol del Tántamo
y quedóse sesudo contemplando...

Y así, mientras cavilaba firsuto.
Hete al Galimatazo, fuego en los ojos,
que surge hedoroso del bosque turgal
y se acerca raudo y borguejeando!!

Zis, zas y zas! Una y otra vez
zarandeó tijereteando el gladio vorpal!
Bien muerto dejó al monstruo, y con su testa
volvióse triunfante galompando!

Y hazlo muerto?! Al Galimatazo?!
Ven a mis brazos, mancebo sonrisor!
Qué fragarante da! Jujurujúu! Jay, jay!
Carcajeó, anegado de alegría.

Pero brumeaba ya negro el sol
agiliscosos giroscaban los limazones
banerrando por las váparas lejanas,
mimosos se fruncian los borogobios
mientras el momio rantas necrofaba...

'A través del espejo y lo que Alicia encontró al otro lado'
Traducción de Jaime Ojeda

Agradecimientos

Me gustaría agradecer el apoyo a todos mis compañeros del laboratorio, colaboradores y amigos que han estado conmigo a lo largo de éstos años que han supuesto mi trabajo de tesis.

En primer lugar quiero agradecer a mi directora de tesis, Marisela Vélez, la oportunidad de formar parte de su grupo de investigación y de iniciar este doctorado en su laboratorio. Su supervisión en el ámbito científico y académico as como su apoyo personal han sido imprescindibles para realizar este trabajo. De Marisela quiero destacar su visión integradora y multidisciplinar que nos ha permitido colaborar muy cercanamente con mundos tan alejados como la física teórica y la biología.

A continuación quiero agradecer a Germán Rivas y a la gente de su laboratorio, muy especialmente a Ariadna Martos, Mercedes Jiménez y Pilar López Navajas, por su paciencia y disposición a la hora de purificar las proteínas necesarias para ésta tesis y de resolver cualquiera de mis dudas. En éste aspecto, no me puedo olvidar de Jesús Mingorance y Estefanía Salvarelli de quienes he aprendido lo que sé sobre la actividad bioquímica de FtsZ.

Mi siguiente bloque de agradecimientos es para Pedro Tarazona y sus dos estudiantes de tesis durante estos años, Alfonso Paez e Ines Hörger. Gracias por tantas reuniones y discusiones sobre la modelización de los polímeros de FtsZ, por el desarrollo de las herramientas computacionales y por el análisis de tantas imágenes. Y gracias Pedro por haber podido compartir tu visión profunda de la física que subyace en los procesos dinámicos estudiados en ésta tesis. Para mi ha sido un verdadero placer poder colaborar con

vosotros.

Gracias a Pedro J. de Pablo, con quien di mis primeros pasos en el uso del AFM, y a toda la gente de *Nanotec*, Nacho, Luis, Adriana y Rafa, que siempre han estado ahí cuando les he necesitado. Gracias a Ilya Reviakine y Marta Gallego por ayudarme a mejorar mi manejo de la QCM, sin duda estaba un poco verde cuando fui a Donosti.

Por supuesto quiero agradecer a mis compañeros del día a día. A David, Ileana, Cristina, Santi, Mario, Julián y muy recientemente a Álvaro, por compartir (y aguantar) buenos y malos ratos en el laboratorio. A mi querida Paloma, te he echado mucho de menos éstos últimos años. A los antiguos compañeros del *Nicolás Cabrera*, Sara, Marta, Amanda, Bea y Alfonso, una pena que no pudiéramos seguir juntos después de que ambos laboratorios se trasladaran casi a la vez. A ése grupo selecto, Sotres, Alejandro, Brian, Merche y Alex, muchas comidas juntos y mucho apoyo al inicio de nuestras respectivas tesis. A los amigos en la distancia, Davide, Nati, Alex, Manuel, Julito, sé que estáis ahí aunque nos veamos poco. A todos los que no nombro, viejos y nuevos amigos, muchas gracias.

Por último a mis padres, lleváis toda la vida conmigo ayudándome y apoyándome. A mi hermano y a mi hermana. Álvaro gracias por todos los consejos y toda la ayuda que me has dado en ésto de la investigación científica. Y a ti Almudena gracias por el apoyo en todas las demás cosas que no son ciencia, que hay a que saber cuidar y que son igual o más importantes.

Resumen

Durante la década de 1950 el nacimiento de la biología estructural, con la resolución de la estructura de los primeros ácidos nucleicos y proteínas a nivel atómico, supuso un hito en el conocimiento de la *materia viva*. Sin embargo, entender los mecanismos subyacentes a los procesos celulares requiere no sólo una descripción atómica de sus componentes sino también conocer cómo éstos se ensamblan e interactúan entre si para realizar su función. Actualmente se sabe que una gran cantidad de procesos dinámicos suceden de forma simultánea en la célula. La expresión y la regulación genética, la generación de energía, el transporte de biomoléculas o la división celular, entre otros, son procesos necesarios para asegurar la supervivencia de la propia célula.

En ésta tesis hemos investigado el autoensamblaje de FtsZ, proteína principal de la maquinaria de división procariota. *In vivo*, FtsZ polimeriza en la cara interna de la membrana citoplasmática de la bacteria, formando un anillo dinámico (anillo Z) capaz de generar, al menos parcialmente, la fuerza necesaria para la división. *In vitro*, FtsZ retiene su capacidad para formar filamentos dinámicos en presencia de GTP. Éste trabajo de doctorado se centra en comprender la dinámica de los polímeros formados por FtsZ, desde su estructura más simple, i.e., protofilamentos aislados, hasta la formación de estructuras más complejas como agregados de filamentos y redes altamente entrecruzadas.

Trabajos previos han propuesto modelos sobre el comportamiento de los filamentos de FtsZ a partir de datos estructurales y dinámicos obtenidos de forma independiente mediante técnicas espectroscópicas y mediante micro-

scopia electrónica (EM). Nosotros hemos utilizado la microscopia de fuerza atómica (AFM) para obtener simultáneamente información dinámica y estructural de los filamentos de FtsZ adsorbidos en superficies planas. Ésta microscopia es capaz de registrar imágenes de alta resolución siendo posible distinguir protofilamentos individuales de FtsZ en tiempo real estando sumergidos en una disolución acuosa. El amplio polimorfismo estructural y el comportamiento dinámico observado experimentalmente se utilizó para formular modelos teóricos basados en las interacciones presentes entre los monómeros de FtsZ. Finalmente, un exhaustivo análisis estadístico y el uso de simulaciones computacionales revelaron aspectos clave del comportamiento dinámico de los filamentos de FtsZ.

La tesis está estructurada de la siguiente manera:

- La parte I es una introducción general que describe de forma breve el proceso de división bacteriana (capítulo 1) y la instrumentación utilizada durante el proyecto (capítulo 2).

- La parte II expone la estructura y la dinámica de filamentos de FtsZ sobre mica: desde protofilamentos individuales aislados (capítulo 3) hasta el comportamiento colectivo de muchos filamentos (capítulo 4).

- La parte III describe la formación de redes compuestas de filamentos cuando FtsZ polimeriza sobre bicapas lipídicas (capítulo 5).

- Al final se incluye unas conclusiones generales que integran y completan todo el trabajo.

En el capítulo 3 el estudio de filamentos individuales aislados de FtsZ reveló la relación entre la actividad GTPasa de FtsZ y la movilidad de la

proteína sobre la superficie con el mecanismo por el cual despolimerizan. Concluimos que la ruptura de los enlaces poliméricos entre dos monómeros de FtsZ sucede en posiciones aleatorias a lo largo del filamento y con una frecuencia correlacionada con la velocidad de hidrólisis del GTP. Además se identificaron tanto la movilidad en la superficie como el recambio de nucleótido como aspectos importantes para la nueva formación de enlaces poliméricos después de la hidrólisis del GTP.

El capítulo 4 estudia el comportamiento colectivo de muchos filamentos en términos de las interacciones presentes entre los monómeros de FtsZ. Se estimó cuantitativamente la energía del enlace longitudinal, la curvatura y la flexibilidad de los polímeros, y la energía de atracción lateral. Se encontró que estos cuatro parámetros en su conjunto son esenciales para explicar la dinámica y la estructura de los agregados de FtsZ experimentalmente.

En el capítulo 5 se describe cómo FtsZ sobre bicapas lipídicas dio lugar a la formación de redes altamente entrecruzadas. Las principales características de FtsZ, la ruptura y reformación de los enlaces longitudinales y la atracción lateral, siguen estando presentes en los entramados de filamentos formados. Se encontró que la composición lipídica de las bicapas modula la estructura de la redes, es decir, su curvatura, altura y grado de entrecruzamiento.

Para terminar, quiero resaltar que éste trabajo ha supuesto un esfuerzo multidisciplinar en el que han participado biólogos, físico-químicos y físicos teóricos. Las distintas contribuciones necesarias para llevar a cabo éste proyecto se describen a continuación:

- La purificación de las proteínas y caracterización de su actividad

bioquímica [1].

- El diseño experimental. La preparación de superficies y la reconstitución del sistema modelo de membrana. Los experimentos de AFM y QCM. El análisis de imágenes y datos [2].

- La modelización de los resultados experimentales y el desarrollo de las herramientas computacionales para la simulaciones de Monte Carlo (MC) y las simulaciones de Languevin. La segmentación de los protofilamentos individuales y el análisis estadístico de los datos [3].

[1] Ésta parte del trabajo se llevó a cabo en el laboratorio de Germán Rivas (Centro de investigaciones biológicas, CSIC. Madrid, Spain) y en el laboratorio de Jesús Mingorance's (Hospital universitario La Paz. Madrid, Spain)

[2] Se debe considerar ésta parte del trabajo como la contribución original de doctorando y fue realizada en el laboratorio de Marisela Vélez (dirección antigua, Instituto Nicolás Cabrera, UAM. Madrid, Spain. Dirección actual Instituto de Catálisis y Petreoloquímica, CSIC. Madrid, Spain)

[3] Ésta parte del trabajo se llevó a cabo en el laboratorio del Profesor Pedro Tarazona (Facultad de Ciencias, UAM. Madrid, Spain)

Summary

Irruption of structural biology during the 1950s, establishing the atomic structure of nucleic acids and proteins, constituted a turning point in the knowledge of *living matter*. However, understanding the mechanisms underlying cell processes requires not only an atomistic description of their isolated components but also knowledge about how they interact and assemble to carry out their functions. Nowadays it is well known that a multitude of dynamic processes occur simultaneously inside a cell. Genetic expression and regulation, energy generation, trafficking of biomolecules or cell division, among others, are essential to ensure cell viability.

In this thesis we have investigated the self-assembly of FtsZ, a main protein in prokaryotic cell division machinery. *In vivo*, FtsZ polymerizes on the inner face of bacterial cytoplasmic membrane forming a dynamic ring (the Z-ring) able to generate, at least partially, the force necessary for cell division. *In vitro*, FtsZ retains its capacity to form dynamic filaments in the presence of GTP. This PhD work is focused on understanding the dynamics of FtsZ from its simplest form, i.e. isolated filaments, to the formation of higher order structures such as filament aggregates and highly interconnected networks.

Previous works have proposed models for FtsZ filaments from dynamic and structural experimental data obtained separately with spectroscopic techniques and electron microscopy (EM). In contrast, we have used an atomic force microscope (AFM) to obtain simultaneously the structure and dynamics of FtsZ filaments adsorbed on flat surfaces. This microscopy is able to acquire high resolution images discerning the structure of FtsZ

single protofilaments in real time under buffer solution. The rich structural polymorphism and dynamic behavior observed experimentally were used to formulate theoretical models in terms of interactions between FtsZ monomers. Finally, statistical analysis and computational simulations revealed key quantitative aspects of the dynamic behavior of FtsZ filaments.

The thesis is structured as followed:

- Part I is of a general introduction describing briefly the bacterial cell division process (chapter 1) and the instrumentation used in the project (chapter 2).

- Part II reports the structure and dynamics of FtsZ filaments on mica: from single isolated protofilaments (chapter 3) to the collective behavior of many filaments (chapter 4).

- Part III describes the formation of filament networks when FtsZ polymerizes on lipid bilayers (chapter 5).

- At the end general conclusions were include to integrate and complete the whole work.

In chapter 3 the study of single isolated FtsZ filaments revealed the relationship between FtsZ GTPase activity and protein surface mobility with its depolymerization mechanism. We conclude that rupture events of the polymeric bonds between FtsZ monomers occur at random locations along the filament and their frequencies correlates with GTP hydrolysis rate. Protein surface mobility and nucleotide turnover were also identified as relevant for reannealing of polymeric bonds after GTP hydrolysis.

Chapter 4 looks at the collective behavior of many filaments in terms of FtsZ monomer-monomer interactions. Quantitative values for longitudinal bond energy, polymer curvature and flexibility, and lateral attraction were given. These four parameters were found as the essential traits to account for the structure and dynamics of FtsZ aggregates observed experimentally.

In chapter 5, we found that the polymerization of FtsZ on lipid bilayers leads to the formation of highly interconnected networks. The main dynamic features of FtsZ filaments, rupture and reannealing of longitudinal bonds and lateral attraction, were still present in the meshes formed. Lipid composition of the bilayer was also found to modulate the structure of the networks, affecting their curvature, height, and connectivity.

To conclude, I want to remark that this work has been a multidisciplinary effort involving biologists, physical-chemists, and theoretical physicists. The different contributions necessary during the project are described as followed:

- Protein purification and characterization of their biochemical activity [1].

- Experimental design. Surface sample preparations and membrane model system reconstitution. AFM and QCM measurements. Image and data analysis [2].

[1] This part was carried out at Germán Rivas' laboratory (Centro de investigaciones biológicas, CSIC. Madrid, Spain) and at Jesús Mingorance's laboratory (Hospital universitario La Paz. Madrid, Spain)

[2] This part must be consider the original contribution of the PhD student and it was carried out at Marisel Vélez's laboratory (past address Instituto Nicolás Cabrera, UAM. Madrid, Spain. Present address Instituto de Catálisis y Petreoloquímica, CSIC. Madrid, Spain)

- Modeling of experimental results and implementation of computational tools for Monte Carlo (MC) and Languevin simulations. Single protofilaments segmentation and statistical data analysis [3].

[3]This part was carried out at Professor Pedro Tarazona's laboratory (Facultad de Ciencias, UAM. Madrid, Spain)

Publications

- P. López-Navajas, G. Rivas, J. Mingorance, P. Mateos-Gil, I. Hörger, E. Velasco, P. Tarazona, and M. Vélez, "*In vitro* reconstitution of the initial stages of the bacterial cell division machinery.," *J Biol Phys*, vol. 34, pp. 237-247, 2008.

- A. Paez, P. Tarazona, P. Mateos-Gil, and M. Vélez, "Self-organization of curved living polymers: FtsZ protein laments," *Soft Matter*, vol. 5, no. 13, pp. 2625-2637, 2009.

- A. Paez, P. Mateos-Gil, I. Hörger, J. Mingorance, G. Rivas, M. Vicente, M. Vélez, and P. Tarazona, "Simple modeling of FtsZ polymers on flat and curved surfaces: correlation with experimental *in vitro* observations.," *PMC Biophys*, vol. 2, no. 1, p. 8, 2009.

- P. Mateos-Gil, I. Marquez, P. López-Navajas, M. Jiménez, M. Vicente, J. Mingorance, G. Rivas, and M. Vélez, "FtsZ polymers bound to lipid bilayers through ZipA form dynamic two dimensional networks.," *Biochimica et Biophysica Acta-biomembranes*, vol. 1818, pp. 806-813, Mar. 2012. [1]

- I. López-Montero, P. Mateos-Gil, M. Sferrazza, P. L. Navajas, G. Rivas, M. Vélez, and F. Monroy, "Active membrane viscoelasticity by the bacterial FtsZ division protein.," *Langmuir*, vol. 28, pp. 4744-4753, Mar 2012.

[1] Chapter 5 of this thesis is the accepted version of the paper.

- P. Mateos-Gil, A. Paez, I. Hörger, G. Rivas, M. Vicente, P. Tarazona, and M. Vélez, "Depolymerization dynamics of individual filaments of bacterial cytoskeletal protein FtsZ., *Proc Natl Acad Sci USA*, vol. 109, pp. 8133-8138, May 2012. [2]

[2]Chapter 3 of this thesis is the accepted version of the paper

Contents

List of Figures

List of Tables

List of abbreviations

AFM	Atomic force microscopy
CA	Cardiolipin (*E. coli*)
DOGS-NTA	1,2-dioleoyl-sn-glycero-3-[(N-(5-amino-1-carboxypentyl)iminodiacetic acid)succinyl] (nickel salt)
EcPL	*E. coli* Polar Lipid Extract
EPC	L-α-phosphatidylcholine (Egg, Chicken)
GDP	Guanosine 5'-diphosphate
GMPCPP	Guanosine-5'-[(α,β)-methyleno]diphosphate
GTP	Guanosine 5'-triphosphate
MC	Monte Carlo
PE	L-α-phosphatidylethanolamine (*E. coli*)
PG	L-α-phosphatidylglycerol (*E. coli*)
QCM	Quartz crystal microbalance
SLB	Supported Lipid bilayer
Tris-HCl	Tris(hydroxymethyl)aminomethane hydrochloride

Part I

Introduction

Chapter 1

General Introduction

In this chapter we will overview the prokaryotic cell division process. In the first section cell division stages and the components of cell division machinery are presented. In the following section we will focus on FtsZ, the main component of the division machinery that forms the so called Z-ring and responsible, at least partially, to generate the force necessary to cell division. At the end of the chapter we present the objectives of the thesis

1.1 Bacterial cell division

1.1.1 Cell division stages

In bacteria, the division occurs as a binary fission comprising different steps (figure 1.1). It begins with the replication of genetic information contained in a unique chromosome, a DNA condensed structure known as nucleoid (step 1). Simultaneously, cell elongates and both chromosome replication origins (oriC) migrate towards the cell poles (step 2). When the two daughter nucleoids are fully segregated, FtsZ protein assembles on the inner face of the cytoplasmic membrane at the cell center, forming the so-called Z-ring (step 3). During step 4 other membrane-associated proteins essential for cell division are recruited to the cell midpoint forming the bacterial cell division machinery. At this stage the contraction of the Z-ring and the con-

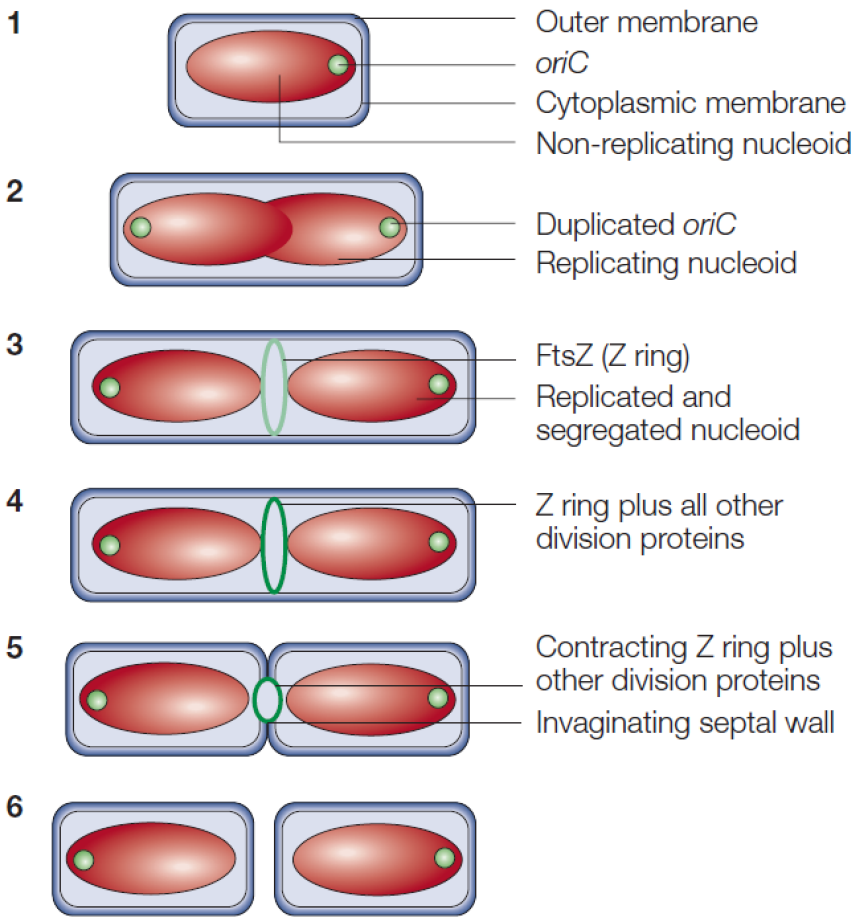

Figure 1.1 – Cell division stages in *E. coli*. Schematic illustration of cell division stages in *E. coli*. Adapted from [1]

striction of the cell membrane lead to the rupture of the parental cell into two newborn daughter cells.

The division process is spatially and temporally regulated. The localization of division machinery at the cell center and a fully DNA replication and segregation is necessary to ensure the viability of the newborn cells. Two regulatory mechanisms, the MinCDE system and nucleoid occlusion, prevents the FtsZ assembly at the cell poles and the polymerization close to the nucleoid [1].

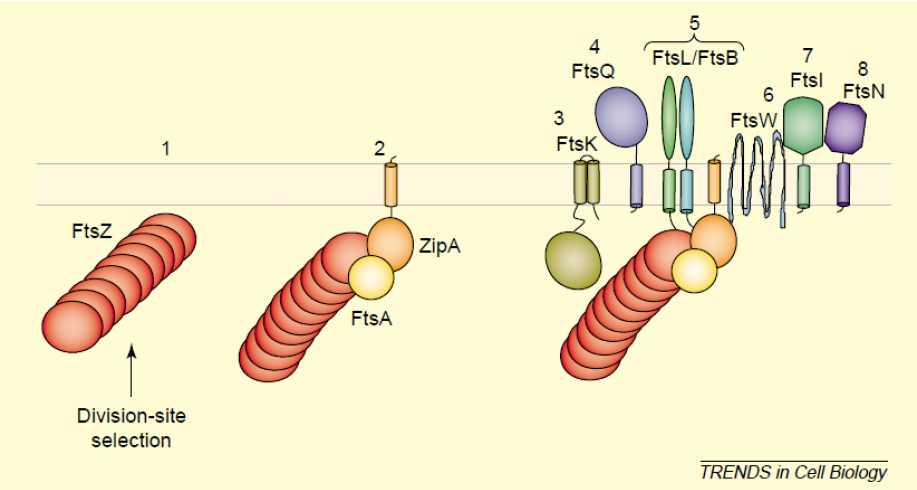

Figure 1.2 – Schematic cartoon of the components of cell division machinery in *E.coli*. (1) shows FtsZ polymers at the division site. (2) shows FtsZ polymer anchored to the cytoplasmic membrane by FtsA and ZipA. (3) shows the whole division machinery components comprising ten essential membrane associated proteins. Adapted from [2]

1.1.2 Cell division machinery: the components and their assembly

The division cell machinery, the divisome, in *E. coli* is a complex molecular machine that comprises at least 10 membrane-associated, both cytoplasmic and periplasmic, proteins (a cartoon is shown in figure 1.2).

FtsZ is the main component of the divisome. It is conserved through the majority of bacteria and it is also present in chloroplast and mitochondria. It polymerizes on the inner face of cytoplasmic membrane forming the so-called Z-ring but FtsZ filaments are not bound directly to cell membrane. In *E. coli* its anchoring is mediated by two proteins, FtsA and ZipA [3]. Initially, FtsZ, ZipA and FtsA assemble simultaneously at the midpoint of the bacteria to form the proto-ring, followed by the assembly of FtsK to form the cytoplasmic ring. The rest of proteins: FtsQ, FtsB and FtsL form a periplasmic connector; FtsW and FtsI are involved in peptidoglycan synthesis during the cell division; and FtsN assemble in a later stage. It has been shown that, in spite of a strictly linear order, assembly of later proteins might occur in the absence of early components of division machinery such as FtsA [4] (see figure 1.3).

All of these proteins are essential to the functionality of the divisome. The absence of one of them would disrupt the cell division leading to the formation of bacterial filaments formed by many cells one beside each other but not separated.

1.2 Bacterial cell division protein FtsZ

The main interest of this thesis is the structure and dynamics of FtsZ filaments. In this section we overview the fundamental aspects of FtsZ. We will introduce the structure of FtsZ monomer as the prokaryotic ancestor of tubulin, its ability to bind and hydrolyze GTP, its polymeric structure and dynamics. Finally two force generating mechanisms based on FtsZ will be summarized.

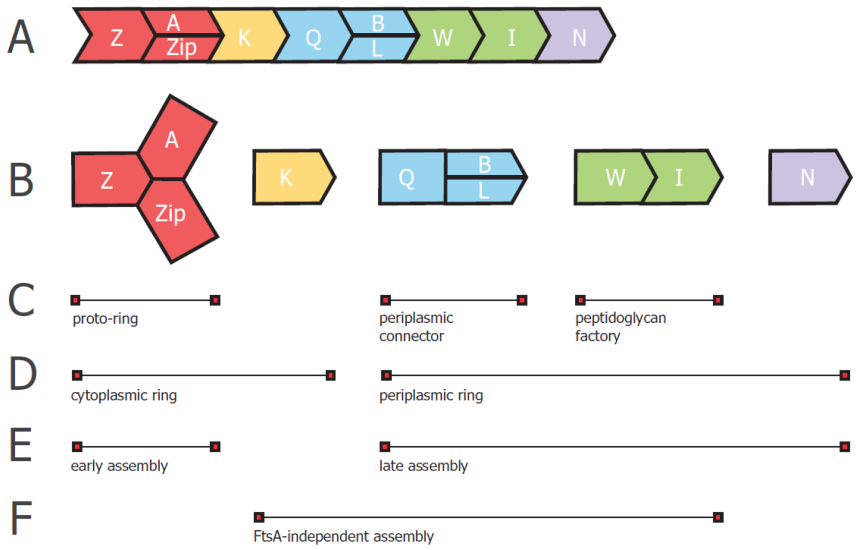

Figure 1.3 – Assembly of cell division machinery components in *E. coli*. A strictly linear sequence (A) or a concerted assembly (B) have been proposed. A proto-ring formed by FtsZ, ZipA and FtsA assembles in the inner face of cytoplsamic membrane constituted an early assembly of the division machinery (C, D an E). The periplasmic ring composed by a periplasmic connector and peptidoglycan factory assemble later (C,D and E). Late assembly events might occur in the absence of FtsA (F). Fts was omitted from Fts protein names and Zip=ZipA. Adapted from [4]

1.2.1 FtsZ-The GTPase ancestor of tubulin

FtsZ is a prokaryotic homologue of tubulin. Despite the low sequence homology between FtsZ and tubulin, the three-dimensional structure solved for FtsZ of *Methanococcus Jannaschii* revealed that both proteins shared the same fold[5]. The globular structure of FtsZ consists in two domains divided by a central helix (see figure 1.4 A), the N-terminal domain that binds GTP and the C-terminal domain containing specific binding sequence to other proteins like ZipA or FtsA.

As tubulin, FtsZ binds and hydrolyzes GTP. The active GTP pocket is formed between the interfaces of two FtsZ monomers associated in a head-to-tail manner (see figure 1.4 B). The insertion of the T7 loop from the base of one subunit into the nucleotide-binding site of the subunit below catalyzes the GTP hydrolysis.

In vitro, subunit assembly of FtsZ and its hydrolysis activity depends on the binding of nucleotide, the pH and the cations present in the buffer solution[6–9]. In the presence of GDP and Mg^{+2} FtsZ forms short oligomers[10]. Upon addition of GTP, Mg^{+2} and K^{+} FtsZ polymerizes and the polymers hydrolyze GTP. In the presence of non-hydrolyzing analogues of GTP, such as GMPCPP and GDP-AlF_3, FtsZ still forms filaments indicating that the polymerization depends on nucleotide binding but not on nucleotide hydrolysis[11,12].

1.2.2 Structure of FtsZ polymers and aggregates

What is the basic structure of FtsZ polymers? was the first question about the polymeric structure of FtsZ. Initially, electron microscopy images showed multistranded filaments with different widths[13]. Following work discerned single-stranded protofilaments 5 nm width[14]. Nowadays, it is widely accepted that FtsZ assembles into single stranded protofilaments with a high tendency to aggregate laterally depending on the polymerization conditions (see figure 1.5).

FtsZ and tubulin differ in their lateral interactions to form higher-order structures. Tubulin forms microtubules, tubes comprising thirteen protofilaments, but FtsZ protofilaments associate preferentially in one monomer thick structures. Conditions promoting the lateral aggregation of FtsZ are Ca^{+2}, acidic pH, interaction with other division proteins like ZipA, or the presence of crowding agents leading to the formation of networks, bundles, ribbons, sheets, spirals, and toroids[15–19] (see figure 1.5).

What is the curvature of FtsZ protofilaments? has been also a central question on the polymeric structure of FtsZ. During the year 2000, small rings and straight filaments were observed in the presence of GDP and GTP respectively, suggesting a switch between straight and curved conformation associated with a GTP- and GDP-bound state of FtsZ[20]. In 2005, AFM images under buffer solution showed that FtsZ filaments can modulate their conformation and curvature depending on the environment[12]. A highly packed arrangement of straight and parallel filaments was observed for a high protein surface density. As surface coverage decreased filaments explore other conformations, curving gently , and forming rolled aggregates. Whether GTP- and GDP-bound states of FtsZ lead to different curvatures

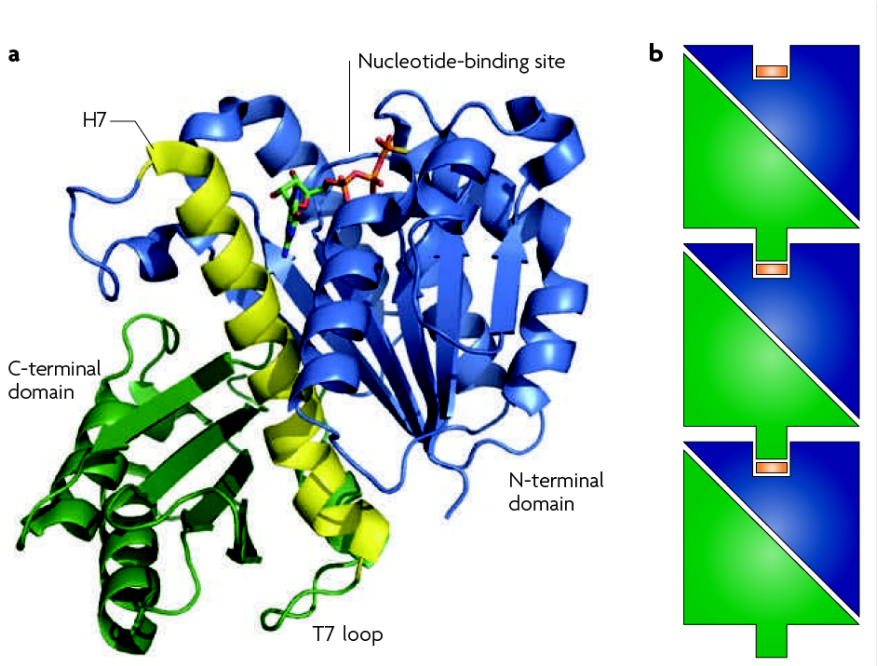

Figure 1.4 – FtsZ monomeric and polymeric structure. (A) Crystal structure of *Bacillus subtilis* FtsZ monomer bound to GTP-γS. FtsZ is composed of two domains separated by a central helix (H7). The amino-terminal domain (blue) contains the nucleotide-binding site. The T7 loop responsible of catalyze the nucleotide hydrolysis is in the carboxy-terminal domain (green), following H7. The extreme C-terminal tail, which forms the binding site for several division proteins, is not visible in the crystal structure. (B) FtsZ polymerizes by the head-to-tail association of individual subunits, shown in blue and green, to form a single-stranded protofilament. Adapted from[3]

between FtsZ subunits is still under discussion.

How FtsZ protofilaments arrange *in vivo* to form the Z-ring is not known yet.

1.2.3 Dynamics of FtsZ polymers

Both, GTP binding and hydrolysis, and nucleotide exchange affect FtsZ dynamics. However the relationship between FtsZ dynamics with its polymeric structure and biochemical activity is not fully understood.

How does FtsZ polymerize? In the presence of GDP FtsZ forms short oligomers[10,22]. In contrast, the formation of FtsZ filaments in solution upon addition of GTP and GMPCPP (a non-hydrolyzing GTP analogue) indicates that FtsZ polymerization is dependent on nucleotide binding but not on its hydrolysis. A critical protein concentration around 1 μM[23,24] is required for FtsZ polymerization in solution, indicating a

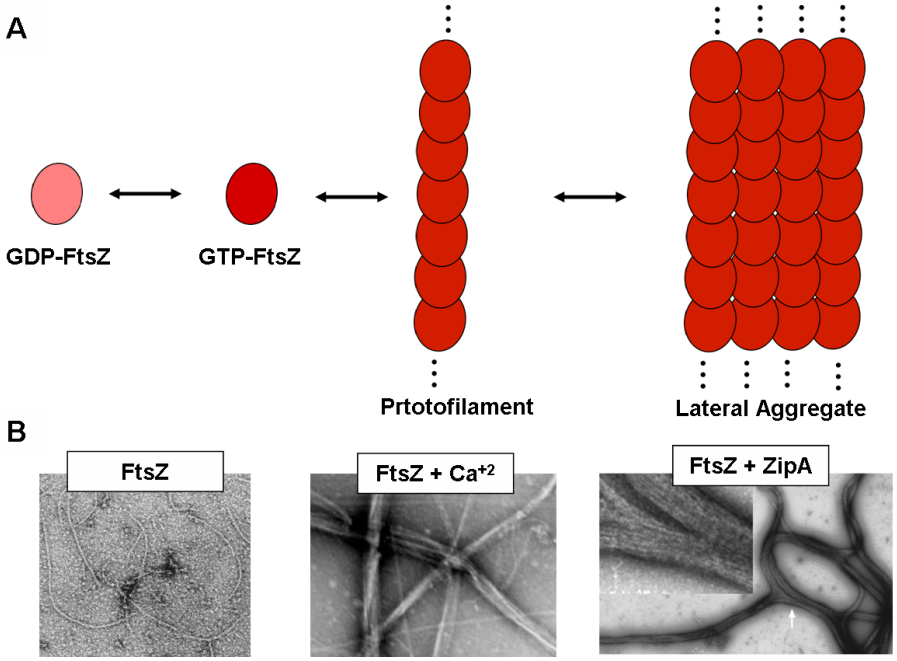

Figure 1.5 – FtsZ polymerization and lateral aggregation. (A) illustrates the assembly of FtsZ subunits into protofilaments that aggregate laterally. (B) shows EM images of FtsZ protofilaments (left) and lateral aggregates formed in presence of Ca^{+2} (center) or ZipA (right). Adapted from[14,17,21].

cooperative assembly of FtsZ subunits. Simultaneous formation of longitudinal and lateral contacts leading to multistranded filaments accounts for cooperative polymerization but is contradicted by EM and AFM images showing single-stranded filaments. Models involving preferential cyclation, allosterism, or activation of a FtsZ dimer nucleus have been proposed to explain cooperative assembly of single-stranded protofilaments[23,25,26].

What is the depolymerization mechanism of FtsZ filaments? It is well known that both nucleotide turnover and reduced GTPase activity stabilize the FtsZ polymers. Polymers formed upon addition of GTP can be stabilized including a GTP-regeneration system in the buffer solution[27] and polymerization with GMPCPP instead of GTP also increases the lifetime of the filaments[12]. On the other hand, GDP promotes a fast filament disassembly competing with the GTP to bind between FtsZ subunits[27]. However, different questions are still open to understand FtsZ dynamic behavior related with its GTPase activity (see figure 1.6 A)

- **What is the nucleotide content in FtsZ polymers?**...Is it segregated or not?
- **How does GTP hydrolysis occur along the filaments?**...Does it occur randomly at different monomer-monomer interfaces or is it directional?
- **How does the nucleotide turnover occur along the filament?**... Does it occur only in the free monomers or can it take place along the filament?

Microtubules (MTs) dynamics is an example of how these factors determine polymer stability and depolymerization (see figure 1.7). Growing MTs incorporate GTP-bound tubulin to its plus end and nucleotide hydrolysis occurs from its minus to its plus end, resulting in a segregated nucleotide content. In addition, the different stability of GDP-bound and GTP-bound tubulin in the MTs, less and more stable respectively, is responsible of rapid shrinking events. If polymerization rate is faster than hydrolysis rate, then the plus end will have a GTP cap that stabilizes the polymeric structure. In contrast, if GTP hydrolysis is more rapid than the addition of new GTP-tubulin subunits, the absence of a GTP cap will lead to a fast depolymerization. In this case the high content of GDP in the filaments constitutes a mechanism to store energy from each phosphorylation and release it afterward when MTs shrinks.

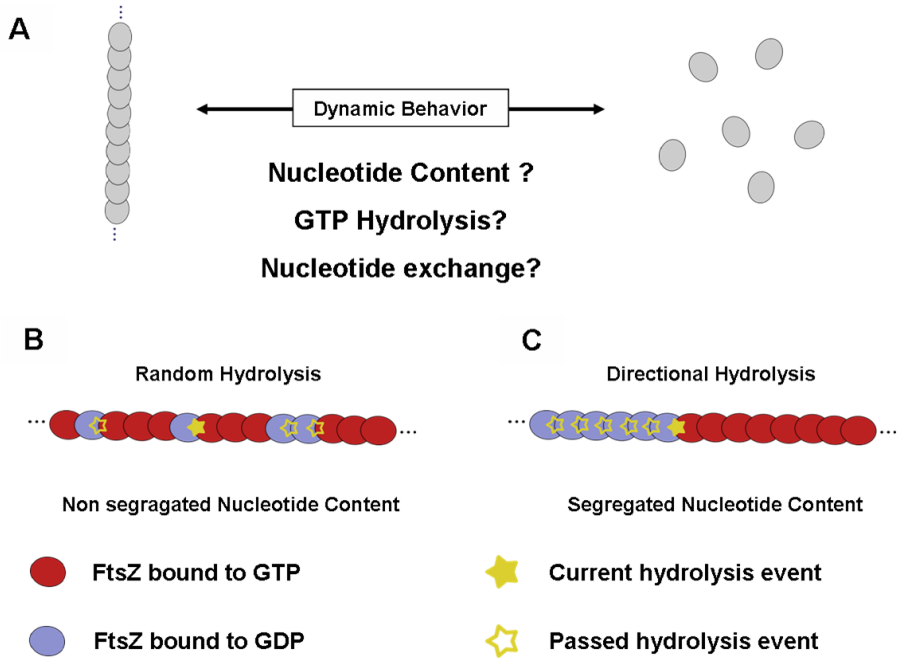

Figure 1.6 – Open questions for FtsZ dynamics. Questions about FtsZ dynamic and its hydrolysis activity.

In contrast to MTs, previous works have measured a high GTP:GDP ratio within FtsZ filaments, ranging from 100:0 to 50:50 [22,27–29]. Three possibilities have been proposed for nucleotide turnover location: (i) throughout the polymer [27] (ii) at the free ends of the polymer, and (iii) in free FtsZ monomers [29]. And recently data suggest that GTP hydrolysis occur independently at each FtsZ monomer-monomer interface [30].

1.2.4 FtsZ *in vivo*

What is the structure of Z-ring? *In vivo*, FtsZ polymers anchored to the inner face of the cytoplasmic membrane by FtsA and ZipA form the so-called Z-ring observed as a closed circle by conventional fluorescence microscopy. Recent data with photoactivated light microscopy (PALM) with spatial resolution of $\sim 35\ nm$ beyond the diffraction limit have discerned also helical structure indistinguishable from closed ring structure with conventional fluorescence microscope [31]. The arrangement of FtsZ filaments inside the Z-ring is still under discussion. One possibility would be an arrangement where FtsZ subunits were connected head-to-tail embracing 2-3

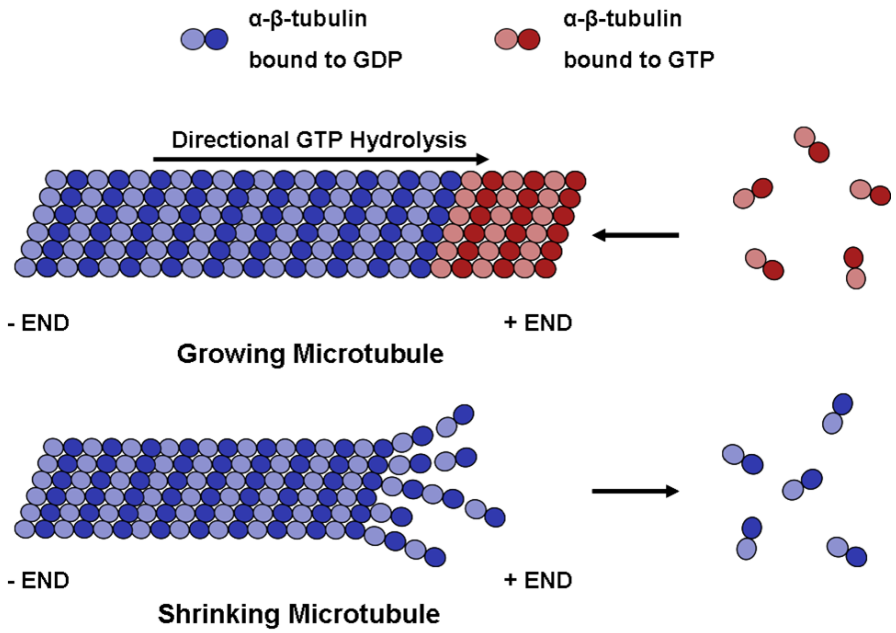

Figure 1.7 – Microtubule dynamic instability. Schematic cartoon of microtubule's dynamic instability

times the waist of the bacteria with the protofilaments tightly aligned, this would lead to a width $\sim 20 - 30$ nm. However, the width of the Z-ring measured by PALM (~ 110 nm) suggests that FtsZ filaments are loosely aligned forming a thicker structure. Whether the Z-ring is formed by short or longer filaments continuously connected is also under discussion.

What are the force generation mechanisms based on the Z-ring? In contrast to eukaryotes, in bacteria no protein motors have been found to provide the force necessary for cell division. It is widely accepted that FtsZ filaments in the Z-ring generates, at least partially, the force needed for cell division. This assumption is supported by recent experiments in membrane model systems where FtsZ alone deforms the lipid membrane of tubular liposomes (see following section).

There are two different models for how the Z-ring itself generates the constriction force necessary for cell division. One is based on filament bending associated with the nucleotide-bound state of FtsZ. The angle between two FtsZ monomers has been reported to be around 0°-3° for GTP bonds and 22° for GDP bonds[32]. In this model, the force will be generated by an increase in the filament curvature as GTP is hydrolyzed. The second model is based on lateral bonds between FtsZ filaments inside the Z-Ring.

For a fixed number of proteins a smaller Z-ring would increase the number of lateral contacts between FtsZ filaments. These models are not mutually exclusive and both may play an important role during the cell division.

1.2.5 FtsZ on membrane model systems

In vitro, membrane model systems have been recently used to study FtsZ assembly. Whereas FtsZ does not anchor directly to the lipid membrane, different approaches have been used to reconstitute FtsZ onto lipid membranes. A modified FtsZ fused with a membrane attachment-helix inserts into the lipid membrane. This protein assembles forming rings and partially deforming the lipid membrane of tubular liposomes, supporting the hypothesis that FtsZ by itself generates a contractile force[33]. A different strategy uses ZipA, a natural anchoring protein of the proto-ring in *E. coli*, to tether FtsZ to a supported lipid bilayer on mica. In this case FtsZ bundles assemble onto the flat bilayer. It was found that lipid composition had a major impact on aggregate structure[34].

1.3 Objectives of the thesis

In 2005 FtsZ filaments were visualized by atomic force microscopy (AFM) on mica. This work constituted the first report where the dynamics of FtsZ was directly related with its polymeric structure. Fragmentation and reannealing of longitudinal bonds, preferential curvature and lateral aggregation were identified as relevant features of single-stranded protofilaments of FtsZ exhibiting a rich structural polymorphism. In contrast, previous works have studied separately the structure and dynamics of FtsZ filaments by electron microscopy (EM) and spectroscopic techniques.

The main objective of this PhD thesis extends the approach of characterizing structure and dynamics of FtsZ polymers on flat surfaces a little further. From the collective dynamics of FtsZ filaments on mica as a starting point, two opposite directions were followed. One direction was simplifying the system, i.e. from filament aggregates to isolated polymers, on mica. The second direction was increasing the complexity of the system by the reconstitution of FtsZ onto supported lipid bilayers (SLBs) containing ZipA, a natural anchor protein present in the *E. coli* division machinery.

1.3.1 Specific objectives

- **Characterization of single FtsZ protofilaments on mica.** We isolated single stranded FtsZ protofilaments on mica to avoid the formation of lateral aggregates. We studied the dynamics, stability and depolymerization of the isolated polymers.

- **Study the role play by nucleotide binding and hydrolysis on FtsZ protofilaments stability and depolymerization**. The effect of nucleotide content in the buffer was explored. GTP and its nonhydrolyzing analogue GMPCPP were used to modulate nucleotide hydrolysis of FtsZ. Acid buffers were also used to reduce nucleotide hydrolysis and glycerol was used to reduce surface protein mobility.

- **Quantitative estimation of the basic traits involved in FtsZ protofilaments aggregation.** The polymorphism of FtsZ filaments observed at different surface coverages by AFM was compared with Monte Carlo (MC) simulations including a labile longitudinal bond energy, its curvature and flexibility, and a lateral attractive energy.

- **Study the effect of FtsZ attachment to a lipid bilayer on the structure and dynamics of FtsZ polymers.** SLBs with different lipid composition were prepared on flat solid substrates. FtsZ was specifically anchored to the lipid membranes through a soluble his-tagged ZipA construct (sZipA) previously attached to the bilayer through chelating lipids. Finally, we triggered the polymerization of FtsZ upon GTP addition and we evaluated the effect of lipid composition on the structures formed.

Chapter 2

Instrumentation

2.1 Atomic Force Microscopy (AFM)

2.1.1 AFM in biology

Atomic force microscopy (AFM) belongs to the family of scanning probe microscopes (SPM), capable of registering topography, electric density, mechanical properties (young modulus) or other surface properties at the nanometer scale. Since the development of the scanning tunneling microscope (STM) in 1982[35], the first member of SPM family and a predecessor of AFM, a revolution in the study of material surfaces has occurred. In this section we review the historical origin and developments of AFM, in particular few applications in biology. Finally, we will focus in the use of AFM to study dynamic processes, very similar to the aim of this thesis, where biological macromolecules were observed in real-time under buffer solution.

The STM exploits the exponential dependence of tunneling electric current across the gap between a conductor (or semiconductor) tip and a conductor (or semiconductor) surface, with the distance between the tip and the surface. This feature of the STM was used to study metal surfaces, allowing subnanometric surface resolution of gold and indeed the visualization of atoms[36]. Despite the effort to obtain topographical images of biological molecules[37], it was the invention of the atomic force microscopy in 1986[38] that opened the door to study biological molecules. Instead of the tunneling electric current used by STM, the AFM is based on the force present be-

tween a sharp tip (the probe) and a surface (the sample). This force is the total result of different contributions (for instance Van der Walls, hydration and electrostatic forces) and has a strong dependence with the tip-surface distance. AFM bypassed the limitation of STM to study only metallic samples, being used to measure non-conducting samples in air and liquid. Very soon first images of biological molecules were obtained in air[39]. In 1987, the first AFM images of surfaces immersed in liquid[40] broke the barrier to study biological samples fully hydrated under physiological conditions and even molecules in action. During the 90s advances in technology, sample preparation protocols, and better understanding of the sample-tip interaction, in addition to the availability of commercial setups popularized and extended the use of AFM all over the world.

There are two main applications of atomic force microscopy in biology: imaging and force spectroscopy. The AFM can be used to visualize at single molecule level, not only the topography of biomolecules, but also other features like electrostatic density or mechanical properties of the sample. High resolution imaging achieved for first time on 2D membranes protein crystals[41] and extensively used to study protein structure and conformational changes at submolecular level related with its function[42–44]. It provides complementary information to X-ray crystallography and electron microscopy in structural biology. Mechanical information, such as elasticity or stiffness, obtained by AFM is complementary to other techniques like optical tweezers, micropipette manipulation, or flow chamber developed for measuring forces. Probing samples at the nanometer scale allows local mapping of forces of lipid membranes, viruses and microtubules[45–47] relating mechanics with structural and functional data. The other AFM application is force spectroscopy, where the force vs. the tip-sample distance is registered. This characteristic of the AFM has been used to study intra-molecular and inter-molecular interactions, leading to new insights in unfolding and refolding of proteins[48,49] and providing mechanical energy landscape of ligand-receptor interactions[50].

Using the AFM to visualize molecules at work in real-time has been particularly interesting for the aim of this thesis. Recording videos following the same area to observe DNA-protein interaction, molecular motors as myosin, and fibril dynamics[51–53] has allowed to correlate chemical reactions with structural information, such as DNA bending, conformational changes, polymerization, curvature changes, and fibril branching respectively. Fine sample preparation, where the molecules are adsorbed gently enough on the surface to be functional and free to lateral diffuse, is necessary to get

reliable dynamic data, adjusting ionic strength and pH may help to this purpose. Limitation in image acquisition velocity has been an essential barrier to these dynamical studies. The time needed to take one image, in the range of minutes, determines which processes are accessible to be studied. High speed AFM prototypes have been developed since 90s and nowadays it is possible to find commercial setups (for a review in the history and development of high speed AFM see[54]). Lapsed time in the range of seconds between images will allow the study of faster processes.

To conclude, the future of AFM is plenty of new possibilities and developments. To visualize single molecules at work, improvements in sample preparation protocols, and new cantilevers to limit sample damage and improve spatial resolution, are still necessary. To study more complex multi-components systems it would be desirable to obtain topographical and chemical information simultaneously. Instrumentation advances, combining regular AFM with Raman spectroscopy or with new fluorescence microscopes able to resolve particles beyond the diffraction limit, could be a solution.

2.1.2 AFM Measurement principles

In this section we will introduce the atomic force microscope setup. We will see the different parts on an AFM and a brief summary of the principles underlying the measurement process. Finally we will explain how samples were prepared to be visualized under buffer solution.

Atomic Force Microscope setup

Figure 2.1 A shows a diagram of the AFM parts: a mechanical module where the sample is physically scanned, an electronic box, and a PC controller with a digital signal processing card (DSP). A piezoelectric positioner allows on plane (XY) and vertical (Z) displacements of the sample at subnanometer scale while a sharp tip attached to a flexible micro-cantilever is probing the surface. To measure the force between the tip and the surface, the micro-cantilever behaves as a spring being deflected upward or downward for repulsive and attractive forces respectively. The electronic box receives the deflection signal, registered on a photodiode by measuring the reflection of a laser on the cantilever, and the position of the sample controlled by the piezotube. Finally, a computer processes the signals received by the

electronics and establishes a feedback control, adjusting the Z-position of the sample to keep the force at a constant value in the case of *contact mode*.

Figure 2.1 B shows the commercial AFM used during this thesis from Nanotec Electrónica (Madrid, Spain). In this setup configuration the AFM head containing the cantilever holder and the photodetector system is uncoupled from the sample positioner consisting in piezoelectric tube.

The AFM tip attached to a cantilever is an essential piece of the microscope, indeed it is responsible of probing the scanned surface. The sharpness of the tip, with a typical radius of few nanometers, makes possible the scanning of localized regions leading to a lateral resolution in the nanometer scale. The flexibility of the cantilever, with a typical spring constant ranging from 50 to 1000 pN/nm, allows the transduction of the force sensed by the tip to a mechanical deflection registered in the photodiode as variation on the position of the laser reflection. Sharpness and elasticity, of the tip and the cantilever respectively, may vary widely. As a standard in biology silicon nitride tips and soft cantilevers ($\sim 50\ pN/nm$) are used. The elasticity of a cantilever depends primordially on its shape. As an example figure 2.2 shows electron micrographs of triangular and rectangular cantilevers facing up allowing the visualization of the AFM tip.

AFM tip-surface interaction

The nature of the different contributions to the tip-surface interaction can be extremely complex and a detailed description of them is far away from the aim of this thesis.

As a simple view, the interaction between the AFM tip and the sample

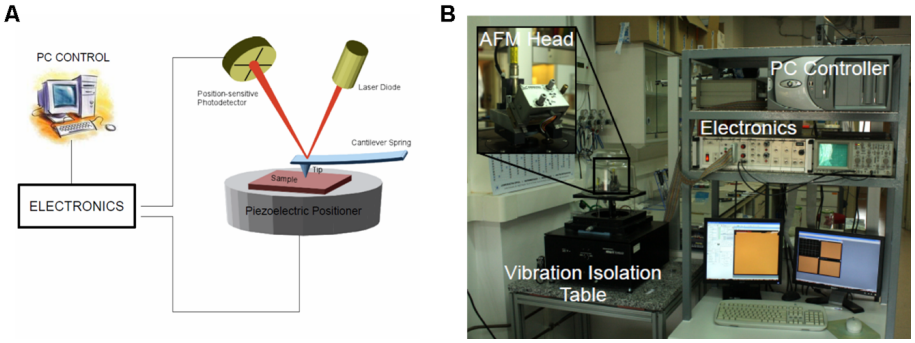

Figure 2.1 – AFM setup diagram. (A) shows a scheme of an atomic force microscopy. (B) shows the AFM setup used during this thesis.

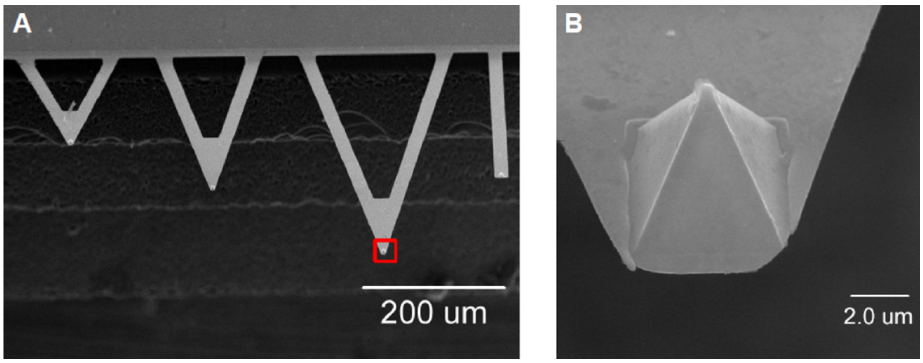

Figure 2.2 – AFM Cantilevers and tips. Electron microscopy images of triangular and rectangular cantilevers (A). (B) is a magnification of the AFM tip placed at the free end of one cantilever in (A) (red square). Adapted from http://www.mobot.org/jwcross/spm/

surface might be described with a Lennard-Jones potential

$$V_{LJ}(r) = 4\varepsilon \left[\left(\frac{\sigma}{r}\right)^{12} - \left(\frac{\sigma}{r}\right)^{6} \right] \tag{2.1}$$

where ε is the depth of the potential well and σ is the distance at which the potential is zero (see figure 2.3). The LJ potential was introduced as an approximation to study the interaction between two neutral atoms or molecules. Essentially, it is the balance of two terms, a short-range repulsive term ($\propto r^{-12}$) describing Pauli repulsion due to the overlap of electron orbitals of the atoms, and a long-range attractive term ($\propto r^{-6}$)

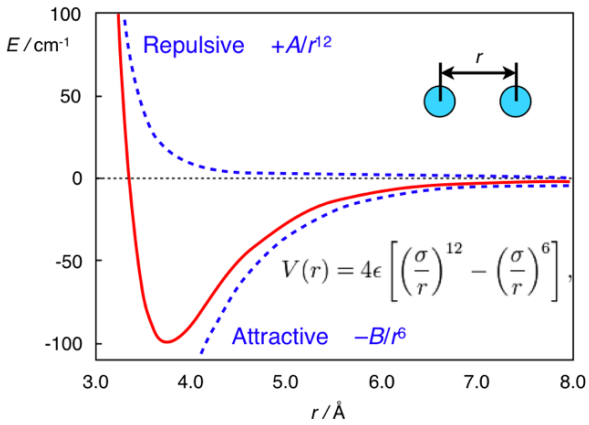

Figure 2.3 – Lennard-Jones potential.

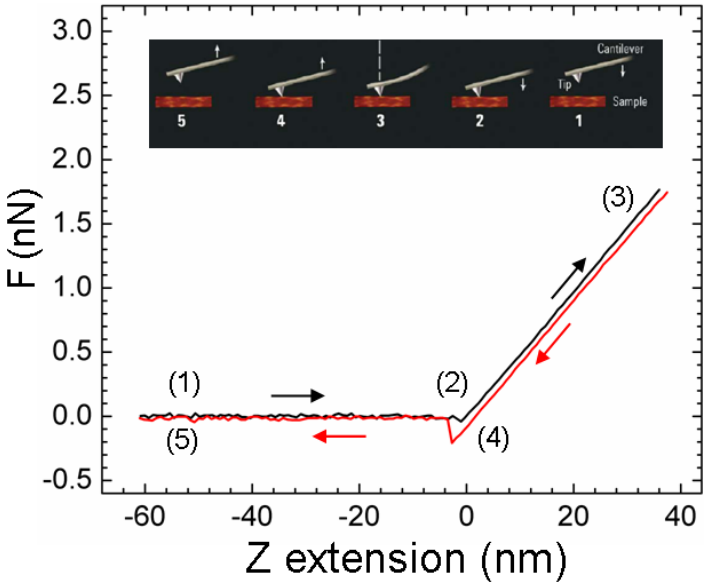

Figure 2.4 – Force vs. piezotube z extension.

due to the Van der Walls force. In our case other forces might contribute to the AFM tip-surface interaction. Capillary force, due to the formation of a water meniscus between the tip and the sample surface, and long-range electrostatic have a great impact while measuring in air conditions. In liquid, there are other contributions like the double-layer force, due to the counterion layer surrounding a surface; the solvation, hydration and hydrophobic forces, arising from the organization of liquid molecules; and the chemical specific forces, due the interaction between a specific pair of molecules such as ligand-receptor interaction. For an extensive review of theoretical and experimental description of these forces see [55,56].

The force between the AFM tip and the sample surface can be obtained as the derivative of the interaction potential described above, $V(r)$, respect to the tip-sample distance r, i.e.:

$$F(r) = -\frac{\partial V(r)}{\partial r} \tag{2.2}$$

Indeed, what an AFM measures experimentally is this force not the interaction potential. Figure 2.4 shows a force vs the z-extension of the piezoelectric tube while the tip is approaching to (black line) and retracting from (red line) the surface. In (1) the tip is far way from the surface and the cantilever is not deflected. (2) shows when the tip enters to contact with the sample and the increasing cantilever deflection is registered until the

tip is retracted (3) and the deflection decreases progressively. Finally, the tip snap off the surface and the force registered is zero (4) while it retracts further away (5). Notice that between (2) and (4) the tip is in contact with the sample and that z is not the distance between the surface and the tip. In fact, the linear dependence between the force and the z-extension of the piezotube along this *contact ramp* is what AFM uses to obtain sample topography as we explain in the following section.

Measurement modes and image acquire

The AFM can be operated in different measurements modes. In this section we will describe the *contact mode*, probably the simplest way to obtain topographical images with the AFM, and the *jumping mode*, that was the mode used in the thesis. The *dynamic* or *tapping mode*, frequently used to measure biological samples, will not be reviewed here.

a) **The *contact mode*** keeps constant the force registered during the surface scan. When the AFM tip encounters a change in the topography, i.e. a depression or a protrusion, the feedback control reacts and the electronics sends an electric signal to expand or contract the piezoelectric tube to compensate the changes in the deflection of the cantilever (see figure 2.5 A). Note that AFM collects the voltages applied to the piezotube, and to get the reliable topography these values must be inverted and the displacement of the piezo previously calibrated with a sample of known height, typically a microfabricated grid.

Contact mode is the simplest operation mode of the AFM but it is not the best suited to measure soft biological samples. First, the scan between two neighboring positions takes place with the tip touching the sample generating a lateral force that can drag the molecules attached to the surface. Second problem is that a drift in the position of the laser reflection on the photodiode during imaging can imply an increment in the force and this must be monitored and corrected manually.

b) **The *jumping mode*** registers the deflection of the cantilever, i.e. the force, while it is approaching to and retracting from the surface at each point of the image during the sample scan (figure 2.5 B). To avoid lateral force and its drag effect the cantilever is moved laterally

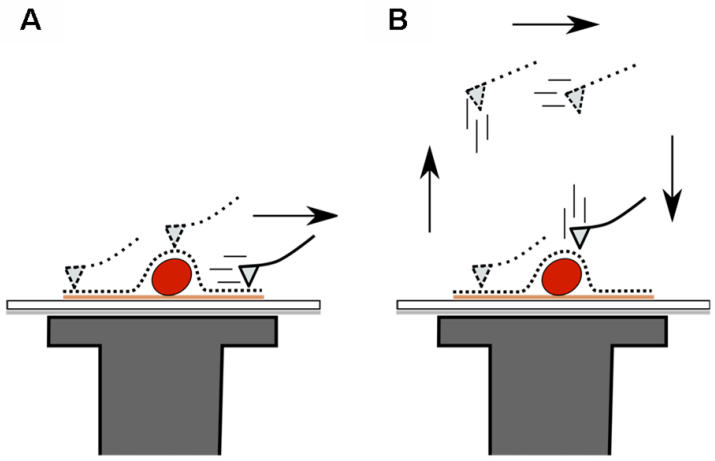

Figure 2.5 – AFM contact and jumping modes. (A) Contact mode. (B) Jumping mode.

to the neighboring position when it is away from the surface. Note that this is specially important when molecules are gently adsorbed, i.e. freely to diffuse laterally, on the surface.

Jumping mode constructs the topographical image from the voltages applied to the piezo tube to maintain the normal force applied to the sample constant. The difference with *contact mode* is that *jumping mode* calculates the force subtracting the cantilever deflection when the tip is in contact with sample minus the cantilever deflection when the tip is retracted from the sample. This feature of the *jumping mode* allows evaluating and correcting any drift in the position of the laser reflection on the photodiode during the sample scan.

Sample preparation

Visualization of biological molecules under buffer solution requires a chamber containing the surface and the cantilever immersed in liquid.

Figure 2.6 B shows a scheme of the chamber used during this thesis. The bottom of the chamber consists of a mica disc glued to a bigger disc of teflon also glued to a metallic disc. Mica was used because it is very simple to get atomically flat surface after cleaving it due to its lamellar structure, providing an excellent contrast with the molecules of interest, with typical height of few nanometers. The teflon, as a hydrophobic surface, keeps the liquid drop on the mica disc, and the metal disc provides a firm attachment

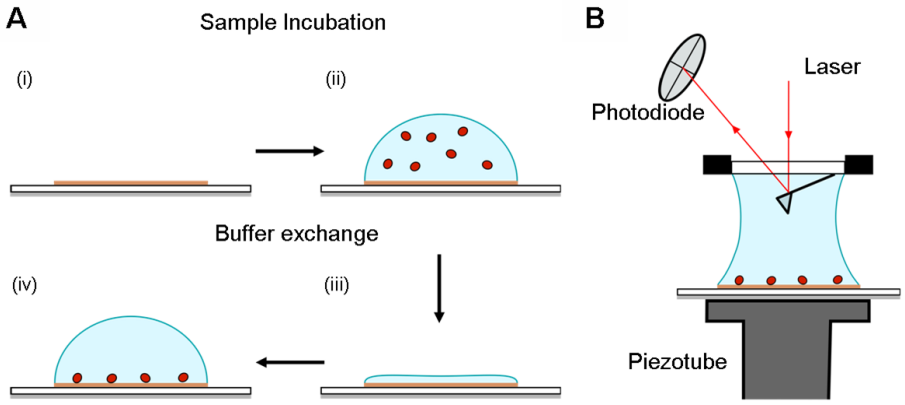

Figure 2.6 – AFM sample preparation and liquid chamber. (A) Sample preparation. (B) AFM liquid chamber.

to the positioner through a magnet present in the piezoelectric tube. The upper part of the chamber is the cantilever holder, firmly attached to the AFM head. The transparent window on top has two functions, to let the laser enter in the liquid and reflect on the cantilever, and to form a meniscus with the water drop deposited onto the mica.

Figure 2.6 A shows the regular procedure to adsorb the biomolecules of interest used in this thesis, such as lipidic unilamellar vesicles, or FtsZ and ZipA proteins. The purified sample is incubated onto the mica disc at the desired concentration and after incubation the drop is exchanged by the sample-free visualization buffer. Notice that between first and second step, the mica surface must be maintained always hydrated to avoid sample damage. If we want to adsorb sequentially different biomolecules a new sample incubation and buffer exchange cycle is performed.

2.2 Quartz Crystal Microbalance (QCM)

The quartz crystal microbalance belongs to the family of piezoelectric sensors that use acoustic waves to detect biological events in real time. In this section we review the historical developments on the QCM from its initial application to monitor thin layer growth on surfaces to biological application in liquid environment. We also address the physical principles underlying the measurement process of QCM and signal modelization that allows to use QCM devices for both mass detection and analyzing structural and mechanical properties. Finally, we briefly describe the experimental procedure for sample preparation and signal recording under liquid buffer.

2.2.1 Historical background and applications of QCM

QCM became widely used as a mass balance in 1959 when theory and experiments demonstrated the relationship between the frequency change of an oscillating quartz crystal plate with the amount of mass adsorbed on its surface[57]. During the next decades QCM was used in vacuum and gas environment to monitor thin layer deposition, oxidation rates of metal surfaces and gas adsorption and desorption processes[58].

The use of QCM in liquid environment began in 1982 when Nomura and coworkers described the behavior of a quartz crystal in aqueous solution[59]. Specially relevant was the work by Kanazawa and Gordon in 1985 that incorporated the mass loading contribution of the liquid phase to the crystal surface, establishing the relationship between the frequency change of the oscillating quartz plate with the density and viscosity of the liquid solution[60]. The use of QCM device as a balance for mass detection of biological samples under buffer solution required an expression relating the total frequency change of the quartz crystal resonator with the amount of mass adsorbed to the crystal surface and the mass loading contribution of the liquid phase. This problem was solved by Martin and co-workers in 1991[61] demonstrating that the addition of the Sauerbrey equation to the Kanazawa equation accounted for the total frequency change of the quartz sensor due to the mass adsorbed on its surface and the loading of the liquid phase.

Further modeling to understand the origin of the signal recorded with the QCM was developed during the 90s. The relationship of the mass

and frequency described by the Sauerbrey equation was biased because viscoelastic effects are not included. This is specially important with soft biological samples. The characterization of a quartz crystal resonator loaded by a viscoelastic thin layer was solved in 1999 by Voinova and co-workers allowing the use of the QCM not only as a balance but also to extract mechanical properties of the mass adsorbed on the surface sensor, such as the shear viscoelastic young modulus[62].

The use of QCM under liquid environment expanded the number of potential applications including biological applications. The application fields include clinical diagnosis, biomaterials, biomedicine, environmental science and food safety. Among the processes studied with QCM devices there are (bio)film deposition, detection of specific antigens, biomolecule binding kinetics, cell adhesion, and DNA detection.

Specifically, DNA studies regarding how ligands bind to specific gene sequences[63] or adsorption of DNA onto functionalized surfaces in the context of DNA sensors, genes delivery, DNA hybridization, and DNA-protein interaction[64–66]. In biomaterial science, QCM has been used to measure protein adsorption to different surfaces to determine, first if the material promotes or resists protein adsorption, and second if this initial protein layer can mediate cell attachment and prevent unwanted interactions[67–70]. In protein science, QCM has been used to monitor protein-protein, protein-DNA, and protein-small molecule interaction. Besides just looking at binding kinetics and affinity constants, conformational changes such as swelling and hydration processes can be also studied[71].

Specially relevant for the aim of this thesis are QCM applications to the formation of supported lipid bilayers (SLBs). SLBs formation monitored by QCM leads to a very specific signal first studied by Keller and Kasemo in 1998[72] due to the detection of vesicle adsorption to the surface with water trapped inside and its subsequent rupture and spreading to form a lipidic bilayer. SLBs as membrane model systems have been used to investigate protein-membrane interactions on top such as two-dimensional self-assembly of annexin A5[73], membrane-hyaluronan films and hyaluronan interaction with membranes containing cell receptor CD44[74,75], and the interaction of nuclear transport receptors with nucleoporin thin films reconstituted onto lipid bilayers[76].

2.2.2 QCM measurement principles

The physical principle underlying the QCM is the piezoelectric effect discovered by Pierre and Jacques Curie in 1880. Piezoelectric materials, such as certain crystal solids and ceramics, are mechanically stressed and deformed by the application of an external electric field. In the case of QCM sensors, a thin disc cut at 35.25° angle to the optical axis of quartz mineral (the so-called AT-cut) is sandwiched between two gold electrodes (figure 2.7 A). An electric potential applied to the electrodes produces a shear (tangential) deformation of the quartz disc due to the piezoelctric effect (figure 2.7 B).

When an alternate electric field with a fixed frequency is applied to the electrodes the bottom and the top surface of the quartz plate move with the same frequency but in parallel and opposite directions. This motion generates an acoustic wave propagated through the quartz perpendicularly to the plate surfaces, and reflections of this wave in both surfaces produced a standing wave within the crystal (figure 2.7 B). From the solution of the wave equation, the eigenfrequencies (also called resonance frequencies) of the crystal are:

$$f_N = N\frac{v_q}{2t_q} \quad ; \qquad N = 1, 3, 5, 7, ... \tag{2.3}$$

where N is the order of the overtone, v_q is the wave propagation velocity within the quartz and t_q is the thickness of the quartz plate (details on mathematical solution of the wave equation can be found in the literature[77,78]). Equation (2.3) indicates that only odd overtones are excited and that resonance frequency (f_N) and the wave length (λ_N) depends on

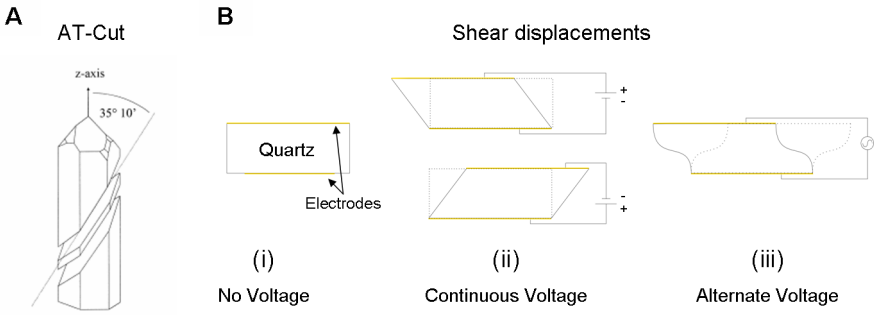

Figure 2.7 – Quartz AT-cut shear displacement. (A) Quartz plate deviated only 5′ from the AT-cut of 35° 15′ angle . (B) Shows the cross section of an AT-cut quartz plate and its shear deformation under (i) no potential, (ii) continuous voltage, and (iii) alternate voltage.

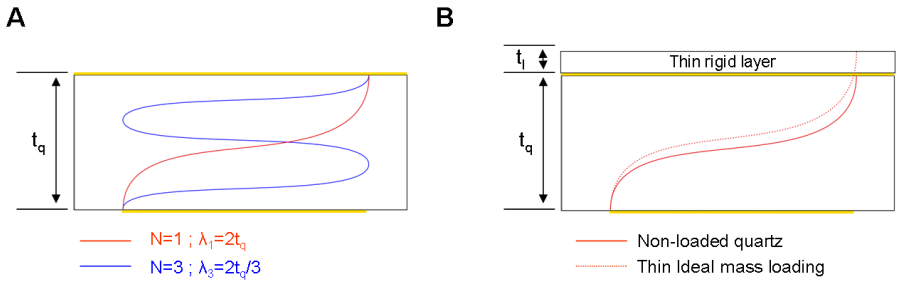

Figure 2.8 – Thin ideal mass loading (Sauerbrey equation). (A) Cross-section of an unperturbed quartz TSM resonator amplitude profile of the mechanical deformation for the first (red) and for the third overtone (blue) with $\lambda_1 = 2t_q$ and $\lambda_3 = 2t_q/3$ respectively. (B) Shows the wave length increase in the fundamental overtone for a quartz plate loaded with a thin rigid layer due to an increase in the total thickness and resulting in a decrease of the resonance frequency.

the quartz thickness, i.e:

$$t_q = N\frac{\lambda_N}{2} = N\frac{v_q}{2f_N} \quad ; \qquad N = 1, 3, 5, 7, ... \tag{2.4}$$

as represented in figure 2.8 A.

Ideal mass loading

Equation 2.4 can be used to relate a change in the thickness (Δt) of the resonator with a change in the acoustic wave propagated through the crystal. If the thin layer adsorbed is assumed to have the same properties of the quartz then an increase in wavelength and a decrease in the resonance frequency of the quartz as represented in 2.8 B can be related, i.e:

$$\Delta t = -N\frac{v_q}{2f_N^2}\Delta f_N \tag{2.5}$$

Using $\Delta t = \Delta m/\rho_q$ and $f_N = Nf_0$, equation 2.5 can be written as

$$\Delta m = -\frac{v_q\rho_q}{2f_0^2}\frac{\Delta f_N}{N} = -C\frac{\Delta f_N}{N} \tag{2.6}$$

where m is the mass per unit area of the thin layer attached to the quartz surface, $\rho_q = 2650\ Kg/m^3$ is the quartz density, $v_q = 3340\ m/s$ is the speed of sound in the quartz, and f_0 is the fundamental frequency of the resonator.

The sensitivity constant C depends on the fundamental frequency f_0, for the crystal used in this thesis $f_0 \approx 4.95\ MHz$ and $C = 18.1\ ng/Hz \cdot cm^2$

Equation 2.6 is known as *Sauerbrey equation*, and is only valid when the mass layer deposited on the quartz surface is (i) small compared to the weight of the crystal (less than 10%), (ii) rigidly adsorbed, and (iii) evenly distributed on the surface. Moreover *Sauerbrey equation* does not account the changes in frequency due to the mass loading by the presence of a semi-infinite liquid layer when the QCM is operated in aqueous solution.

Semi-infinite liquid loading

Kanazawa and co-workers solved the acoustic wave propagation in the liquid due to to the coupling at sensor surface. The solution predicts a damping in the shear wave propagated through the liquid with a characteristic decay length, δ_N (see figure 2.9), and a decrease in the quartz resonance frequency, Δf_N, for the different overtones

$$\delta_N = \sqrt{\frac{\eta_L}{\pi f_N \rho_L}} = \frac{1}{\sqrt{N}}\sqrt{\frac{\eta_L}{\pi f_0 \rho_L}} \tag{2.7}$$

$$\Delta f_N = -f_o^{3/2}\sqrt{\frac{\rho_L \eta_L}{\pi \mu_q \rho_q}}\sqrt{N} \tag{2.8}$$

Equation 2.8 shows that, under aqueous solution, changes in the acoustic wave are coupled to the mechanical parameters of the liquid, i.e. its

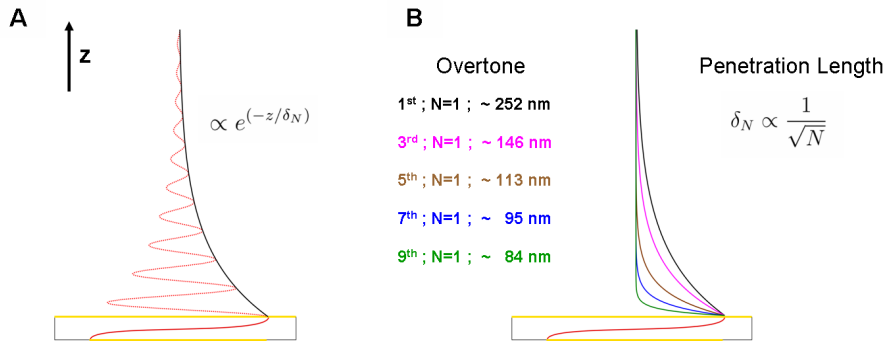

Figure 2.9 – Semi-infinite liquid loading (Kanazawa equation). (A) shows the amplitude profile of the mechanical deformation of the quartz crystal (continuous red line) and the acoustic wave penetration into the liquid (dashed red line). (B) shows the penetration length (δ_N) for different overtones.

density (ρ_L) and viscosity (μ_L), i.e:

$$\sqrt{\rho_L \eta_L} = -\frac{1}{\sqrt{N}} \frac{\sqrt{\pi \mu_q \rho_q}}{f_0^{3/2}} \Delta f_N \tag{2.9}$$

Simultaneous ideal mass and liquid loading

Martin and co-workers[61] predicted the total change in resonance frequency for the different overtones, Δf_N, of the quartz resonator when it is loaded simultaneously by an ideal thin layer and a semi-infinite liquid. They obtained a linear combination of the Sauerbrey equation (eq 2.6) and Kanazawa equation (eq 2.8), i.e.:

$$\Delta f_N = \Delta f_{Sauerbrey} + \Delta f_{Kanazawa} \tag{2.10}$$

Equation 2.10 shows that changes in resonance frequency of the quartz sensor must be carefully evaluated. To separate liquid loading from the mass adsorption contribution upon sample addition a reference base line is used to monitor changes in the buffer solution and directly subtracted.

2.2.3 QCM with dissipation monitoring (QCM-D)

To obtain the full potential of the QCM devices it is necessary to measure both the frequency and dissipation changes of the oscillating quartz resonator (Δf and ΔD respectively). The dissipation factor D of an oscillating system is defined as the ratio between the energy dissipated and the energy stored by the oscillator in one cycle, i.e:.

$$D = \frac{1}{Q} = \frac{1}{2\pi} \frac{E_{dissipated}}{E_{stored}} \tag{2.11}$$

where Q is the quality factor of the resonant peak.

We present here two technical approaches corresponding to the different setups used in this thesis. QCM D300 from Q-sense (Göteborg, Sweden) uses the relationship between the decay of a freely oscillating crystal after being excited at resonance frequency[79] with the dissipation factor D. QCM-Z500 from KSV (Finland) obtains D directly measuring the width of the resonant peak.

Qsense technology

When the alternate voltage is switched on and off it is possible to monitor the movement of the driven and free resonator respectively. The amplitude of the driven resonator can be described as an harmonic oscillator (figure 2.10 A)

$$A(t) \propto sin(2\pi f \cdot t) \tag{2.12}$$

in contrast the free oscillator is described as a damped oscillator where an exponential decay depending on the dissipation factor (figure 2.10 B)

$$A(t) \propto sin(2\pi f \cdot t) \cdot e^{(-\pi f D \cdot t)} \tag{2.13}$$

The damping effect is used to differ between different sensor loading conditions (figure 2.10 C). This approach allows to calculate f_N and D_N with subsecond temporal resolution for each overtone and consequently to obtain the corresponding changes Δf_N and ΔD_N.

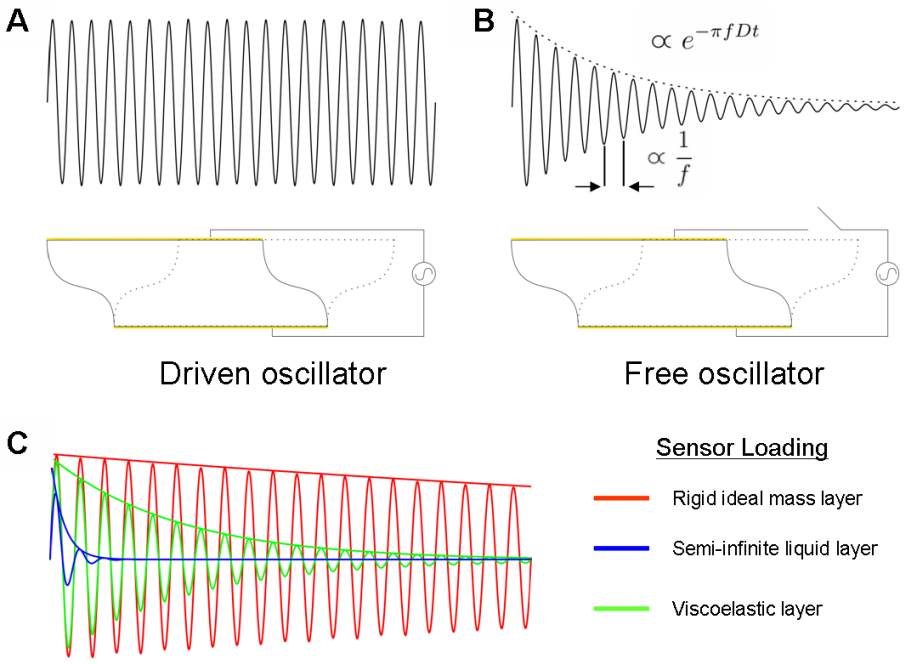

Figure 2.10 – Qsense technical approach. (A) shows the quartz resonator driven at resonance frequency (f). (B) shows a free quartz resonator behaving as a damped oscillator. (C) shows the damping oscillation of a free quartz resonator for different loading conditions.

Impedance analyzer

Dissipation factor D can be obtained by measuring the bandwidth of the resonant peak, the larger the damping the broader is the resonance peak. Impedance analysis approach uses the electrical impedance, a complex magnitude, across the quartz sensor

$$Z_e = R + jX \tag{2.14}$$

modelized with an equivalent circuit (figure 2.11 A) exploiting the electromechanical analogy, i.e.:

$$Z_e = R + j\left(\omega L - \frac{1}{\omega C}\right) \tag{2.15}$$

where $\omega = 2\pi f$ is the angular frequency of the alternate voltage applied to quartz crystal, and $j = \sqrt{-1}$. The resonant peak is obtained from the admittance (the inverse of $|Z_e|$), i.e.:

$$|Y| = \frac{1}{|Z_e|} = \sqrt{\frac{1}{R^2 + (2\pi f L - 1/2\pi f C)^2}} \tag{2.16}$$

Figure 2.11 B shows two examples of the response of the resonant peak under rigid and liquid loading. Only a frequency shift is observed for a rigid layer adsorption while both a decrease in frequency and an increase in the bandwidth of the peak is observed for liquid loading indicating a dissipation damping.

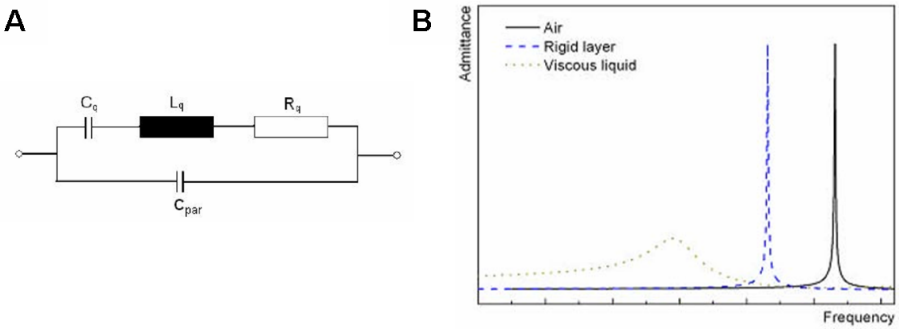

Figure 2.11 – Impedance analyzing approach. (A) shows the LCR equivalent circuit of the quartz. (B) shows changes in the resonant peaks for unperturbed resonator (black), for a rigid mass loading (dashed blue), and for liquid loading (dashed yellow). Adapted from KSV-Z500 tutorial.

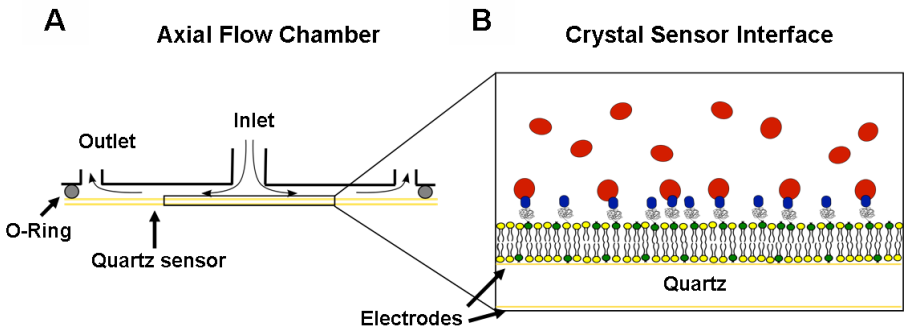

Figure 2.12 – QCM liquid chamber scheme. (A) shows a QCM liquid chamber geometry where the sample is injected perpendicularly to the crystal sensor surface. (B) represents a high magnification of the sensor interface where the biomolecule adsorptions take place.

To transform the measured electrical impedance into mechanical parameters of the mass layer adsorbed onto the surface quartz sensor it is necessary to model the piezoelectric sensor. The transmission line model is a general approach that provides a mechanical and electrical description for the piezoelctric sensor under various loading conditions [80].

2.2.4 Sample preparation and signal recording

We have used the QCM to follow the anchoring of FtsZ to a supported lipid bilayer (SLB) by ZipA. The change in resonant frequency, Δf, was measured during the SLB formation, the ZipA binding to the bilayer, and the FtsZ anchoring to ZipA. Sauerbrey equation (eq 2.6) was used to estimate the mass amount adsorbed to the quartz sensor surface.

To monitor the successive adsorption events samples are prepared at desired concentration and injected through a fluid chamber (see figure 2.12). Temperature control is essential to obtain a good signal without drifts. A thermoblock and a pelltier are used for external and internal temperature control respectively.

Part II

FtsZ filaments on mica surface

Chapter 3

Single FtsZ isolated rings: Structure and dynamics

Abstract

We report observation and analysis of the depolymerization filaments of the bacterial cytoskeletal protein FtsZ (filament temperature sensitive Z) formed on a mica surface. At low concentration, proteins adsorbed on the surface polymerize forming curved filaments that close into rings that remain stable for some time before opening irreversibly and fully depolymerizing. The distribution of ring lifetimes (T) as a function of length (N), shows that the rate of ring aperture correlates with filament length. If this ring lifetime is expressed as a bond survival time, ($T_b \equiv NT$), this correlation is abolished, indicating that these rupture events occur randomly and independently at each monomer interface. After rings open irreversibly, depolymerization of the remaining filaments is fast, but can be slowed down and followed using a nonhydrolyzing GTP ana-

logue. The histogram of depolymerization velocities of individual filaments has an asymmetric distribution that can be fit with a computer model that assumes two rupture rates, a slow one similar to the one observed for ring aperture, affecting monomers in the central part of the filaments, and a faster one affecting monomers closer to the open ends. From the quantitative analysis we conclude that the depolymerization rate is affected both by nucleotide hydrolysis rate and by its exchange along the filament, that all monomer interfaces are equally competent for hydrolysis, although depolymerization is faster at the open ends than in central filament regions, and that all monomer-monomer interactions, regardless of the nucleotide present, can adopt a curved configuration.

3.1 Introduction

Bacterial cytoskeletal protein FtsZ (filamenting temperature sensitive Z) assembles into dynamic polymers on the inner side of the bacterial cytoplasmic membrane in the presence of GTP. Its role in cell division is twofold: recruiting the rest of the proteins involved in the assembly of the septal ring and contributing to generate the force needed for cell rupture. Recent *in vitro* experiments with artificially membrane-bound FtsZ reconstituted in model systems support the suggestion that FtsZ is capable of generating a contractile force without the need of any other proteins [33,81]. Several theoretical models trying to explain the molecular mechanism by which the GTP-dependent self-assembling polymerization process generates a contractile force have been recently proposed [82–91], but the debate is still open. Existing controversy over the relative contribution of filament curvature and lateral interactions in the constriction process is difficult to resolve until new experimental data determine how GTP hydrolysis is associated to monomer exchange within filaments.

FtsZ is known to polymerize above a critical concentration in the presence of GTP [92]. Bulk experiments in solution using a fluorescence signal to follow polymerization [29] have provided indirect evidence of monomer exchange, annealing and depolymerization of individual filaments. Visualization of filaments adsorbed on a mica surface with atomic force microscopy (AFM) [12,93] also showed a rich dynamic behavior in which annealing, filament curvature and lateral interactions played important roles. We now extend the AFM analysis to characterize the depolymerization of isolated individual filaments. We have quantitatively analyzed the behavior of two types of structures: closed rings and open curved filaments. The survival time of closed FtsZ rings and the shortening of open filaments were analyzed using statistical methods. This analysis, combined with computer simulations, allowed estimating the depolymerization velocity of the open filaments and describing the influence of the monomer location within the filament on the depolymerization rate. We conclude that all monomer-monomer interfaces are competent for depolymerization and that each rupture event takes place randomly and independent of its position, excluding any cooperative depolymerization process. We also conclude that depolymerization at the open ends is faster than in central filament regions and that filament curvature is not solely associated with the presence of GDP.

3.2 Materials and methods

Protein Purification and Assay

Escherichia coli FtsZ was purified by the calcium-induced precipitation method as described previously. The protein concentration was measured using the bicinchoninic acid assay (Pierce), with spectrophotometrically calibrated FtsZ standards[10].

AFM imaging

A 50 nM solution of FtsZ in Tris-HCl 50 mM, KCl 500 mM, $MgCl_2$ 5 mM pH 7.5 buffer in the presence of 1 mM GTP was incubated on a freshly cleaved mica surface for 10 min. Excess protein was removed and images of the adsorbed protein were taken under buffer at different pH (50 mM Citrate buffer, KCl 500 mM, $MgCl_2$ 5mM adjusted for pH 5, 6.5 and 7.5). Experiments done in the presence of glycerol were carried out by adding 15% glycerol to the imaging buffer after the filaments had been formed on the mica surface. Images were taken in jump mode[94] optimizing conditions to allow taking one image per minute.

Filament shape parametrization

Filaments that were stable and isolated enough to assure that their dynamic behavior was not affected by the proximity of neighboring filaments were parametrized and analyzed. Filaments were described in polar coordinates using the harmonics series:

$$r(\theta) = \frac{1}{2}a_0 + \sum_{n=1}^{5} \left[a_n \cos(n\theta) + b_n \sin(n\theta)\right] \tag{3.1}$$

truncated at the fifth term in order to have enough flexibility to adjust any filament. The detailed analytical protocol is presented in the Supplementary Material.

3.3 Experimental results

3.3.1 FtsZ individual filaments

Individual FtsZ filaments form on a mica surface exposed to a solution with FtsZ below its critical concentration, even when no filaments form in the solution[92]. They assemble due to a local increase in protein concentration on the surface. It has been previously shown that this process is dependent on the surface diffusion of the monomers, and that lowering the temperature or increasing the viscosity of the solution reduces the number of observed filaments[95]. The filaments studied were formed exposing mica to a 50 nM protein-GTP solution for 10 min before adding the protein-free imaging buffer also containing 1 mM GTP. It is important to note that samples are imaged in the absence of protein in solution, therefore no protein is available in the bulk to exchange with the filaments. This preparation protocol allowed the formation of short filaments that closed to form stable rings. After the rings opened irreversibly, we measured the depolymerization velocity of the open filaments. The two types of structures, closed rings and open curved filaments, were analyzed separately.

3.3.2 Closed rings

Closed FtsZ rings on the mica can either open transiently at random locations or irreversibly, leading to subsequent filament depolymerization. Reversible opening events were sometimes followed by a loss of material that gave rise to smaller rings. Because depolymerization rate is associated with GTP hydrolysis[92], we explored the behavior of rings formed in the presence of guanosine-5'-[(β,γ)-methyleno]triphosphate (GMPCPP), a slow hydrolyzing GTP analogue[96] and in low pH solutions, that are also known to decrease GTP hydrolysis rate[9]. In both cases, the reduction in the hydrolysis rate produced an increase in ring lifetime. Increasing the viscosity of the imaging solution adding glycerol reduced monomer diffusion and was also efficient in stabilizing the closed rings. Figure 3.1 shows some rings and their size distribution under three experimental conditions. The most frequent size observed falls within the expected values considering that the spontaneous curvature of the open filaments described earlier[97], with a preferred angle of 2.4°- 3.0° degrees between neighbor bonds, would bring the two ends close to each other when N is in the range of 120 to 150

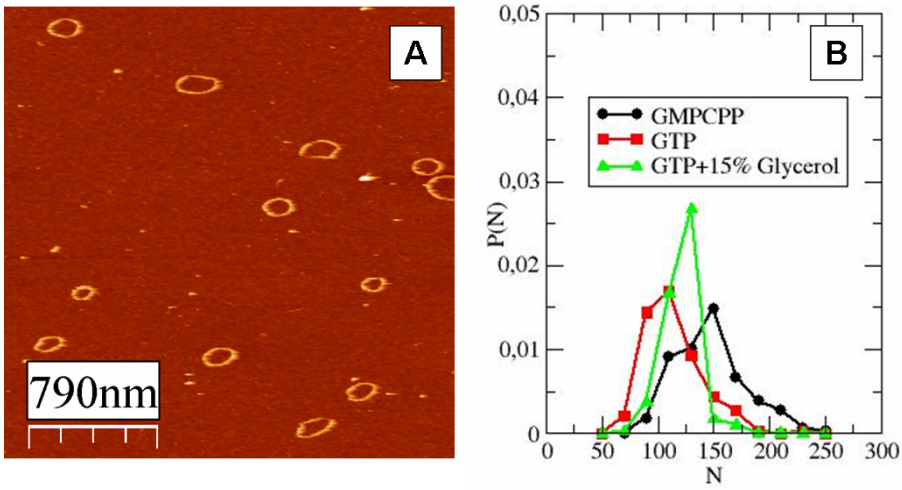

Figure 3.1 – FtsZ closed rings AFM image and size distribution. (A) AFM image of FtsZ rings formed in presence of GTP at pH 7.5 (B) Size distribution of rings formed with GTP (squares), GMPCPP (circles) and GTP plus 15% of glycerol (triangles)

monomers.

Figure 3.2 illustrates the typical behavior of the rings over time: Openings can happen at different positions in the same filament (Figure 3.2 A), and some are followed by material loss that reduces the size of the ring (Figure 3.2 B). Movies showing the behavior of the filaments over time are presented as Supplementary Material (VideoS1a and VideoS1b).

For each ring, we measure the length (N), lifetime (T) (i.e., the time before it opens irreversibly), and define a bond lifetime ($T_b \equiv NT$) (see section below). Table 1 summarizes the average values $\langle N \rangle$, $\langle T \rangle$, and $\langle T_b \rangle$ for three populations studied: rings formed with GTP, with GMPCPP and rings formed with GTP but observed with glycerol present in the imaging buffer. Supplementary Materials shows the data for rings observed in low-pH solution. Slow hydrolysis and reduced monomer diffusion are both associated with longer and more stable rings.

3.3.3 Depolymerization of open filaments

Filaments with GTP disappear very fast once opened, usually within 1 min, the time needed to take an AFM image (Figure 3.3 A). Increasing the scan rate to 40 s per image allowed us to see at least one open filament, but

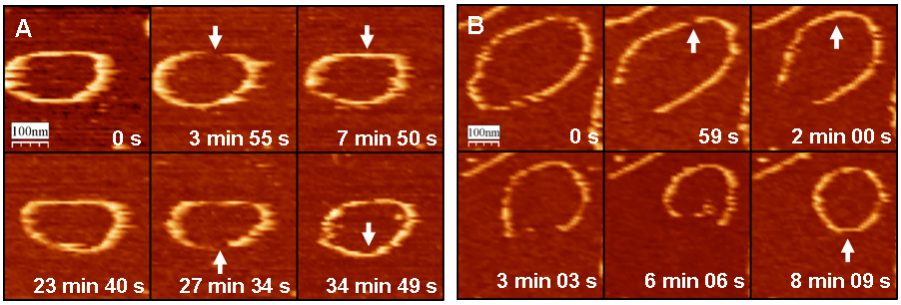

Figure 3.2 – FtsZ closed rings dynamics. Shape fluctuation, opening, and reannealing at random positions (arrows) are observed for GTP (A) and GMPCPP (B). Opening event followed by a partial depolymerization leading to smaller ring is observed in B.

it was not possible to follow the intermediate steps of depolymerization (Figure 3.3 B). In the presence of GMPCPP, however, the process is slow enough to be observed along several frames (Figure 3.3 C) (see Supplementary Material).

Figure 3.3 D illustrates that the depolimerization observed when the viscosity of the imaging buffer is increased has the same qualitative behavior (see Supplementary Material). When GTPase hydrolysis is slowed with increasing acidity of the imaging buffer[9], the depolymerization process is comparable (Supplementary Material).

3.4 Quantitative analysis and simulation models

3.4.1 Length and lifetime of closed rings

Filaments were parametrized to measure filament length as a function of time as described in detail in the Supplementary Material. The size N (number of monomers) and lifetime T of rings of three different ring populations are presented in Figure 3.4 A. All three (T, N) distributions are quite broad, spanning in length from 50 to 230 monomers and in ring lifetime from 1 to more than 50 min. The distributions shows that the length is correlated with the lifetime-i.e., longer rings have a shorter lifetime than

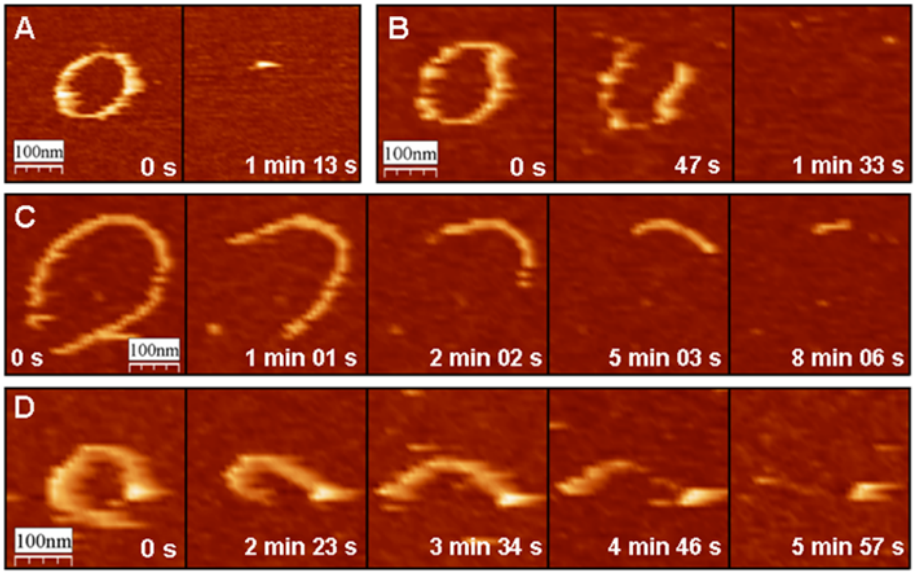

Figure 3.3 – Depolymerization of FtsZ filaments. (A) Shrinkage of a FtsZ closed filament in presence of GTP at pH 7.5-i.e., full GTPase activity and diffusion. (B) Increasing the scan velocity allows observing open filaments in the same biochemical conditions as in A. Slowed depolymerization observed in the presence of GMPCPP (C) or in presence of GTP in an imaging buffer with increased viscosity (D). In all cases, both filament ends lose monomers during depolymerization.

smaller ones. Rings with $N \approx 100$ monomers may last as long as 50 min, whereas rings with $N \approx 200$ are never observed for more than 20 min. An explanation for this length-lifetime correlation is that irreversible opening is triggered by independent events occurring at each monomer-monomer interface. Therefore the larger the number of interfaces, the higher the probability of having one rupture to break the ring. To test this random rupture assumption, eliminating the effect of the number of bonds, we define a typical bond survival time $T_b \equiv NT$. This takes into account the lifetime of a ring, T, and the number of bonds present, N, and reflects the fact that opening of only one bond is enough to trigger the irreversible opening. If this rupture event is stochastic, this bond survival time should have a broad distribution and be independent of filament length. Because the three populations analyzed have different life-times and filament lengths, N and T_b were also normalized by the average $\langle N \rangle$ and $\langle T_b \rangle$ values of each population. This normalization produces the overlap of the three data sets, eliminating the stabilizing effect associated with slow hydrolysis rate and

reduced lateral diffusion. The distributions for $(T_b/\langle T_b\rangle, N/\langle N\rangle)$ shown in Figure 3.4 B are now uncorrelated, as expected for random events.

The experimental data sets allow obtaining the rupture rate of one bond as $v_o = \langle T_b\rangle^{-1}$ for each population studied, and also allow checking if the irreversible opening of a FtsZ ring of size N behaves like a stochastic process with frequency $v_N = N/\langle T_b\rangle \equiv Nv_o$, implying that rupture events occur randomly and independently at each monomer interface (see Supplementary Material for more details on the statistical analysis). The normalized probability for $\tau = T_b/\langle T_b\rangle$, obtained from the three data sets in figure 3.4 B should be very close to the exponential form $P(\tau) = exp(-\tau)$, with no fitting parameters, that describes a fully random process that happens with unit frequency (in the time units normalized by $\langle T_b\rangle$) as shown in figure 3.4 C. This behavior implies that the filaments do not show any kind of aging or memory effect.

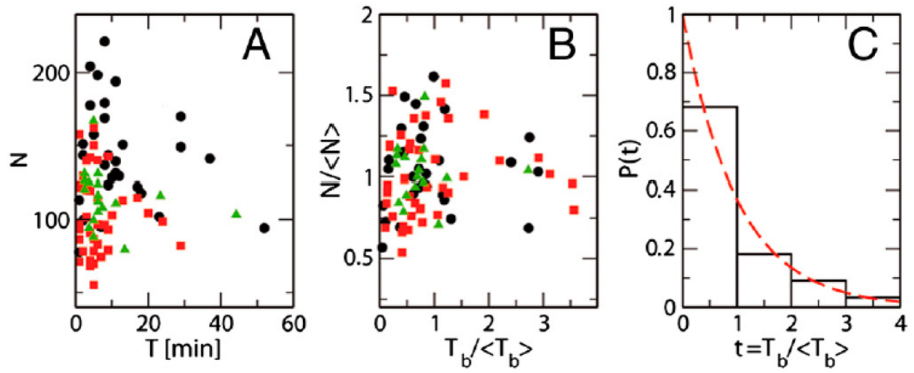

Figure 3.4 – Lifetime vs. length distribution (T, N) of FtsZ rings. Depolymerization of FtsZ rings under different conditions. A shows the (T, N) distribution for the size of each ring N (estimated number of monomers) and its observed survival time T (minutes from the first to the last AFM image in which the ring is observed); black circles, buffer with GMPCPP; red squares, buffer with GTP; green triangles, GTP buffer with 15% glycerol. B shows the distribution $(T_b/\langle T_b\rangle, N/\langle N\rangle)$, for the values of N and $T_b \equiv NT$, normalized to their mean values, given in Table 1. C presents the histogram for the normalized life time per bond $\tau = T_b/\langle T_b\rangle$, collecting the data from the three nucleotide buffers in B independently of their size. The red dashed line is $P(\tau) = exp(-\tau)$, with no fitting parameters, that represents the probability distribution for independent events with unit frequency.

Table 3.1 summarizes the data extracted from the analysis of the survival time of the closed rings and shows the monomer-monomer bond breaking frequencies v_o found for each experimental condition. GMPCPP reduces it to less than half the value obtained for GTP, which correlates well with the known reduction of the hydrolysis rate of GMPCPP. Additional experiments modulating the GTP hydrolysis rate by lowering the pH are shown in the Supplementary Material. Low pH also reduces v_o three fold at pH below 6.5, in accordance with the measured decrease in GTPase activity[9] (see Supplementary Material). From this quantitative analysis of ring lifetimes, we conclude that, under our experimental conditions, with no monomer exchange in and out of the rings, the rupture frequency between protein monomers is random, it correlates both with hydrolysis rate and monomer lateral diffusion, and it is the only parameter required to explain the time evolution of the rings.

3.4.2 Depolymerization rate of open filaments

The length versus time data of 22 open filaments were used to quantify the depolymerization process by measuring the "instantaneous" depolymerization velocity-i.e., the difference in the estimated number of monomers between two consecutive AFM frames. The histogram (figure 3.5) has a broad distribution and includes apparent growth events, in which the estimated length N increases between an image and the following one. Because there is no protein in the imaging buffer, these events are most probably artifacts of our estimation for N.

Buffer	GTP	GMPCPP	GTP glycerol
No. rings	243	365	204
$\langle N \rangle \pm \sigma_N$	103 ± 26	137 ± 32	112 ± 15
$\langle T \rangle$ min	6.5	13.1	8.9
$\langle T_b \rangle$ min	670	1800	990
v_o min^{-1}	0.0015	0.00056	0.0010

Table 3.1 – The number of observed FtsZ rings, their mean size and size dispersion (in number of monomers), and the mean time for which each ring is observed in successive AFM frames, are compared for different nucleotide buffers: GTP, GMPCPP, and GTP with 15% glycerol buffers.

Filaments shrink at a mean rate of 9.3 and 11.8 monomers per minute, respectively, for GMPCPP and GTP with 15% glycerol. Filaments in the presence of GTP depolymerize at least ten times faster, that is, more than 100 monomers per minute, the time needed to take an AFM image, making it technically impossible to measure the depolymerization velocity. The shape of the histogram of the depolymerization velocities can provide additional information to the mean depolymerization rate (see Supplementary Material). The histogram for the filaments grown with GMPCPP is asymmetric. On the positive side (increasing lengths) there is a sharp decay that may be well fitted by a Gaussian and interpreted as the result of the noise coming from numerical estimation of the instantaneous filament length from the AFM images. On the negative side (depolymerization), the velocity distribution has a slowly decaying tail, so that the AFM images taken at 1-min intervals may show the loss of up to 70 monomers. The depolymerization events of filaments with GTP observed in the presence of 15% glycerol are noisier than those with GMPCPP and produce a broader histogram with much weaker (or maybe completely lacking) asymmetry.

The analysis of the closed rings, in which all of the monomer-monomer interfaces are equivalent, indicated that these bonds break independently with a certain frequency correlated with the nucleotide hydrolysis rate. If we extend this hypothesis to open filament, we would expect that the depolymerization of an initially long filament would proceed as a fragmentation process in which any of the bonds would be irreversibly broken with the same frequency v_o, equivalent to the one obtained from the analysis of ring rupture and listed in Table 3.1. Once the filament is fragmented in two pieces, the fragmentation would proceed on each segment independently, until all the pieces are too small to be observed in the AFM images. However, this interpretation does not agree with the experimental results. If a random fragmentation processes with a rupture frequency v_o is applied to open filaments, the computer model described below gives mean depolymerization velocities of 1.36 monomers/min for GMPCPP and 0.98 monomers/min for GTP on filaments observed in the presence of 15% Glycerol. These velocities are significantly slower than the 9.3 and 11.8 monomers per minute measured, indicating that the direct extension from the breaking of rings to shrinkage of open filaments does not explain the observed data.

The opposite view to the fragmentation process at random positions would be to assume that the depolymerization occurs by removing only one monomer from the filament end at a time. To get the observed mean

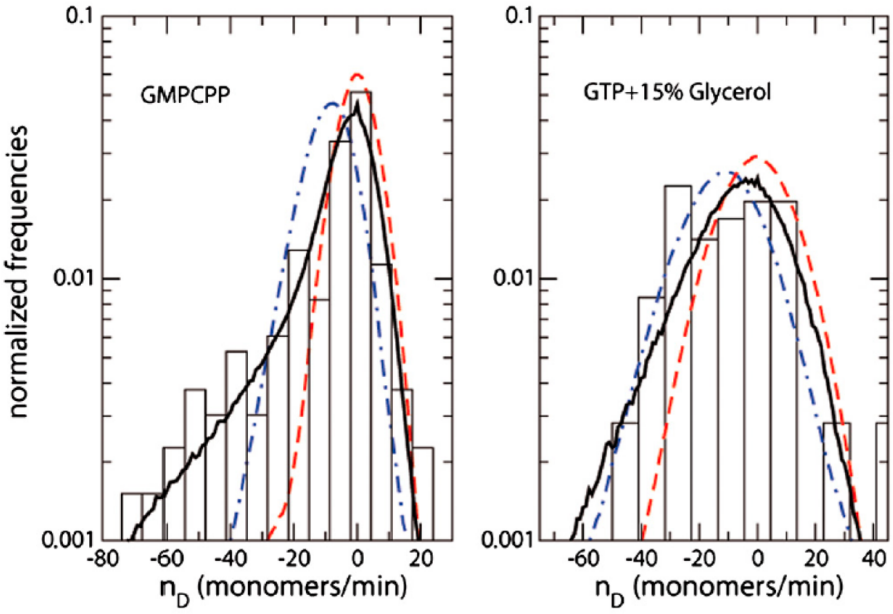

Figure 3.5 – Histograms of depolymerization velocities of FtsZ open filaments. Histograms of depolymerization velocities, in estimated number of monomers between consecutive AFM images taken at 1-min intervals, for GMPCPP buffer (Left) and GTP with 15% glycerol buffer (Right). The black full lines are the simulation results obtained with 10^5 biased fragmentations (see Supplementary Material). Blue dash-dotted lines are the simulation results for unbiased fragmentations, with the frequency v_o measured for closed FtsZ rings. Red dashed lines are the results for one-by-one monomer depolymerization, with frequency fitted to reproduce the observed mean value.

depolymerization velocities, monomers at the ends of the filaments would have to leave at a rate of 4-5 per minute-i.e., about 10^4 faster than the events leading to the breaking of a ring. Under this assumption, and in absence of other sources of noise, the observed distribution of instantaneous velocities between two AFM images would be very narrow and symmetric (see Supplementary Material). Adding some extra noise we could get the broader Gaussian presented by the dash-dotted lines in figure 3.5, which could be acceptable for GTP with glycerol, but clearly fails to reproduce the strong asymmetry of the histograms for the GMPCPP buffer. Neither of these two extreme interpretations, depolymerization by fragmentation process nor by individual monomer release, reproduces the shape of the histogram of depolymerization velocities observed.

3.4.3 Model and computer simulations of fragmentation processes

The bond breaking frequency of rings, the mean depolymerization velocity for open filaments, and the asymmetry of the instantaneous shrinkage velocities may only be explained if we assume that an open filament has different breaking frequencies depending on the location of the bond. Bonds between monomers within the filament have a lower breaking frequency and bonds connecting the monomers at the ends have a higher breaking frequency.

To check if this scenario can explain our experimental results, we have run Langevin computer simulations with a filament model that had been previously developed to study FtsZ filaments[97] and is explained in more detail in the Supplementary Material.

The model, which treats protein monomers as beads in a chain linked by elastic springs, can mimic filament fragmentation. Simulations reveal that the distance, although more significantly, the relative orientation between monomers adjacent to a rupture event, undergo rapid changes (see Supplementary Material)

The overall rupture frequency used in the computer simulations is explained in Supplementary Material. The parameter v_1 represents the rupture frequency of short filaments (bonds at filament ends), whereas the value of v_o extracted from the analysis of the rings (Table 3.1) gives the breaking frequency for long fragments (bonds within the filament). The results of the simulations, with the optimal fitted values for v_1 and using v_o reproduce very accurately the asymmetry of the velocity histograms. The full line in the left panel of figure 3.5 represents the curve for $v_1/v_o = 30 \pm 5$, which fits both the histograms of filaments in GMPCPP and in GTP plus glycerol buffer, indicating that the bonds in short filaments that short filaments rupture 30 times faster than the bonds in closed rings.

3.5 Discussion

The association between nucleotide exchange or hydrolysis and depolymerization has been difficult to study experimentally, in spite of its relevance, to fully understand polymer dynamics. We have now been able, for the first time, to observe the depolymerization of single FtsZ filaments. We have analyzed our data using statistical methods that have provided not only

average kinetic information but also insight into how the depolymerization takes place. A short discussion on the advantages of using this approach as compared to standard kinetic analysis is included as Supplementary Material.

It is clear from our data that nucleotide hydrolysis rate correlates with the rate at which monomers are released. Filament rings increase their lifetime and open filaments decrease their depolymerization velocity under low GTPase hydrolyzing conditions. However, there is a more than 1000-fold difference between the hydrolysis rate and the filament rupture times observed, considering GTPase activities measured in solution [28]. Because in our experiments there is no monomer exchange between the filaments and the bulk, a plausible explanation is the presence of a nucleotide hydrolysis-exchange cycle in which hydrolysis and substitution of the nucleotide occurs many times before an irreversible rupture event takes place. Evidence for this cycle comes from the fact that both decreasing the hydrolysis rate or increasing the solution viscosity retard depolymerization. Higher viscosity keeps the appropriate orientation between open ends after a hydrolysis event for longer times, decreasing the probability of an irreversible rupture in the time needed for the nucleotide exchange, having therefore an equivalent effect to decreasing hydrolysis rate. Depolymerization experiments carried out in solution [29] have also determined that GTPase hydrolysis rate is faster than depolymerization, but in such bulk experiments monomer exchange and monomer release cannot be isolated as independent processes, and therefore their association to GTP hydrolysis or exchange is ambiguous. Biochemical data suggesting nucleotide exchange into protofilaments are available [8,27–29,98], supporting our interpretation that both nucleotide exchange and hydrolysis are determining the observed depolymerization dynamics.

Two additional observations support our suggestion that hydrolysis products within the filament are being substituted by fresh GTP from the bulk before any monomer release takes place. When GTP is removed from the buffer, filaments disappear too quickly to be observed over time. On the other hand, all interfaces behave equivalently along the full lifetime of the ring. Some of the rings formed in the presence of GTP can be observed for more than 10 minutes. Assuming a GTPase hydrolysis rate on the order of eight GTP hydrolyzed per minute per FtsZ monomer [28], after 10 minutes, if no nucleotide exchange were possible, the filament would accumulate GDP at most of the interfaces. We see no evidence that the interaction between monomers changes, as would be expected if the GDP generated were not

replaced by GTP.

The quantitative analysis of the depolymerization of open filaments led to another important conclusion: The rupture rate between two monomers depends on the location of the monomers interface. Bonds located at the center of the filament rupture at a slower rate than bonds located at the end. We cannot follow directly the fast rupture rate of the filament because our experimental time resolution does not allow distinguishing a sequential loss of 10 independent monomers from a single fragmentation of a 10 monomer piece. However, we extract the information from comparing the velocity histogram distribution with the computer simulation results. From the mean depolymerization rate and the strong asymmetry of the histogram, we can discard both a fragmentation with a slow rupture rate v_o at random locations and a sequential depolymerization of single monomers from the filaments ends with a fast rupture rate v_1. A size-biased fragmentation, approximately 30 times more effective for short filaments than the uniform slow fragmentation process, is what best describes the observations. Because there are more possible fragmentations of long pieces than of small ones, the mean depolymerization rate of open filaments ends up being about 10 times faster than the estimate from the v_o value obtained from the rings.

The assumption that filament ends hydrolyze faster has also been suggested by other groups. Molecular modeling studies indicate that the effective hydrolysis rate is larger at monomers located near filament ends than it is between monomers located within the filament [99]. Both effects, higher hydrolysis rate and faster monomer diffusion at the ends, could contribute to give a faster irreversible separation of the end monomer with a frequency v_1 much larger than the v_o found for monomer-monomer interactions in the central part of the filaments and associated to the irreversible opening of rings.

Combining the information provided by the study of the resilient closed rings and the depolymerization of the open filaments allows us to reach yet another important conclusion: FtsZ filaments show no sign of cooperative depolymerization. Tubulin, the related eukaryotic cytoskeletal protein, shows dynamic instability [100], a cooperative depolymerization process that is not observed here for FtsZ filaments. All monomer-monomer interfaces are equally competent for annealing, opening or closing randomly. These results are consistent with recent biochemical data that have also shown that all the GTP-bound sites within FtsZ filaments are noninteracting and catalytically active [30].

Associating the GTPase hydrolysis cycle to filament depolymerization

has remained a challenge difficult to address from bulk steady-state experiments. It has been suggested[29] that the mechanisms that contribute to FtsZ dynamic behavior include random fragmentation within the protofilament following GTP hydrolysis, and that dissociation of subunits occurs either at the end or within the filament, mainly at GDP containing subunits, allowing also for annealing of fragments of different protofilaments. Our data qualitatively refine the picture. We have confirmed that the hydrolysis events within a filament are indeed random, independent from each other, and that rupture can occur, although at different rates, both within and at the filament ends.

Because there is no change in the curvature of the rings along the full nucleotide hydrolysis-exchange cycle, another clear result is that monomers within filaments are equivalent and that, regardless of their GTP or GDP content, all are capable of sustaining a curved configuration. This structural plasticity, understood as a structural state of the polymer not associated to the chemical state of its bound nucleotide[101] has been previously described for tubulin and actin. We observe that it is also relevant in FtsZ polymers and should be considered in future theoretical models to explain the force generation mechanisms.

Finally, the data presented here describing how individual filaments depolymerize help to understand the more complex situation found *in vivo*. Recent experiments describing the behavior of FtsZ filaments attached to supported lipid bilayers[102] indicate that the essential traits of the dynamic behavior of the FtsZ filaments observed on mica[12] are preserved on lipid surfaces, in spite of the formation of higher order aggregates. Accordingly, experimental evidence shows that the FtsZ ring in cells retains a dynamic behavior[103]. It is therefore expected that the dynamic character of the filaments that allows for filament rupture and annealing *in vitro* will play an important role in the functional force-generating mechanism *in vivo*.

3.6 Supplementary Information

3.6.1 Filament shape parametrization

For each atomic force microscopy (AFM) image, the height of every pixel (z) was read and the average ($\langle z \rangle$) and standard deviation (σ_z) calculated, discarding all pixels below the threshold level $h_{threshold} = \langle z \rangle + 2\sigma_z$. The

selected pixels were then grouped in clusters larger than 25 pixels. Smaller clusters were discarded because they often corresponded to static blobs of protein. The clusters selected described the protein strands. Once these filaments were identified, the center of mass of the clusters was calculated and used as center for the polar coordinate expressed by the pairs $\{(r_i, \theta_i)\}_{i=1}^{N}$, being N the number of clusters. In this coordinate system we can describe the filament with a harmonics series:

$$r(\theta) = \frac{1}{2}a_0 + \sum_{n=1}^{5} \left[a_n \cos(n\theta) + b_n \sin(n\theta)\right] \tag{3.2}$$

The series is truncated at the fifth term in order to have enough flexibility to adjust any filament. The fitting procedure provides the values for the coefficients (a_n, b_n) that minimize the function D^2

$$D^2 = \sum_{i=1}^{N} \left[r_i - r(\theta_i)\right]^2 + \epsilon \sum_{n=1}^{5} n^3 \left(a_n^2 + b_n^2\right) \tag{3.3}$$

The first term is the contribution of the square distance between the pixel clusters and the fitted curve, and the second is a contribution that penalizes the higher order harmonics to avoid overfitting by high-frequency oscillations. The weight of this second contribution relative to the first one is determined by the parameter ϵ. It was chosen to be $\epsilon = 0.1$, but there were no detectable differences in the fitted curve for small variations in ϵ. This analysis can also be applied to open filaments if the θ value is restricted to a limited range. Figure 3.6 illustrates that the procedure gives a smooth and fairly accurate fit of the open filaments (figure 3.6 A) and the closed rings (figure 3.6 B). The integration of the analytical curve $r(\theta)$ provides the filament length at each frame. Figure 3.6 C shows the time evolution of the length of a given filament $L(t)$.

3.6.2 Statistical analysis of FtsZ polymers at single-filament level

AFM images provide information on individual FtsZ filaments. The survival time of each closed FtsZ rings (figure 3.4) and the decay in length with time of open filaments (figure 3.5) can be measured directly. These experimental data are beyond the usual description of the chemical reaction

kinetics, which analyzes the average depolymerization in a large ensemble of filaments, disregarding their size distribution. Here we use simple examples to illustrate the statistical methods that are used to extract all the information provided by the *single-filament* data from AFM images.

For the analysis of closed rings, our experimental results show clearly that the ring survival time depends on ring size. On average, large rings disappear sooner than small rings. A coarse description within the frame-

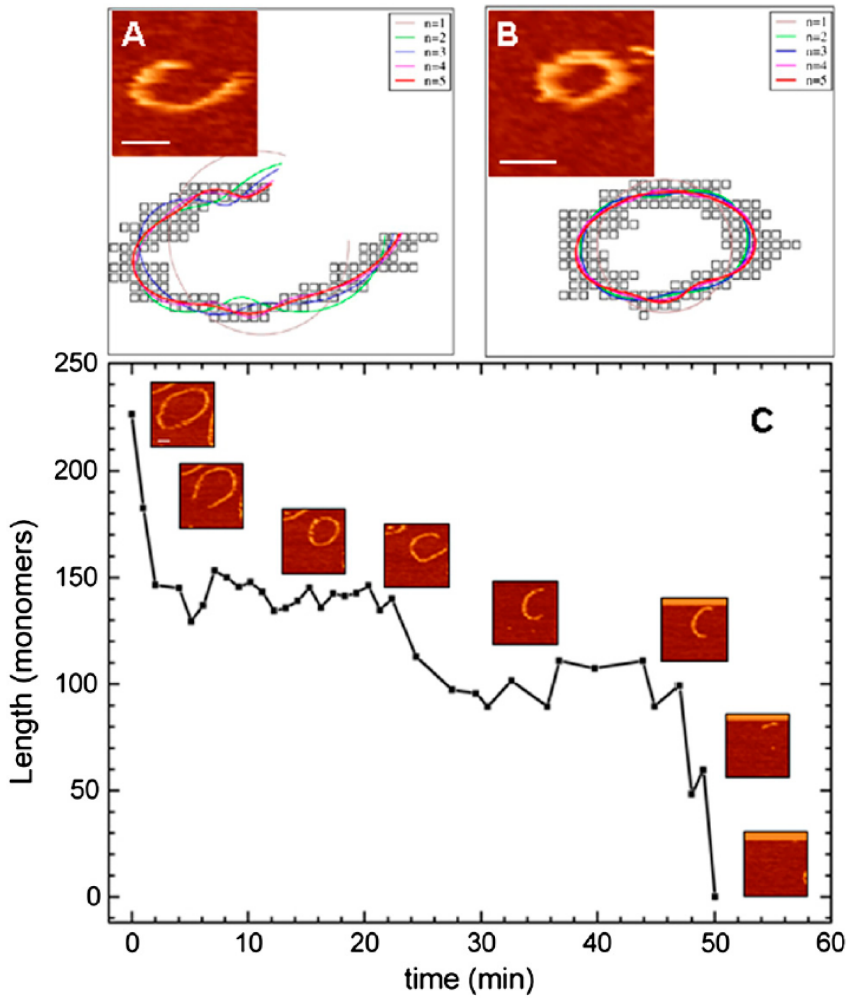

Figure 3.6 – Filament shape parametrization. Fitted curves for a FtsZ ring and filament using different harmonics. A and B show the fit to the digitalized image for different value of n. C illustrates the time evolution of the filament length estimated from the AFM images. (Scale bars: 100 nm)

work of the kinetics of chemical reactions would add all the observations together, to get a life-time distribution with a corresponding mean life-time, which would depend on the particular distributions of ring sizes. However, with the statistical treatment described in the section below, we can check the hypothesis that the reaction rate for the irreversible depolymerization is proportional to the ring size, and get a breaking rate per bond that is independent of ring length. This information can then be "exported" to the analysis of open filaments.

For the depolymerization velocity of open filaments (figure 3.5), our analysis goes beyond the usual reaction kinetics concerned with mean values in systems with a large number of molecules. We use the tools of the statistical physics of small systems to analyze the fluctuations of depolymerization velocity around its mean value. This analysis is crucial to extract all the information provided by the single-filament data from AFM images, as demonstrated below in the simple example in *Statistical distribution for the instantaneous depolymerization velocities of single FtsZ filaments.*

Analysis of the lifetimes for FtsZ closed rings with different sizes (collective kinetics for multiple reactions with proportional rates)

Considering FtsZ rings in the sample and their irreversible depolymerization a process triggered by a single reaction with a rate v_o in a purely random way, then the time evolution equation for the concentration of these rings $Z_{\text{rings}}(t)$ would be:

$$\frac{dZ_{\text{ring}}(t)}{dt} = -v_o Z_{\text{ring}}(t), \tag{3.4}$$

and its solution would give the number of rings at any time as

$$Z_{\text{ring}}(t) = Z_{\text{ring}}(0) exp(-v_o t). \tag{3.5}$$

The mean survival time of a ring could be calculated as

$$\langle T \rangle = \frac{\int_0^\infty T\ Z_{\text{ring}}(t)dt}{\int_0^\infty Z_{\text{ring}}(t)dt} = \frac{\int_0^\infty T\ e^{-v_o t}dt}{\int_0^\infty e^{-v_0 t}dt} = v_o^{-1}, \tag{3.6}$$

so that the reaction rate v_o could be obtained directly from the mean survival times of the rings. If our experimental data (presented in figure 3.4) were analyzed in this way, distinguishing as different populations

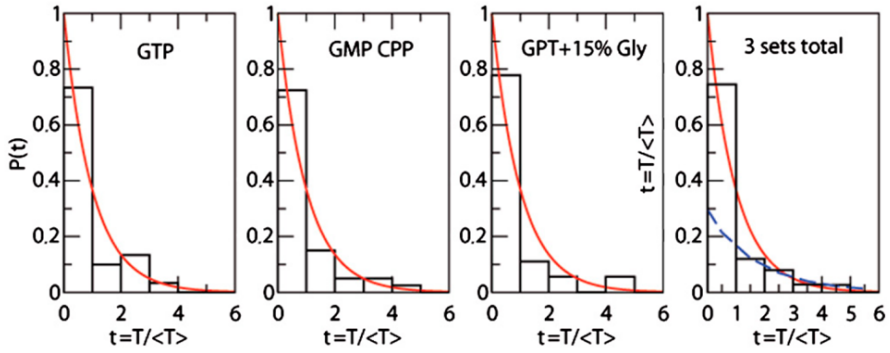

Figure 3.7 – Lifetime probability distributions of FtsZ closed rings. Normalized histograms for the survival time of FtzS rings in different nucleotide buffers. The time is scaled with the mean value $< T >$ for each set. The red lines correspond to the exponential decay $P(\tau) = exp(-\tau)$ predicted by eq.(3.4).The blue dash line is a one exponential fit that illustrates that one exponent can only account for the slow tail but not the behavior of the full histogram

of rings the ones grown under different experimental conditions, we would get: $\langle T \rangle = 6.45$ min for GTP in the normal buffer, $\langle T \rangle = 13.13$ min for GMP, and $\langle T \rangle = 8.88$ min for GTP with 15% glycerol; giving reaction rates $v_o = 0.15$, 0.076, and 0.11 per minute respectively. That would be the only information available from the experimental data with the simple analysis of the irreversible depolymerization as a single random process over the whole experimental sample.

However, there is more information contained in these data sets. In figure 3.7 we present the (normalized) distribution for the observed times for FtsZ rings, in terms of the reduced time $\tau = T/\langle T \rangle$ for each buffer condition. According with equations 3.5, 3.6, this distribution should be a pure exponential, $P(\tau) = exp(-\tau)$, but the experimental results seem to deviate from that simple form.

The statistics are not very good, because the number of rings is not very large, but (because we have already normalized the times in each data set with its own mean value), we may accumulate the three sets in the single histogram. The better quality of the accumulated histogram confirms the nonexponential shape of $Z_{\text{rings}}(t)$: The decay is too rapid at short times and too slow at the tail of the distribution.

This representation of the experimental data shows that the depolymerization of the rings cannot be described by a single reaction rate v_o to

represent all the rings in each sample. We have to look for the additional elements that explain why the depolymerization of the rings deviates from the simple behavior defined by eq. (3.4). The experimental data provide the length of individual rings. This information is very useful since its shows clearly that longer rings disappear faster than smaller ones. Having a mixture of rings with different sizes gives a complex (nonexponential) behavior to the time-decay of the total population of rings.

Let us consider two subpopulations of FtsZ rings, Z_a and Z_b, shrinking through different reaction rates v_a and v_b respectively (e.g., because they have different sizes $N_b = 2N_a$, and that is reflected in v_b=$2v_a$). The concentrations of each component would follow a simple exponential decay $Z_a(t) = Z_a(0)exp(-v_a t)$ and $Z_b(t) = Z_b(0)exp(-v_b t)$, but if we treat all of them together, the total number of rings $Z_{\text{rings}}(t) = Z_a(t) + Z_b(t)$, evolves

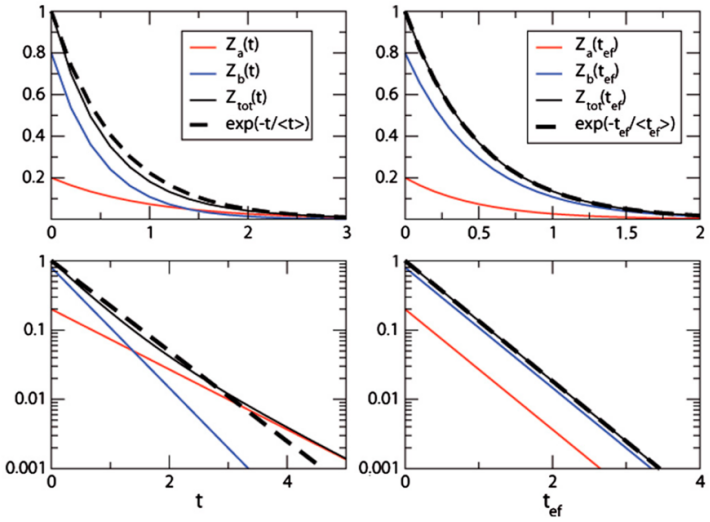

Figure 3.8 – Life time probability distribution for two subpopulations of closed rings with different rupture rates. At the left-hand side, the continuous black line is the distribution $Z_{\text{tot}}(t)$ for the survival times in a system with two sub-populations: a (red line) with initial concentration $P_a(0) = 0.2$ and reaction rate $k_a = 1$ (in arbitrary units), and b (blue line) with $P_a(0) = 0.8$ and $k_b = 2$. The dashed line is the exponential distribution that would describe a single process with the mean reaction rate. The log scale (bottom) shows more clearly the tail of the distributions. At the right hand side the same data are analyzed in terms of the effective time, that takes into account the ratio $k_b/k_a = 2$, and produces a pure exponential decay for $Z_{\text{ef}}(t_{\text{ef}})$.

like:

$$Z_{\text{rings}}(t) = Z_a(0)\ exp(-v_a t) + Z_b(0)\ exp(-v_b t), \tag{3.7}$$

which does not follow the simple equation (3.4).

If we describe the full sample as a whole, the mean survival time would be

$$\langle t \rangle = \frac{v_a^{-2} Z_a(0) + v_b^{-2} Z_b(0)}{v_a^{-1} Z_a(0) + v_b^{-1} Z_b(0)}, \tag{3.8}$$

which depends on the initial amount of rings of each type, $Z_a(0)$ and $Z_b(0)$, and which gives some intermediate value between the two reactions rates v_a and v_b that really describe the depolymerization process in the sample. Figure 3.8, *Left* shows the shape of $Z_{\text{rings}}(t)$, compared with the exponential form $P(\tau) = exp(-\tau)$ of a single process with the same mean value $\langle t \rangle$ as given by equation (3.8). The deviation of $Z_{\text{rings}}(t)$ from the exponential shape is similar to that observed in figure 3.7 for the actual experimental results.

Obviously, in this example, we may do separate analysis of the data for the two subpopulations, to recover the simple exponential distribution for each one, $Z_a(t) = Z_a(0)exp(-v_a t)$ and $Z_b(t) = Z_b(0)exp(-v_b t)$, so that the complex stochastic phenomena behind $Z_{rings}(t)$ is decomposed in its simple components. However, if we have some hypothesis for the ratio between the two reaction rates v_b/v_a (e.g., we may guess that the reaction for b is twofold faster than for a because b rings are twice as large as the a rings), we may check the accuracy of the hypothesis defining effective times, $t_{\text{ef}} = 2t$ for a and $t_{\text{ef}} = t$ for b, and collecting the information of $Z_a(t)$ and $Z_b(t)$ into a single function for equal values of their effective times, $Z_{\text{ef}}(t) = Z_a(2t) + Z_b(t)$. The result, presented in figure 3.8, *Right*, is

$$\begin{aligned} Z_{\text{ef}}(t) &= Z_a(0)e^{-2v_a t} + Z_b(0)e^{-v_b t} = \\ &= (Z_a(0) + Z_b(0))e^{-2v_a t} = Z(0)e^{-2v_a t}, \end{aligned} \tag{3.9}$$

which follows the simple equation (3.4) with a single effective rate $v_{ef} = 2v_a$. Therefore, the basic hypothesis $v_b = 2v_a$ would then be confirmed (or rejected) by the observation (or not) of a pure exponential shape for the distribution of reduced survival times $\tau = t_{\text{ef}}/\langle t_{\text{ef}} \rangle$.

This procedure becomes very useful if, instead of the two components a and b, we have a stochastic process with many simple components, each with a different reaction rates v_N. That is the case for the irreversible

breaking of FtsZ rings with a broad initial distribution of size $P_N(0)$, which would evolve in a complex way,

$$Z_{\text{rings}}(t) = \sum_N P_N(0) exp(-v_N t), \tag{3.10}$$

adding to the nonexponential decay in figure 3.7. The separated analysis of each ring population, $Z_{\text{ring}}(t)$ would be impossible, because we do not have enough observations for each value of N, so that we lack information to get accurate separated fits to $Z_{\text{N}}(t) = P_{\text{N}}(0) exp(-v_{\text{N}} t)$. However, the obvious hypothesis to be tested is that the reaction rates for depolymerization are proportional to the length of each ring, so that, as described above, we define the effective time of a ring with length N as $t_{\text{ef}} = Nt$. As shown in figure 3.4, this description leads to the simple exponential decay of $P(t_{\text{ef}}/\langle t_{\text{ef}} \rangle)$, so that the hypothesis is confirmed: The irreversible depolymerization of FtsZ rings is triggered by independent events at each bond, so that the reaction rate v_o is proportional to N, and the whole process is described by a single reaction rate per bond $v_o = \langle t_{\text{ef}} \rangle^{-1}$, that characterizes all the rings in each nucleotide buffer.

Statistical distribution for the instantaneous depolymerization velocities of single FtsZ filaments

If we consider the simplest depolymerization process, where monomers are released from a filament one-by-one by a purely stochastic process with fixed rate v, then the change of the number of FtsZ filaments with length N, $Z_N(t)$, in a sample with a broad size distribution is given by the reaction kinetic equation

$$\frac{dZ_N(t)}{dt} = -vZ_N(t) + vZ_{N+1}(t) \tag{3.11}$$

for $N \geq 2$. The integration of these coupled equations gives the populations $Z_N(t)$ from the set of initial values $Z_N(0)$, and we could extract any global measure of the sample, like the total number $Z_{tot}(t)$ and the total length of all the filaments $L_{tot}(t)$ as

$$Z_{tot}(t) = \sum_{N \geq 2} Z_N(t), \tag{3.12}$$

$$L_{tot}(t) = \sum_{N \geq 2} N Z_N(t), \tag{3.13}$$

then the total mean length of the filaments in the sample is given by

$$\langle N\rangle(t) = \frac{\sum_{N\geq 2} N\ Z_N(t)}{\sum_{N\geq 2} Z_N(t)} = \frac{L_{tot}(t)}{Z_{tot}(t)} \tag{3.14}$$

If we may neglect the adsorbing boundary at the short filament end of the distribution $Z_N(t)$ (i.e. as far as all the initial filaments still have $N > 2$), the total number of filament is constant

$$\frac{dZ_{tot}(t)}{dt} = -v\sum_N Z_N(t) + v\sum_N Z_{N+1}(t) = 0, \tag{3.15}$$

and the mean length decays steadily at the rate v

$$\frac{d\langle N\rangle(t)}{dt} = -v\frac{\sum_{N\geq 2} N\ [(Z_N(t) - Z_{N+1}(t)]}{Z_{tot}(t)} = -v\frac{Z_{tot}(t)}{Z_{tot}(t)} = -v, \tag{3.16}$$

$$\langle N\rangle(t) = -vt \tag{3.17}$$

as it may have been written directly, since all the filaments are shrinking at that mean rate. Therefore, the depolymerization rate v could be directly extracted from experimental observations for the mean decay of the filament length, i.e. the mean depolymerization velocity, as

$$\langle V\rangle = \frac{\langle N\rangle(t_f) - \langle N\rangle(t_0)}{t_f - t_0} = -v. \tag{3.18}$$

However, the information obtained experimentally by the estimation $\langle V\rangle$ is not enough to characterize the depolymerization mechanism. If we consider a four-by-four mechanism (i.e., depolymerization occurs taking off pieces of four monomers from the filament with a rate v'), the reaction kinetics would be described now by

$$\frac{dZ_N(t)}{dt} = -v'Z_N(t) + v'Z_{N+4}(t), \tag{3.19}$$

and we may follow the same argument as above to get the mean depolymerization rate as

$$\frac{d\langle N\rangle(t)}{dt} = -v'\frac{\sum_{N\geq 2} N\ (Z_N(t) - Z_{N+4}(t))}{Z_{tot}(t)} = -v'\frac{4Z_{tot}(t)}{Z_{tot}(t)} = -4v', \tag{3.20}$$

$$\langle V\rangle = \frac{\langle N\rangle(t_f) - \langle N\rangle(t_0)}{t_f - t_0} = -4v', \tag{3.21}$$

therefore $\langle V \rangle$ can not be used to discern between a basic depolymerization mechanism that releases the monomers, one-by-one, at a rate $v \equiv v_1$, and other mechanism in which the monomers are released in bunches of 4 monomers but fourfold slower-i.e., with a rate $v' \equiv v_4 = v_1/4$. Moreover, any stochastic combination of both processes could be interpreted either as one-by-one or as four-by-four mechanism.

As will be shown below, analysis of the distribution of instantaneous velocities can distinguish between the two depolymerization mechanisms described above. Notice that the principal advantage of AFM is that we get direct access to the time evolution of single filaments and it is possible to construct the whole instantaneous velocities histogram between two AFM frames. In contrast, such information is not accessible from any other experimental method that looks at ensembles and collects the mean size value from a broad distribution of filament lengths.

For a set of images of one filament taken at Δ_t intervals, we get a time series $N(t_i)$ for $t_i = i\Delta_t$, and $i = 0, 1, 2, ...$ The depolymerization velocity in each time interval is given by

$$V(t_i) = \frac{N(t_{i+1}) - N(t_i)}{\Delta_t} \tag{3.22}$$

then in the one-by-one monomer depolymerization mechanism with a rate v, the observed velocities would be $V = 0, 1/\Delta_t, 2/\Delta_t, 3/\Delta_t$,..., n/Δ_t that correspond to have none, one, two, three,..., n releasing events in the time interval $t_{i+1} - t_i = \Delta_t$. The probability for each possible value of V is given by a Poisson distribution

$$P\left(V = \frac{n}{\Delta_t}\right) = \frac{e^{-v\Delta_t}(v\Delta_t)^n}{n!}. \tag{3.23}$$

In contrast, with a depolymerization in bunches of four monomers with rate $v' = v/4$, would produce only values $V = 0, 4/\Delta t, 8/\Delta t, ...,$ with probabilities

$$P\left(V = \frac{4n}{\Delta_t}\right) = \frac{e^{-v'\Delta_t}(v'\Delta_t)^n}{n!}. \tag{3.24}$$

The mean value of n from (3.23) would be $\langle n \rangle = v\Delta_t$, so that the mean depolymerization velocity is $\langle V \rangle = \frac{\langle n \rangle}{\Delta_t} = v$, as expected. Similarly, from (3.24) we get $\langle n \rangle = v'\Delta_t$, so that the mean depolymerization velocity is $\langle V \rangle = \frac{4\langle n \rangle}{\Delta_t} = 4v' = v$. The two processes would give again the same mean depolymerization velocity, but now we may easily discern between the two alternatives from the very different shape probability distributions (figure 3.9).

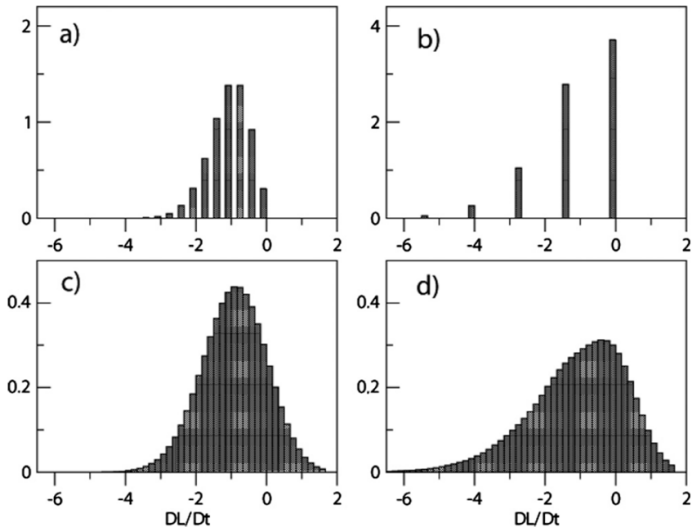

Figure 3.9 – Poisson probability distributions of depolymerization velocities for sequential shrinking mechanisms. The distribution of chain length that would be observed in the simple examples described here. a) is the Poisson distributions for one-by-one depolymerization events eq.3.23; b) represents eq.3.24 for the hypothetical four-by-four depolymerization. Both cases have the same mean value (taken as arbitrary unit), and they correspond to observations times relatively large, $\Delta_t = 3$, so that every "observed" change of length may include several "depolymerization events". With the ideal resolution of these graphs, the difference between the two cases would be obvious: a) presents non-zero probabilities for all the values corresponding to an integer number of monomers, whereas in b) the gap between observed values for "instantaneous" depolymerization rates is four times larger. In the bottom distributions we have added a Gaussian noise to the results, so that the gaps between observed rates have disappeared. Nevertheless, the shape of the distributions still allows one to distinguish between the one-by-one ((a) and (c)) and the four-by-four ((b) and (d)) cases.

In particular the typical deviation for the velocity distributions would be $\sigma_V \equiv \sqrt{\langle V^2\rangle - \langle V\rangle^2} = \sqrt{v/\Delta_t}$ from (3.23) and $4\sqrt{v'/\Delta_t} = 2\sqrt{v/\Delta_t}$ from (3.24)-i.e., with equal values of $\langle V\rangle = v$ the typical deviation in the four-by-four depolymerization mechanism would give twofold larger than for the one-by-one. Therefore, the experimental estimation of $\langle V\rangle$ and σ_V would provide the information to discern between depolymerization processes. Moreover, if we can get accurate results for the whole probability

distribution $P(V)$, and it shows a non-Poissonian shape as in figure 3.5, we would learn that the polymerization reaction follows a more complex reaction pattern than a mixture of one-by-one, four-by-four, or other unbiased depolymerization steps. In this case of such a sized biased process, to get an analytical prediction of P(V) the use of computer simulations (with simple parametric forms for the size dependence of the fragmentation rates) provides the simplest way to compare with the experimental distributions.

To conclude, notice that the method is still valid for relatively long time intervals (in the series of AFM images we have $\Delta_t \approx 1$ min), so that $v\Delta_t$ may be relatively large (~ 10 in our case) and the observed depolymerization steps are usually composed of several basic steps. The probability distributions (eq. 3.23 and 3.24) are still valid, although for large Δ_t, they become narrower, $\sigma_V \sim 1/\sqrt{\Delta_t}$, and it would be more difficult to discern the shape. Also, there is an inherent noise from the imaging and the parametrization of the filaments, to get $N(t)$, so that the hypothetical probability distributions $P(V)$ are blurred, and we even observe some positive values of V (spurious polymerizations from the uncertainty in the experimental characterization of the filament length). Nevertheless, we have probed here that, with a feasible number of observations, we may get enough resolution in $P(V)$ to discard both a one-by-one depolymerization and the unbiased fragmentation.

3.6.3 Langevin computer simulations

Protein monomers are modeled as beads of a chain linked by elastic springs that give an optimal distance between beads and an optimal angle between bonds, with thermal fluctuations around these optimal values, assuming that each protein monomer moves in a viscous fluid, with limiting velocity proportional to the instantaneous force. The force on each monomer has a deterministic component coming from the springs that links it to its neighbours along the chain, and a stochastic component that represents the thermal noise-i.e., the molecular collisions with the bath.

The characteristics of the springs and the thermal bath were tuned to reproduce the distribution of filament shapes observed in AFM images for short FtsZ filaments, polymerized with a slowly hydrolyzing GTP analogue[104]. A computer simulation using this same model may be used to describe the separation of the filaments fragments following the elimination of one of the spring bonds, to mimic the breaking of a bond along the chain.

Size dependent diffusion effect of FtsZ filament fragments

We have simulated the breaking of open filaments with N=100 monomers each. The initial shapes of the filaments were selected along the configurations of a long Langevin simulation in thermal equilibrium at room temperature. For each of these configurations, a bond was broken, either at the middle point, breaking the filament in two parts with $N_a = N_b = 50$ each, or at one end of the filament, separating a single monomer $N_a = 1$ from the remaining $N_b = 99$ monomers. At the breaking time, the monomers started with their original (bounded) coordinates, but the spring joining them was deleted to simulate the effect of the GTP hydrolysis. Then the simulation was run for the two fragments of the filament, to follow the time evolution of distance and relative angular orientation between the two previously associated monomers. These variables follow a Brownian diffusive dynamics, so that the distance and the angular mismatch change in a random way but, on average, they move away from their initial values as shown in Figure 3.10. The main difference between the diffusion of an isolated monomer and that of a monomer still linked to a longer filaments appears in the relative angle $\Delta\phi$ between their orientations. It increases more than threefold only 0,1 s after rupture.

The time scale for the Langevin simulation has been calibrated from the comparison of the fluctuations in the shape of closed rings observed in AFM images and in Langevin simulations with the same model (details to be published). According to the hydrolysis rate for GTP, ≈ 8 min^{-1}, the FtsZ bonds become weaker every $7-8$ seconds, and they would open to replace the GDP by a fresh GTP from solution. The small time fraction of ($\sim 0.05-0.1$ s) needed for that replacement would be enough to produce an important angular mismatch in the orientation of an isolated monomer, so that after capturing a GTP, the FtsZ monomer may diffuse away from the remaining filament, instead of finding its way to remake the broken bond. In contrast, when the breaking of the filament leaves two large fragments, their typical diffusion during same time would be of only a few degrees of angular mismatch (and a few nanometer of distance), making more likely that the bond is sealed after the nucleotide exchange. Notice that a quantitative estimate for the frequencies of the depolymerization reaction rates would require a description of the GTP hydrolysis and replacement at molecular level, and the above estimations can only be used at a qualitative level as support to the hypothesis that the fragmentation rate may depend on the fragment size.

Size biased fragmentation process for FtsZ filaments

We have run computer simulations for the fragmentation of 10^5 filaments, with initial sizes following the distribution observed for closed rings (figure 3.1), assuming that a filament with size $< N_o >$ may undergo any possible fragmentation in two pieces of size N_a and $N_b = N_o - N_a$, but with a frequency that depends on the size of the fragments.

$$v\left(N_a, N_b\right) = v_o + v_1 \left(e^{-N_a/L} + e^{-N_b/L}\right). \tag{3.25}$$

The parameter v_1 represents the rupture frequency of short filaments (i.e., with size $N_{a,b} \ll L$) , whereas the value of v_o gives the breaking frequency of long fragments (i.e., with size $N_{a,b} \gg L$). Fragmentations

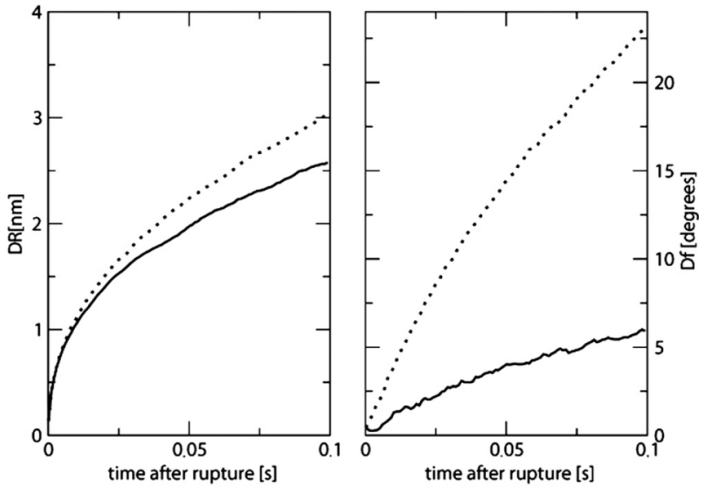

Figure 3.10 – Distance and relative orientation between FtsZ fragments after a rupture event. The standard deviation for the distribution of distances (*Left*, in nanometers) and relative angle (*Right*, in degrees) between the ends of a broken bond in a set of Langevin simulations for model FtsZ filaments. The growth of ΔR and $\Delta\phi$ with the time (in seconds) after the breaking of a polymeric bond along the filament reflects the diffusive changes in the shapes of the filaments (see text). The full lines correspond to the fragmentation of a filament with $N = 100$ monomers into two equal pieces ($N_a = N_b = 50$). Other fragmentations with $N_a \neq N_b$ give similar results unless one of the pieces is very small. The dotted lines correspond to the separation of a single monomer ($N_a = 1$, $N_b = 99$), that shows faster diffusion in distance and particularly in the relative angle.

are attempted at randomly chosen point and accepted with a probability $P(N_a, N_b)$ proportional to $v(N_a, N_b)$. As done in the analysis of the experimental depolymerization histories, after a fragmentation, we keep only track of the larger segment of the filament, so that we cut away a bunch of $N_{cut} = min(N_a, N_b)$ monomers, and iterate the process until the larger fragment becomes shorter than 10 monomers.

The value of v_o is keep to be the irreversibly opening frequency obtained from the analysis of closed rings (Table 3.1), whereas v_1 and L are used to get the same mean value and asymmetry of the experimental instantaneous depolymerization velocity distribution. We have obtained the best fits (black full line in figure 3.5) with $v_1/v_o = 30 \pm 5$ for both GMPCPP and GTP plus glycerol buffers. Instead the values found for L are 30 ± 6 for GMPCPP, whereas for GTP plus glycerol the experimental results are better fit using $L = 15 \pm 4$, in good accordance with the fact that shorter filaments may move similar distances in a more viscous medium than longer filaments in the aqueous buffer. These values for v_1 and L may only be considered as semi-quantitative predictions because the specific choice of the parameters in eq. 3.25 is reasonable but by no means unique, and the fit to the experimental data leave large error bars. Nevertheless, the qualitative interpretation of the depolymerization as random fragmentations with an enhanced frequency for short fragments is very robust and well founded.

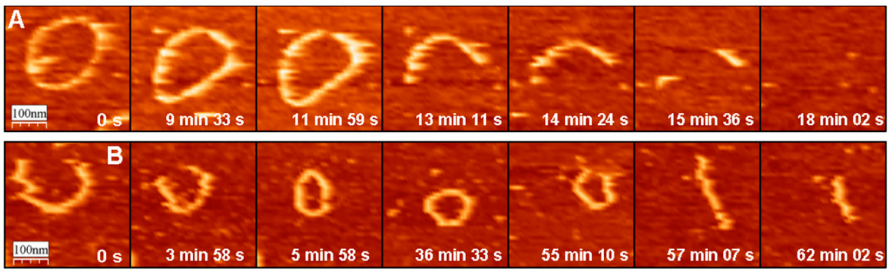

Figure 3.11 – FtsZ filaments imaged in acid buffers. The panel shows the time evolution of FtsZ filaments imaged in acid buffers. Panel (A) pH=6.5. Panel (B) pH=5.0

pH	7.5	6.5	5.0
No. rings	243	176	69
$\langle N \rangle \pm \sigma_N$	103 ± 26	99 ± 28	80 ± 16
$\langle T \rangle$ min	6.5	22.0	25.5
$\langle T_b \rangle$ min	670	2200	2000
v_o min^{-1}	0.0015	0.00045	0.0005

Table 3.2 – The number of observed FtsZ rings, their mean size and size dispersion (in number of monomers), and the mean time for which each ring is observed in successive AFM frames, with buffers of different acidity in the presence of GTP

3.6.4 Videos

The videos can be found in the web page:

http://www.pnas.org/content/109/21/8133.long

Closed rings dynamics

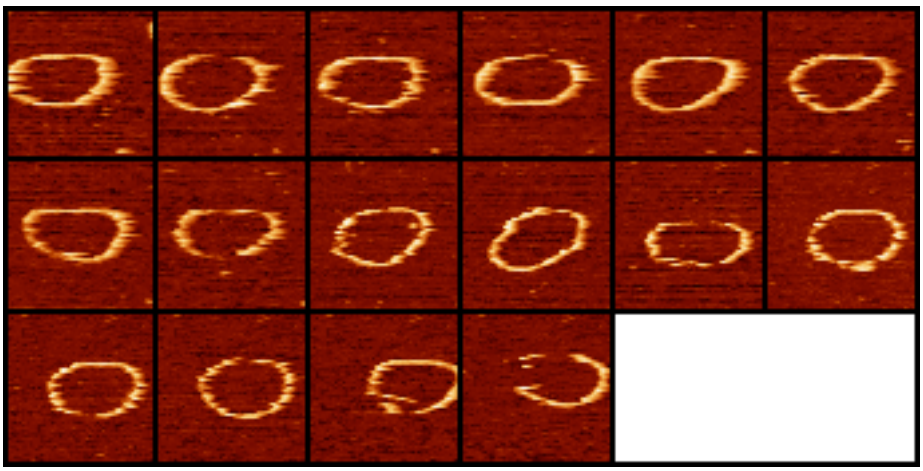

Figure 3.12 – Video S1a-Closed rings in buffer at pH 7.5 with GTP. Image size is 400 x 400 nm and time lapse between frames is $\sim$ 4 min

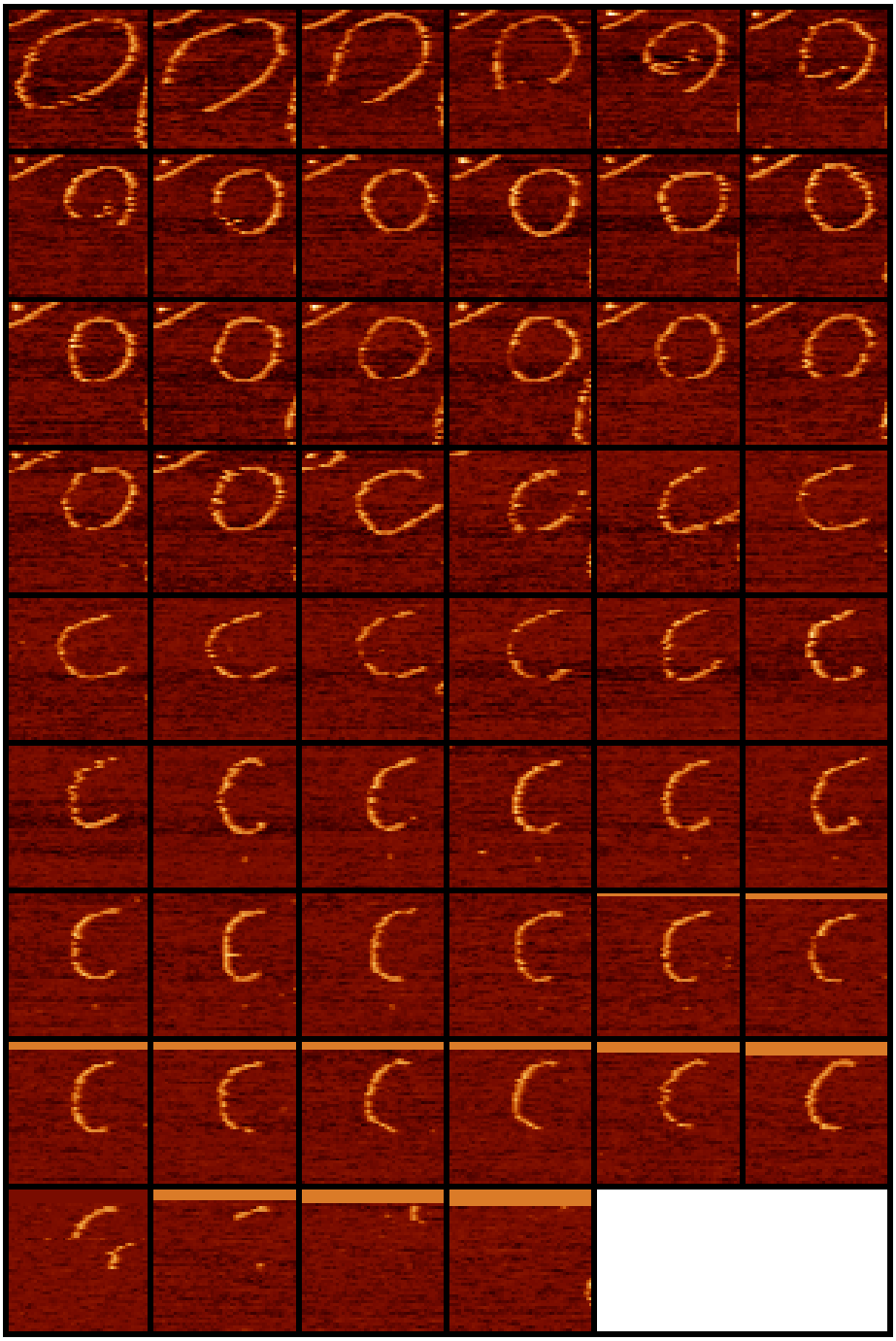

Figure 3.13 – Video S1b-Closed rings in buffer at pH 7.5 with GMPCPP. Image size is 487 x 487 nm and time lapse between frames is ∼1 min

Open filaments depolymerization

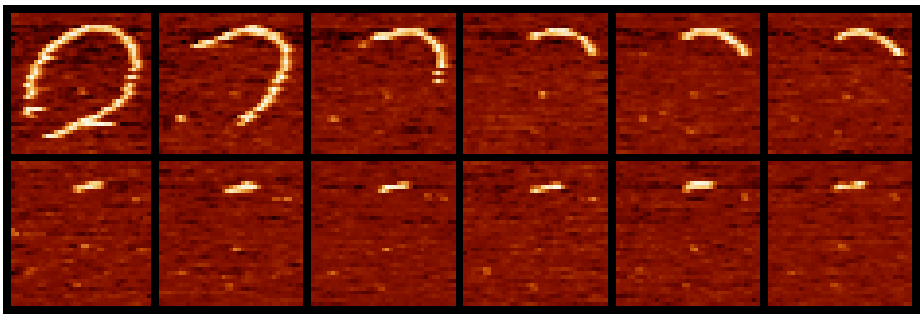

Figure 3.14 – Video S2a-Open filaments depolymerization in buffer at pH 7.5 with GMPCPP. Image size is 366 x 366 *nm* and time lapse between frames is ∼1 min

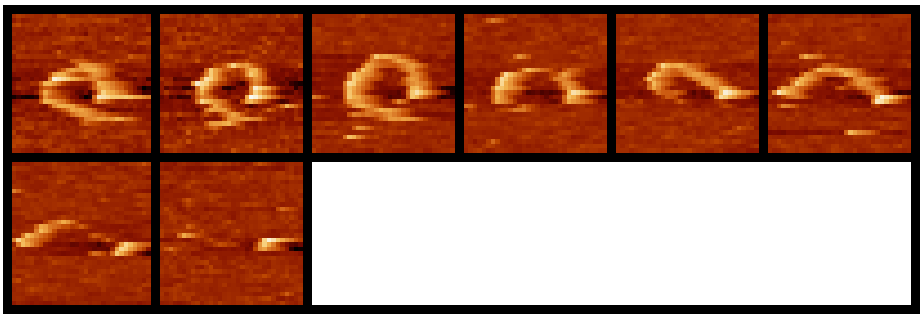

Figure 3.15 – Video S2b-Open filaments depolymerization in buffer at pH 7.5 with GTP plus 15 % glycerol. Image size is 488 x 488 *nm* and time lapse between frames is ∼1 min

Filaments dynamics in acidic conditions

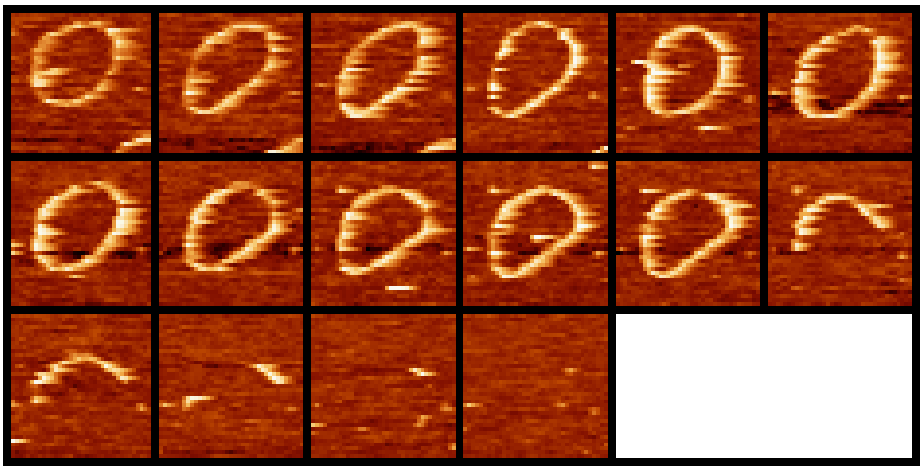

Figure 3.16 – Video S3a-Filaments dynamics in buffer at pH 6.5 with GTP. Image size is 366 x 366 nm and time lapse between frames is $\sim$1 min

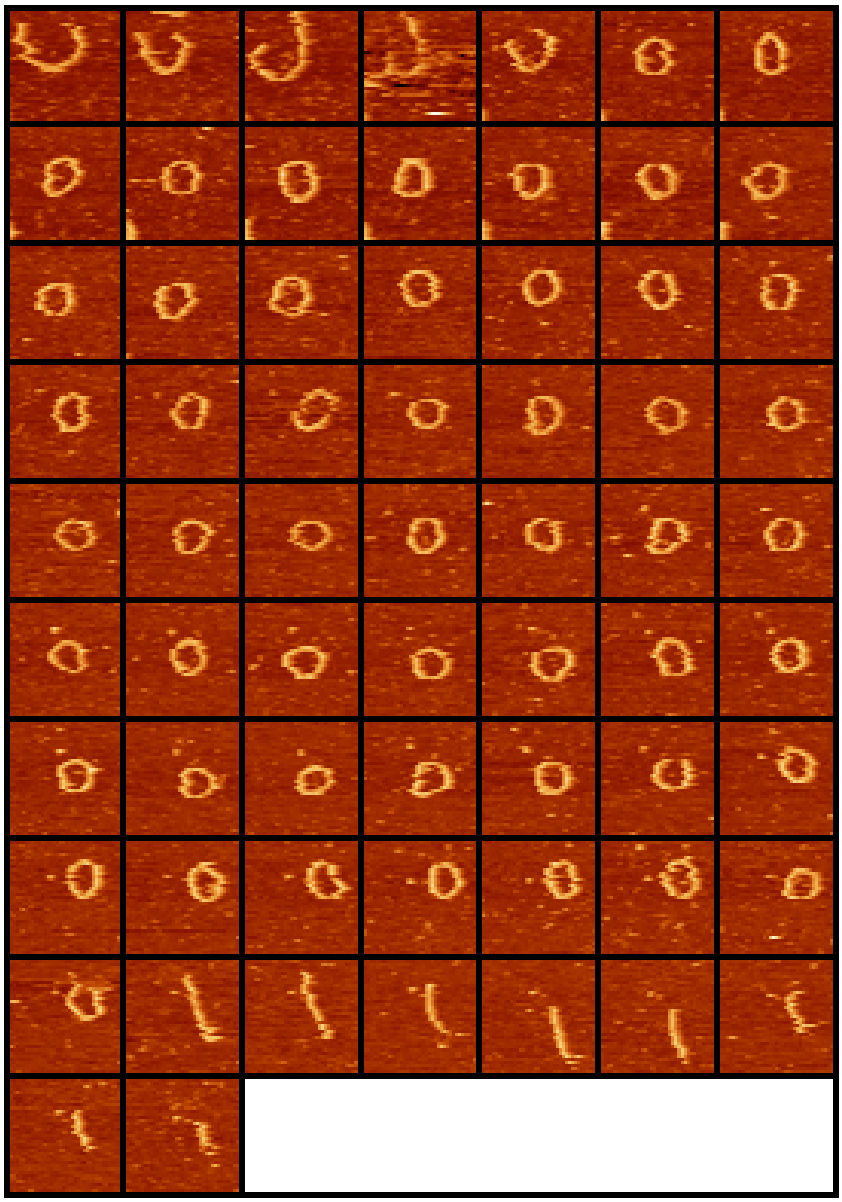

Figure 3.17 – Video S3b-Filaments dynamics in buffer at pH 5.0 with GTP. Image size is 366 x 366 *nm* and time lapse between frames is ∼1 min

Chapter 4

Dynamic collective behavior of FtsZ filaments

Abstract

In this chapter we report experimental observation of the collective behavior of FtsZ filaments adsorbed on mica. Instead of isolated protofilaments we follow the structure and dynamics of many FtsZ filaments able to aggregate laterally. Atomic force microscopy (AFM) images were taken under buffer solution in the presence of GTP registering the shape evolution of filament aggregates at different surface densities. We observed a plastic structural behavior where filaments readapt their shape depending on the surrounding environment. From high to low surface coverage filaments formed from closed packed networks to isolated rolled aggregates.

The rich polymorphism of FtsZ aggregates was used to formulate a pair-wise interaction model between FtsZ monomers in which curvature, flexibility, and lateral attraction are the relevant traits of

FtsZ polymers. Monte Carlo (MC) simulations predict different aggregate shapes depending on the model parameters. We estimated quantitatively the monomer-monomer interaction energies comparing the shapes of the aggregates obtained by MC simulations and the shapes observed experimentally. The energies that reproduce the AFM observations both at high and low surface coverage were selected. Finally, we demonstrated that curvature, flexibility, and lateral attraction comprise a minimal set of features that accounts for the plasticity of FtsZ filaments.

4.1 Introduction

It is well known that FtsZ polymerizes forming single-stranded protofilaments with a strong tendency to aggregate laterally in higher order structures depending on the reaction conditions (see section 1.2.2 in chapter 1). The structure of these FtsZ aggregates has been previously characterized by electron microscopy (EM), providing a fixed snapshot of the protofilament arrangement. In contrast, AFM images acquired under buffer solution allow to obtain not only a high resolution structural information of the filament aggregates but also dynamic information on the rearrangement and shape evolution of the of FtsZ polymers.

In 2005, the dynamics of FtsZ filaments under buffer solution in the presence of GTP was directly visualized in real-time by AFM [12]. In this chapter we have followed FtsZ filaments adsorbed on mica in similar conditions, obtaining the same collective behavior. The observed filaments were highly dynamic polymers, continuously rearranging with frequent reorganizations of their longitudinal bonds. They also showed spontaneous curvature, high flexibility (compared to eukaryotic protein filaments like actin or tubulin [105]), and a strong tendency to form rolled aggregates.

The rich polymorphism observed indicates a plastic behavior for FtsZ polymers. The constrains imposed by the surrounding environment determined the arrangement of the filaments at different surface coverages. A theoretical model in terms of FtsZ monomer-monomer interactions has been developed to study quantitatively this plasticity. Four parameters are included as basic traits of the FtsZ filaments: the polymeric (GTP-mediated) monomer-monomer bonding energy, the flexibility and preferential angle of the bond between monomers, and the lateral attraction between neighboring filaments. Monte Carlo (MC) simulations were run in a 2D fine-grained triangular lattice to reproduce the complex polymorphic filament aggregates observed experimentally. The comparison of FtsZ filament aggregates predicted by the model with the AFM images allows us to obtain a range of values for the interaction energies between FtsZ monomers. The model is able to reproduce from high to low protein surface coverage.

The features included in the model (labile longitudinal bond, curvature, flexibility and lateral attraction) comprises a minimal set of interactions that accounts for the collective dynamic behavior of FtsZ filaments, i.e. all the interactions must be connected in the simulations to reproduce the experimental data. We conclude that it is the balance between the energetic parameters what determines the plasticity and rich polymorphism of FtsZ

filaments.

4.2 Atomic Force Microscopy Images

Atomic force microscope images of *E. coli* FtsZ polymerized in the presence of GTP adsorbed on mica were taken with a microscope from Nanotec Electrónica (Madrid, Spain) operated in the jump mode[94]. Silicon nitride tips with a force constant of 0.05 N/m were used. A drop of the solution with the *E. coli* FtsZ polymers (formed upon addition of 10 mM GTP to FtsZ protein solutions in Tris 50 mM, pH 7.5, 0.5 M KCl, and 5 mM $MgCl_2$ buffer) was incubated over freshly cleaved mica. After incubating for a few minutes, samples were washed extensively with working buffer and imaged under buffer solution containing 1 mM GTP. *E. coli* FtsZ was purified by the calcium-induced precipitation method following the procedure described previously[10].

Figure 4.1 shows a representative time evolution of FtsZ polymers in the presence of GTP. Initially a highly dense layer of filaments was observed. As time evolves partial depolymerization and desorption of FtsZ filaments produced holes, allowing the filaments to rearrange forming curved aggregates. This result is in good agreement with previous work where the time evolution was described in detail[12], showing opening and reannealing and lateral attraction of the filaments as the essential events during the rearrange process.

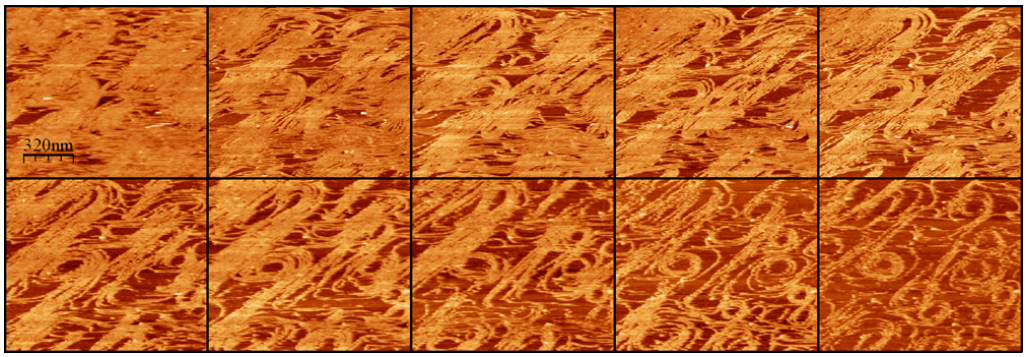

Figure 4.1 – Evolution of FtsZ filaments on mica surface. Time lapse image sequence of FtsZ filaments on mica surface in the same area from high to low coverage. Time between frames is ~ 4 min

4.3 Model for FtsZ filaments on planar surfaces

We will now summarize the basic principles and assumptions of the model used to analyze the AFM experimental data. Previous attempts to describe the collective behavior of FtsZ filaments have used coarse-grained lattice models [84,87,106]. These models include a strong polymeric bond, along the filament direction, and the weaker lateral attraction along the perpendicular direction, but they are too rough to include the flexibility and on-plane spontaneous curvature of the filaments. An off-lattice chain model has also been used [97,104] to analyze the balance between flexibility, spontaneous curvature and lateral attractions using Langevin dynamics simulations. This model did not include the formation and rupture of longitudinal bonds and was compared with AFM images taken in the presence of non hydrolisable analogue of GTP favoring permanent rather than volatile polymeric bonds.

To include a labile longitudinal bond, the filament spontaneous curvature and flexibility, and a lateral attraction, the model was built as follows. Protein FtsZ monomers were described at coarse level far from the atomistic detail (figure 4.2 A). One monomer includes an excluding volume core (gray sites), the head-to-tail geometry of its polymeric direction represented as an row running from their minus end (T7 loop-region) to their plus end (GTP binding site) (vertical/horizontal dashed sites), and a surrounding

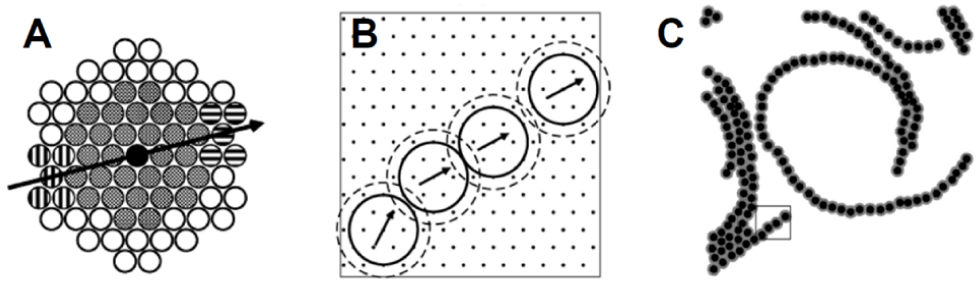

Figure 4.2 – Model scheme for collective behavior of FtsZ filaments. (A) Well defined head-to-tail direction of FtsZ monomer. (B) FtsZ monomers placed in a fine grained triangular lattice. (C) Low magnification images of FtsZ filaments.

area where attractive energy $-U_a$ is present (open sites). On the other hand, a fine-grained two dimensional triangular lattice restricts the positions of the FtsZ monomers (figure 4.2 B). The distance of 1.5 nm between lattice sites was found to be enough to accommodate the spontaneous curvature and flexibility of the filaments. A finer mesh would significantly increase the computational cost of the simulation without adding relevant information for the comparison with AFM experiments. In contrast, a coarser-grained lattice, although more accessible computationally, is not able to account for the experimental observations. A previously described square-lattice representation that also considered dynamic monomer exchange[84,107] using a cell size comparable to the diameter of the protein monomer, 4.5 nm, and allowing only 4 possible monomer orientations was not enough to accommodate the curvature and flexibility of the filaments observed experimentally.

Three parameters tune the properties of the longitudinal bond between the monomers forming the filaments. The bond energy -U_b can be modulated by the additional energetic cost of deviating contacting monomers from linearity either clockwise (U_+) or anticlockwise (U_-). No penalization for curving on either direction, $U_+ = U_- = 0$, would represent very flexible filaments with no preferential curvature, whereas large symmetric values would produce very stiff and straight filaments. An additional fourth energy parameter in the model describes the lateral attractive interactions $-U_a$, between the monomers[93].

Monte Carlo (MC) simulations run at different protein densities explore the shapes and rearrangements adopted by the filaments.

4.4 Comparison with AFM experiments

4.4.1 Adjusting interaction energies

$-U_b = 12kT$ was estimated from short filament length (see details in[93]), the bending penalization $U_\pm$ and the attractive interaction U_a are selected so that we can reproduce the typical structures observed in the AFM images of FtsZ at relatively low coverage (Fig. 3(a)). The rolled structures observed imply a preferential angle attainable by strongly penalizing one of the bending bonds, i.e. fixing $U_+ = U_b$, which completely cancels the bonding energy in the right-bent (+) configuration. To tune the spontaneous curvature and the high flexibility of isolated filaments a left-bent penaliza-

tion relatively small compare to U_b was used, for instance in the range of $0 \leq U_- \leq kT$.

Figure 4.3 illustrates the selection of lateral attraction U_a. The structures presented in panels (4.3b-f) obtained by MC simulations correspond to U_a values between 0.3 and 1.0 in kT units, while the other model parameters are fixed as $U_+ = U_b = 12kT$ and $U_- = 0.5kT$. The formation of rolls aggregates is a condensation process that requires compensating the entropy loss through an attractive interaction stronger than $U_a = 0.3kT$, as can be appreciated by comparing the AFM image in panel (4.3a) with the lattice model snapshot in panel (4.3b). At the other extreme, $U_a = 1.0kT$ in panel (4.3f) produces bundling of the filaments that is tighter than the one in the structures observed with AFM. The appearance of the experimental images fits well with the three intermediate panels. They show well formed

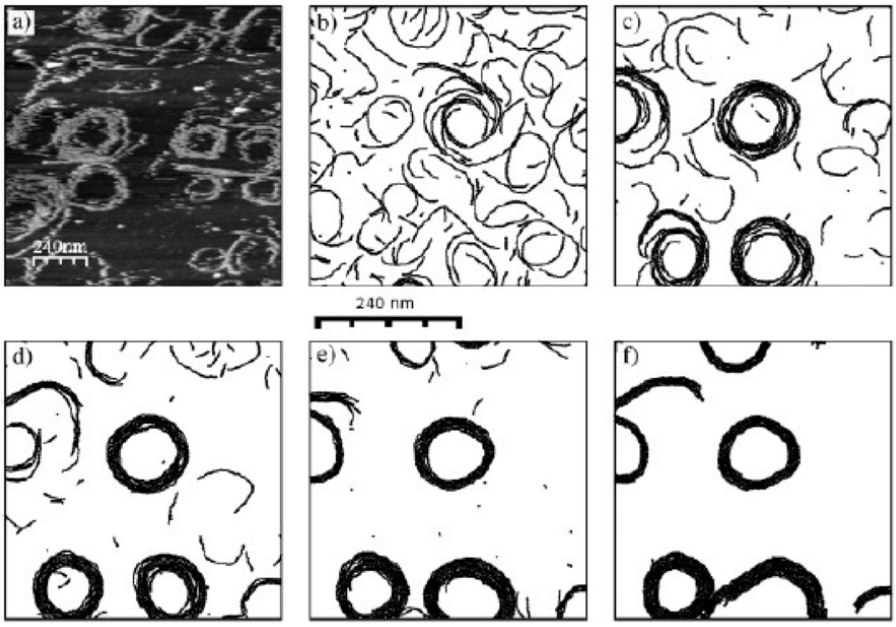

Figure 4.3 – Adjusting lateral interaction energy of FtsZ monomers. Panel (a) shows a typical AFM image of FtsZ protein on mica at medium-low coverage ($\rho \approx$ 1 $pmol/cm^2$). Panels (b-f) are snapshots of MC simulations in our lattice model, with bond energy parameters $U_b = U_+ = 12kT$ and $U_- = 0.5kT$. The lateral attraction parameter is gradually increased: $U_a = 0.3kT$ in panel (b), $0.4kT$ (c), $0.5kT$ (d), $0.6kT$ (e), and $1.0kT$ (f) $U_- = 0.5kT$ and $U_+ = 12kT$. Notice the different scales of the experimental and the MC images.

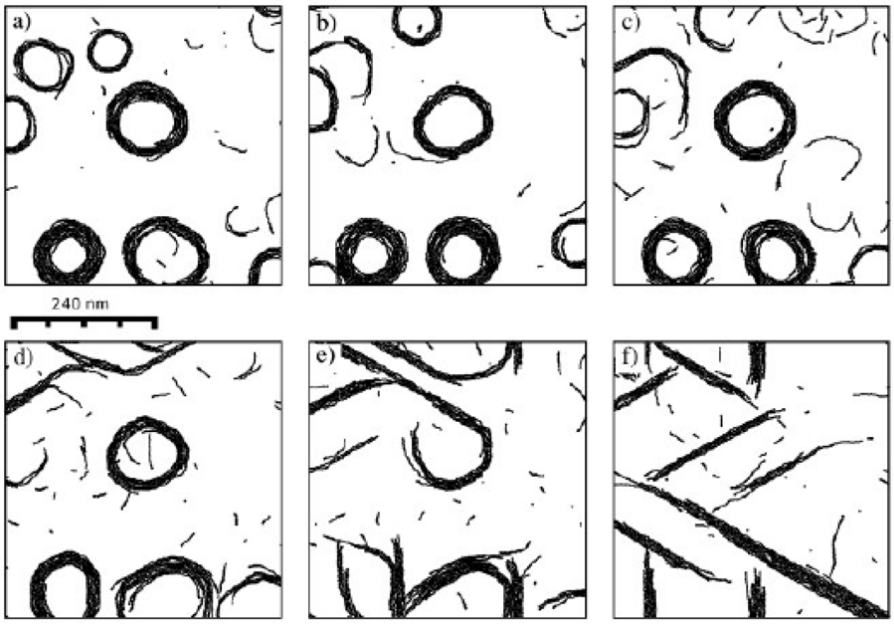

Figure 4.4 – Adjusting curvature and flexibility of FtsZ-FtsZ bonds. Snapshots of MC simulations in our lattice model, as in Fig. 4.3 (d), with parameters $U_b = U_+ = 12kT$, $U_a = 0.5kT$, and different values of the left turn bond penalization: $U_- = 0.125kT$ in panel (a), $U_- = 0.25kT$ (b), $U_- = 0.5kT$ (c), $U_- = 1kT$ (d), and $U_- = 1.5kT$ (e). Panel (f) corresponds to a symmetric choice of the left/right turns, with $U_+ = U_- = 2kT$, and the same values of U_a and U_b.

but looser rolls, in which the filaments may detach and re-attach, and with relatively large mobility of protein between clusters, through the evaporation and re-condensation of short filaments. Therefore, we take $U_a = 0.5kT$ as the most representative value of the observed FtsZ structures.

The fine tuning of the parameter U_- is illustrated in figure 4.4. Values in the range $0 \leq U_- \leq kT$ produce similar structures, although rolls with smaller radii are obtained for lower values. The choice of $U_- = 1.5kT$ presented in panel (4.4 e) produce open rolls and straight bundles.

All together, the set of values that provide a good description of the observed structures are:

- A longitudinal bond energy: $-U_b = 12 \pm 2\ kT \approx 7.2\ kcal/mol$
- A small left-bent penalization: $U_- = 0.5 \pm 0.5\ kT \approx 0.3\ kcal/mol$

- A total right-bent cancellation: $U_+ = U_b$
- A lateral attraction energy: $-U_a = 0.5 \pm 0.1\ kT \approx 0.3\ kcal/mol$

4.4.2 FtsZ filament structures: from high to low coverage

Figure 4.5 shows three snapshots of MC simulations of our lattice model with fixed values of the interaction parameters but different protein coverage (bottom row). The results are again compared with AFM images of FtsZ filaments with similar protein coverage (upper row). The left figures, at relatively high protein coverage, show large regions with local nematic order, co-existing with regions where the spontaneous curvature of the filaments appears, producing interstitial voids with irregular shapes. Further reduction of the protein coverage leads to the central and right figures,

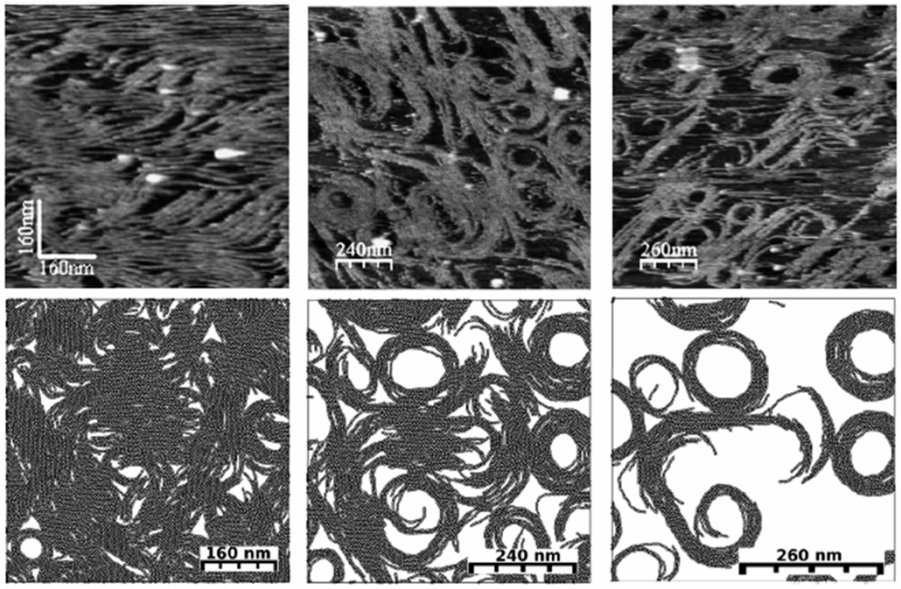

Figure 4.5 – FtsZ filaments structure at different coverages. Examples of the structures formed in the lattice model (bottom), and observed in the AFM images of FtsZ on mica (top) at different coverage of the protein (from left to right: $\rho \approx 6.1,\ 4.3$, and $2.1\ pmol/cm^2$). The interaction parameters in the simulations are $U_b = U_+ = 12kT,\ U_a = 0.5kT$, and $U_- = 0.5kT$, as selected to reproduce the low coverage structures in Fig. 4.3.

with the development of rolled and curved aggregates mixed in a complex percolative network by sharing filaments and forming lateral contacts.

The similarity between the appearance and textures observed in the AFM images and the MC simulations, gives strong support to the hypothesis that our model captures the essence of the interactions between adsorbed FtsZ monomers. The parameter values determined under the diluted conditions (figure 4.3 and 4.4) are still valid for the qualitatively different structures observed at higher protein coverage. Although the balance between the entropy associated with the filament shapes and the energetic factors is strongly shifted by the crowding on the surface, the model still gives a good representation of polymeric bonds, the lateral interactions and spontaneous curvature.

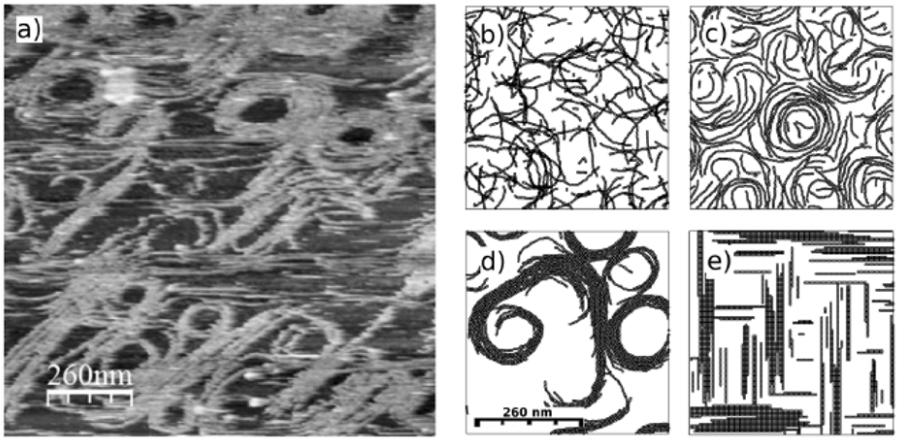

Figure 4.6 – Simulations with incomplete set of interaction energies. The AFM image (a) is compared with equilibrated snapshots of MC simulations of our fine-grained lattice model with incomplete sets of interaction effects. Panel (b) shows filaments formed when the simulation does not include lateral interactions nor excluded volume effects (i.e. isodesmic ideal polymers). Panel (c) comes from a simulation without lateral interactions ($U_a = 0$), to be compared with the snapshot in panel (d) using the complete set of model interactions. Panel (e) corresponds to the coarser square-lattice model presented by Lan et al.[84] at the same protein coverage of a planar surface as in all the other panels.

4.4.3 Minimal set of interaction parameters

We studied if the curvature, longitudinal bonding, and lateral interactions of the filaments considered in our model correspond to a minimal set of parameters needed to reproduce the rich polymorphism observed in the AFM images. Figure 4.6 illustrates the aggregates formed when some of the monomer-monomer interactions considered here are turned off.

MC simulation in which repulsive excluded area and lateral interactions are eliminated shows overlapping filaments and no tendency to form condensed aggregates (panel 4.6b). The inclusion of excluded area effects but not lateral interactions between monomers produces the structures still unable to reproduce the rolled aggregates in AFM image (panel 4.6c), only observed in MC simulations when the lateral attraction between FtsZ filaments is present (panel 4.6d). Panel 4.6e shows a coarser square-lattice simulation unable to account the filaments curvature.

4.5 Discussion

Identifying and estimating the parameters driving polymer formation and aggregation is relevant to understand the function of Z-ring *in vivo*. Although the distribution of FtsZ within the Z-ring is not clear yet, it has been seen that Z-ring is formed by FtsZ polymers comprising around 2000 monomers[31], with a high turnover rate indicating a highly dynamic behavior[103]. Experimental data on the collective behavior of FtsZ filaments obtained by AFM have been used to develop a simple model based on monomer-monomer interactions that accounts for the observed plasticity and rich polymorphism of polymer aggregates at different coverages. Labile longitudinal bond, preferential curvature, flexibility, and lateral attraction were the basic traits represented in by the the model parameters U_b, $U_\pm$ and U_a.

It is clear from AFM measurements that, for fixed biochemical conditions, the collective behavior of FtsZ filaments depends on the protein surface density. The image sequence presented in figure 4.1, showing highly dense layer of filaments leading to bundles and isolated protofilaments as surface coverage decrease, supports this dependency. MC simulations indicate that a much larger longitudinal interaction U_b ($12 \pm 2\ kT$) than lateral attraction U_a ($0.5 \pm 0.1\ kT$) between FtsZ monomers produces two levels of hierarchical organization,i.e. monomers form filaments and filaments form

bundles. FtsZ collective behavior dependence on surface coverage can be understood as a condensation process from a dilute phase (short filaments) to highly packed phase (network of parallel filaments) passing through the formation of isolated or interconnected lateral aggregates at intermediate coverage.

Figure 4.5 shows rolled, curved and straight filament aggregates that might appeared interconnected forming percolative networks. This rich polymorphism indicates that FtsZ filaments are malleable. The labile nature of longitudinal bond is necessary to account for this structural plasticity. A fine balance of the curvature and flexibility ($U_{\pm}$) and the lateral attraction (U_a) determines the shape of isolated aggregates at relatively low coverage. This balance is completely missed in previous coarser lattice models where FtsZ bundles are described as straight and rigid objects.

Models developed from *in vitro* experiments can be used to explore the behavior of FtsZ filaments in conditions difficult to access experimentally. Our model has been used to study computationally the assembly of FtsZ filaments onto cylindrical surfaces mimicking the shape and size *E. coli* membrane[86]. Direct extrapolation of U_b, $U_{\pm}$, and U_a leads to the formation of similar aggregates and interconnected networks on the cylindrical surfaces. On the other hand, a small modulation of model parameters, such as spatially localized weakening of the longitudinal bonds or the existence of an off-plane curvature, are enough to favor the spontaneous formation of rings around the cylinder. The role of MinC has been invoke to destabilize longitudinal bond out of the midcell region. A possible explanation for an off-plane curvature would be loosely linker instead to tight anchoring of FtsZ filaments to the membrane.

4.6 Conclusions

In summary, this chapter presents the collective behavior of FtsZ filaments observed with AFM. The picture that emerges is that filaments are highly dynamic, malleable and they can rearrange depending on the surrounding environment. We observed that curvature and lateral attraction are essential to explain the rich polymorphism. A simple model based on monomer-monomer interactions allows us to estimate quantitatively the polymerization and aggregation of filaments. Comparison of MC simulations with the AFM images constitutes a realistic and experimentally grounded way to account for the basic traits of FtsZ filaments assembly in different conditions.

Part III

FtsZ filaments

on

membrane model system

Chapter 5

FtsZ bundles formed on SLBs in presence of GTP

Abstract

Bacteria divide by forming a contractile ring around their mid-cell region. FtsZ, a cytoskeletal soluble protein structurally related to tubulin, is the main component of this division machinery. It forms filaments that bundle at the inner side of the cytoplasmic membrane. These FtsZ bundles do not attach to bare lipid surfaces. In *Escherichia coli* they remain near the membrane surface by attaching to the membrane protein ZipA and FtsA. In order to study the structure and dynamics of the ZipA-FtsZ bundles formed on a lipid surface, we have oriented a soluble form of ZipA (sZipA), with its transmembrane domain substituted by a histidine tag, on supported lipid membranes. Atomic force microscopy has been used to visualize the polymers formed on top of this biomimetic surface. In the presence of GTP, when sZipA is present, FtsZ polymers re-

structure forming higher order structures. The lipid composition of the underlying membrane affects the aggregation kinetics and the shape of the structures formed. On the negatively charged *E. coli* lipid membranes, filaments condense from initially disperse material to form a network that is more dynamic and flexible than the one formed on phosphatidyl choline bilayers. These FtsZ-ZipA filament bundles are interconnected, retain their capacity to dynamically restructure, to fragment, to anneal and to condense laterally.

5.1 Introduction

Bacteria divide through the action of a complex molecular machine (the divisome) that assembles at midcell. About a dozen proteins organize into a dynamic ring (the division-ring) that generates the contractile force required for cell division. FtsZ, a GTPase tubulin prokaryotic homologue[108], is the first protein to polymerize forming a ring anchored to the inner face of the cytoplasmic membrane through ZipA and FtsA. Subsequently, the rest of the divisome proteins (FtsK, FtsQ, FtsB, FtsL, FtsW, FtsI, FtsN) forming the periplasmic connector and the peptidoglycan factory incorporate into the divisome (reviewed in[4,109]).

The first stage in the assembly of the division ring is the formation of the so called proto-ring by the concerted assembly of FtsZ, FtsA and ZipA[110]. These three proteins assemble some time before the rest of the division proteins are incorporated[111]. Assembly of FtsA and ZipA into the ring is dependent solely on FtsZ[112], while Z-ring formation requires only one of the other two. ZipA binds to the membrane through its N-terminal transmembrane domain[113] while FtsA associates through a conserved short C-terminal amphipathic helix[114]. Both proteins have been found to stabilize the Z-ring, probably by a direct interaction with the carboxy-terminal tail of FtsZ[115,116]. This suggests that one role of these proteins is to stabilize and anchor the FtsZ polymers to the membrane[110,117].

The FtsZ ring is a membrane bound dynamic structure. *In vivo* experiments in *Escherichia coli*[103], have shown that in the functional divisome complex, both proteins, FtsZ and ZipA, can exchange in and out of the ring within seconds. It is not known yet how this protein exchange takes place and how it affects the stability of the ring. *E. coli* ZipA is a 36.4 kDa membrane-anchored protein with a short N-terminal transmembrane domain (aa 1-25) followed by a basic region ($\sim$ 23 aa), an acidic region ($\sim$ 17 aa), and a long proline rich region, the P/Q domain (residues 86-188), that stands between the membrane and the C-terminal globular domain binding FtsZ[113]. Evidence obtained by electron microscopy showed that this P/Q domain is flexible and may stretch over a length from 8 to 20 nm[117]. Different *in vivo* and *in vitro* assays have indicated that the interaction between ZipA and FtsZ is mediated by the C-terminal region of the proteins[17,118] and that the C-terminal domain of ZipA (residues 176-328) is required and sufficient to bind FtsZ. X-ray crystallography[116] and NMR[119] have both provided high resolution information on the interaction region, but little is known about the role played by the rest of the ZipA

domains. It has been speculated[120] that the flexible tether constituted by the P/Q domain might be important for defining the FtsZ functional orientation on the membrane surface.

This flexible tether stands in the proximity of the membrane, therefore the surface characteristics determined by the membrane phospholipid head groups could be relevant for defining the functional configuration. Recent experiments have shown that the distribution of phospholipids in bacterial membranes is heterogeneous and that this is relevant in cell division[121]. It is not known however how the charge and lateral organization of the main glycerophospholipids found in bacteria (phosphatidylethanolamine, phosphatidylglycerol, and cardiolipin)[122] affect the protein interactions at the interface.

In this work we perform a high resolution structural and dynamic characterization of the FtsZ polymers formed in the presence of sZipA anchored on lipid membrane surfaces using atomic force microscopy. To mimic the initial stages of the divisome formation, we use a simplified reconstituted system of controlled composition using only three elements: FtsZ, ZipA and the lipid bilayer. We visualize at single molecule level FtsZ self-assembly occurring on the surface of a supported lipid bilayer containing sZipA with a histidine-tag replacing its membrane region and oriented on the surface by including nickel chelating lipids in the bilayer.

We have examined the ability of FtsZ bound to the artificially anchored sZipA to assemble dynamically and form higher order structures. In addition we have investigated the effect of different lipids, i.e. egg phosphatidyl choline or *E. coli* lipids on the behavior of the assembled molecules.

5.2 Materials and methods

Reagents

GTP was acquired from Sigma. Other analytical grade chemicals were from Merck or Sigma. *E. coli* lipid polar extract (EcPL) and 1,2- dioleoyl-sn-glycero-3-[(N-(5-amino-1carboxypentyl)iminodiaceticacid) succinyl] (DGS-NTA (Ni)), L-α-phosphatidylcholine from chicken egg (EPC) and 1,2-dioleoyl-sn-glycero-3-phosphocholine (DOPC) were purchased from Avanti polar lipids.

Protein purification

E. coli FtsZ was purified by the calcium-induced precipitation method as described in[10]. The soluble mutant of ZipA was constructed by eliminating the hydrophobic N-terminal domain (aa 1-25) of the full length protein, as described elsewhere[123]. sZipA fractions were pooled and stored at -80°C. The purity of sZipA was > 95% according to SDS-PAGE.

Liposomes preparation

Liposomes were prepared from mixtures of lipids (EcPL, EPC or DOPC) and DGS-NTA (Avanti Polar Lipids, Alabaster), in a molar ratio of 10:1. Lipids were dissolved in 1:1 chloroform:methanol solution, mixed in the desired amount, dried under a stream of nitrogen and resuspended at 4 mg/ml lipid concentration in MiliQ water. The resulting multilamellar vesicles were extruded through a polycarbonate membrane with 200 nm nominal pore diameter (Avanti Mini extruder) resulting in large unilamellar vesicles (LUVs).

Planar lipid bilayer formation

40 μl of 0.1 g/l LUV solution in Tris-HCl 10 mM, 100 mM NaCl, and 2 mM $CaCl_2$ (pH 7.5) were incubated on a freshly cleaved mica surface for 1 h resulting in the formation of a Supported Lipid Bilayer as described in[124]. The solution containing the non-fused lipid vesicles was removed and replaced by working buffer (Tris 50 mM, KCl 0.5 M, $MgCl_2$ 5 mM, pH 7.5). Incomplete lipid bilayers were formed by reducing to a few minutes the time the mica surface is exposed to solution containing the lipid vesicles.

Quartz crystal microbalance (QCM)

A quartz crystal microbalance, capable of measuring frequency and dissipation changes (KSV QCM-Z500) was used to quantify the amount of protein adsorbed to the membrane containing linker lipid. A lipid bilayer containing 9:1 molar ratio DOPC:DGS-NTA was formed on a SiO_2 quartz crystal sensor (qsense QSX 303) upon exposure to a solution containing lipid vesicles at 0.1 g/l. After bilayer formation, the liposome containing solution in the chamber was replaced by a solution containing 3 μM sZipA in working

buffer (Tris 50 mM, KCl 0.5 M, $MgCl_2$ 5 mM, pH 7.5). After replacing the ZipA solution by buffer, the binding of FtsZ was registered after injection of FtsZ in the same buffer to reach a 10 μM concentration.

Atomic force microscopy

Atomic force microscopy (AFM) images were taken with a microscope from Nanotec Electrónica (Madrid, Spain) operated in the jump mode[94]. The scanning piezo was calibrated using silicon calibrating-grating (NT-MDT Moscow, Russia). Silicon nitride tips (Olympus) with a force constant of 0.05 N/m were used. To observe ZipA-FtsZ bundles on mica, FtsZ filaments were polymerized in solution in the presence of sZipA and adsorbed on mica immersed in buffer containing 1 mM GTP. To observe the ZipA-FtsZ bundles on the lipid bilayers, sZipA (3 μM) and FtsZ (12.5 μM) were incubated for an hour in Tris 50 mM, 0.5 M KCl, and 5 mM $MgCl_2$, pH 7.5 buffer over the lipid bilayer previously fused on the mica surface. Excess protein was removed from solution and GTP was added before imaging. This protocol resulted in reproducible attachment of the ZipA-FtsZ complex to the lipid bilayer leaving the FtsZ protein responsive to the presence of GTP.

Transmission electron microscopy

A drop of the solution of FtsZ polymers (protein concentration 0.5 g/l (12.5 μM)), formed in the absence or in the presence of sZipA (0.25 g/l (7 μM)) in Tris 50 mM, 0.5 M KCl, 5 mM $MgCl_2$, and 1 mM GTP, pH 7.5 was placed in the microscope grid after one minute incubation with GTP to be visualized by electron microscopy after negative staining with 2% uranyl acetate, using a JEOL-1200 electron microscope.

5.3 Results

5.3.1 sZipA-FtsZ bundles on mica

Fig. 5.1 shows a schematic of the different components used in the sample preparations and a reasonable prediction on how they may assemble on the

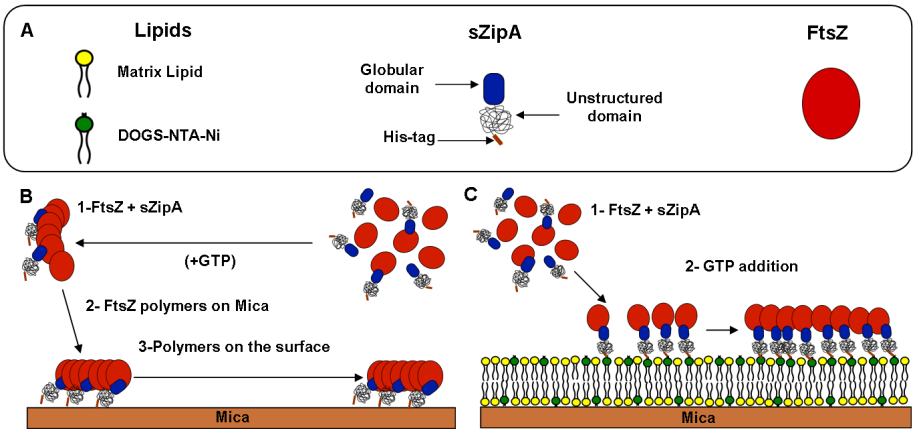

Figure 5.1 – Membrane model system cartoon. Schematic prediction of the reconstituted system. Panel (A) describes the elements used. Panel (B) illustrates the procedure followed to form the sZipAFtsZ bundles on mica and panel (C) the procedure followed to form the bundles on lipid surfaces.

mica surface before imaging with the AFM. sZipA incubated with FtsZ in solution in the presence of GTP forms individual filaments similar to the ones observed in the absence of sZipA, as shown in the TEM images (Fig. 5.2A and B). The behavior observed under our experimental conditions (Tris 50 mM, 0.5 M KCl, 5 mM $MgCl_2$, pH 7.5) (Fig. 5.2B) contrasts with previous observations in which the presence of ZipA induced the formation of FtsZ bundles[17]. The fact that those experiments were carried out at pH 5.8, conditions under which GTPase activity is expected to be at least 5 fold lower[9], could explain this difference. However, when these sZipA-FtsZ filaments are adsorbed on mica in the presence of GTP, they undergo a substantial rearrangement over the surface (Fig. 5.2C). They are about 5 nm in height above the mica, indicating that they remain only one filament thick, but they form longer and wider structures with widths varying from 30 to 60 nm, compatible with a parallel arrangement of 6 to 15 FtsZ protofilaments (see below). A zoom of a smaller area (Fig. 5.2D) illustrates that the reorganization over the surface takes place by fragmentation, reannealing, and lateral condensation, as was previously described for individual FtsZ filaments[12]. These straight and thick filament aggregates are not found in the absence of sZipA.

In this situation in which sZipA is free to move and not attached to the surface, polymers on the surface reorganize if GTP is available in the solu-

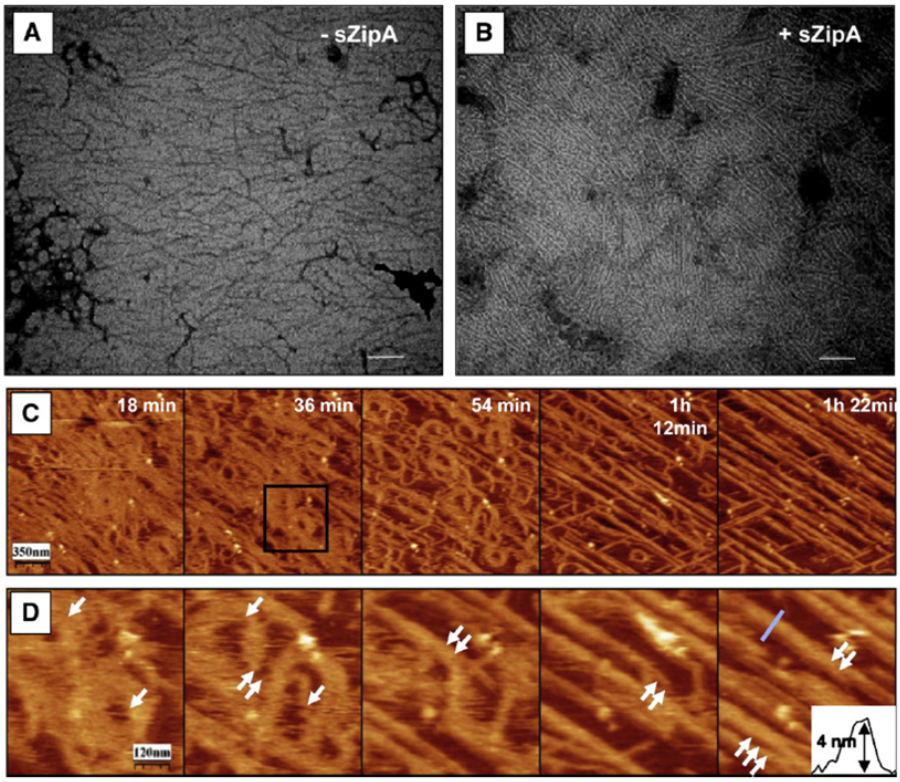

Figure 5.2 – FtsZ-ZipA bundles on mica. TEM images of FtsZ filaments formed in the absence (A) (Scale bar is 100 nm) and presence (B) of sZipA. (C) Reorganization of FtsZ filaments by sZipA on mica. Snapshots of FtsZ filaments polymerized in solution in the presence of sZipA and adsorbed on mica immersed in buffer containing 1 mM GTP over a period of 1 h and 22 min. Panel (D), enlarged region shown in C (subsequent images about 10 min apart), illustrates the rearrangement that precedes the formation of the straight bundles (opening, reannealing and lateral aggregation events are marked with single, double and triple arrows respectively). The inset shows the height of the filaments.

tion, indicating that sZipA bound to FtsZ filaments does not restrict their dynamic behavior, similarly to the one previously described for filaments assembled in solution[125] and on mica[12] (see movie S3 in Supplementary Material). When GTP is not added to the imaging buffer, the initially formed filaments disappeared without further reorganization. We were unable to identify the position of sZipA within the bundles to obtain direct information about the way it crosslinks the filaments. Indirect evidence of

its location comes from measuring the height of the bundles (see inset in Fig. 5.2D), corresponding to the height of the FtsZ filaments, which suggests that sZipA is not sitting between the filaments and the mica but is most likely intercalating between the filaments and modulating lateral contacts to induce the formation of thicker bundles. We can conclude from the observed behavior on mica that, as long as GTP is present, the sZipA-FtsZ bundles remain active to restructure on a surface.

5.3.2 sZipA-FtsZ on lipid bilayers

We first checked the formation of the lipid-protein modified surface using a QCM. The formation of a lipid bilayer on a solid surface and the subsequent sZipA and FtsZ binding to the lipids was monitored by following the frequency changes of the sensor after the different incubations (Fig. 5.3). The -25 Hz frequency change registered when the surface is exposed to a 0.1 mg/ml liposome solution (9:1 molar ratio of DOPC:DGS-NTA), confirms the formation of a full bilayer [73]. The additional frequency change observed after exposure of this lipid surface to a $3\mu M$ sZipA solution indicates the formation of a dense monolayer of protein. The estimated amount, ob-

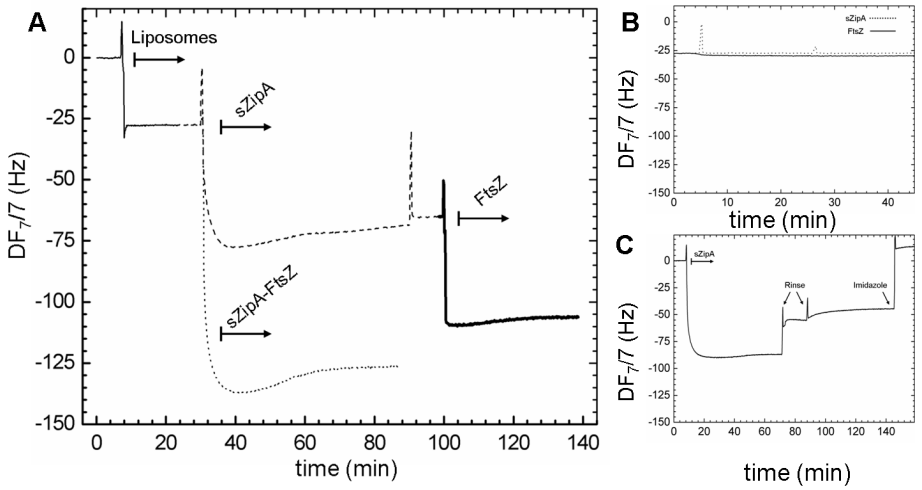

Figure 5.3 – QCM. (A) Frequency change upon addition of liposomes (thin line), sZipA (dashed line), FtsZ (bold line) and sZipAFtsZ complex (dotted line). (B) Non specific binding of sZipA and FtsZ on a DOPC bilayer without NTA. (C) Elution of sZipA bound to the DOPC-NTA bilayer after addition of imidazole 500 mM.

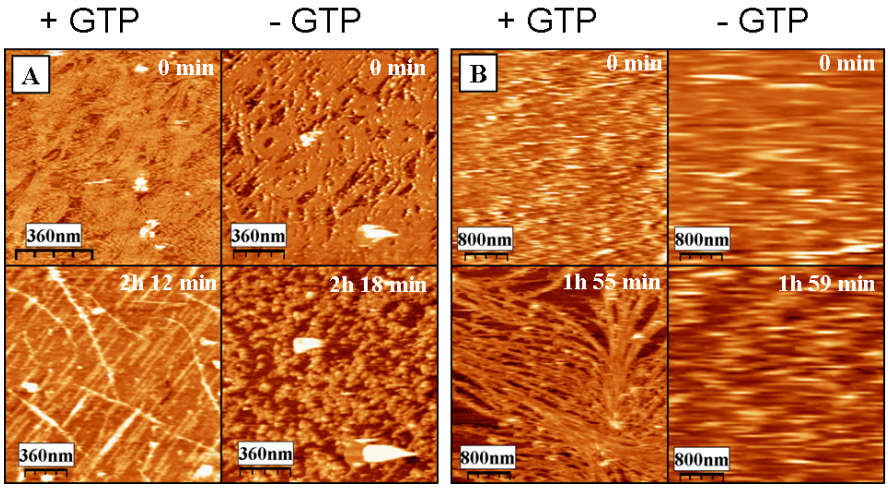

Figure 5.4 – Evolution of the filaments formed on lipid-sZipA. The upper panel shows the initial structure of FtsZ anchored to a lipid surface through sZipA in EPC (A) and EcPL (B) after addition of 1 mM GTP. The lower panel shows the final structures formed on the surface after approximately 2 h in the presence and absence of GTP in the imaging buffer.

tained from converting the frequency change into mass using the Sauerbrey relation[57], was 710 ng/cm^2 (∼21.2 pmol/cm^2). The average area occupied by each ZipA molecule is then approximately 8 nm^2, which corresponds to a dense protein monolayer. Higher amounts of sZipA in solution gave the same result, indicating that this concentration, comparable to the one used in the preparation of the samples characterized with AFM, was enough to saturate the lipid surface. To test the FtsZ binding capacity of this sZipA monolayer, a 10μM FtsZ solution, in the absence of GTP, was added. FtsZ binding to the ZipA was confirmed by the observed decrease in the resonance frequency (Fig. 5.3A). No sZipA or FtsZ bound to the bilayer in the absence of nickel chelating neither lipids nor FtsZ (Fig. 5.3B) in the absence of sZipA. The addition of both sZipA and FtsZ to the solution, a protocol that gave reproducible results and FtsZ polymerization on the lipid surface after GTP addition, gave a comparable mass increment as that obtained after sequential addition of the proteins. The sZipA could be detached from the membrane upon addition of 200 mM imidazole[126] (Fig. 5.3C) indicating that the interaction of the protein with the membrane is governed by the N-terminal His-tag binding to the NTA lipid.

After confirming with the QCM that sZipA bound to the membrane

containing NTA lipids through the histidine tag and that this oriented sZipA was competent to bind FtsZ, we proceeded to image the modified lipid surfaces with the atomic force microscope. In order to explore the effect of the type of lipid environment on the formation of sZipA-FtsZ bundles, lipid bilayers of two different compositions were used, one containing Egg phosphatidyl choline (EPC), a zwiterionic lipid not found in *E. coli* membranes, and another one containing only polar *E. coli* lipids, rich in negatively charged phospholipids. Both were prepared at a 9:1 molar ratio of phospholipid: DGS-NTA in order to contain the same amount of linker lipid. Samples were prepared as depicted in Fig. 5.1C. On egg phosphatidylcholine (EPC) lipid bilayers, filaments formed immediately upon addition of GTP (Fig. 5.4A, t=0 min). If GTP is maintained in the imaging buffer, these structures evolve into straight long arrangements of parallel filaments.

Intermediate stages show the formation of transient wiggly condensates aligned perpendicular to the filaments' longitudinal axis (see movie S4 in Supplementary Material documenting events at approximately 4 minute intervals). In the absence of GTP during imaging (movie S5), the filaments initially formed in solution in the presence of GTP depolymerize on the surface without undergoing any further rearrangement.

The same behavior observed on EPC bilayers was observed on DOPC lipid membranes, a phospholipid sharing the same headgroup as the EPC but differing in the fatty acid composition (results not shown). This suggests that the relevant parameter affecting the behavior of the polymers is the nature of the lipid head group and not the nature of the fatty acids.

sZipA-FtsZ polymers formed on the bilayer prepared with *E. coli* polar lipid extract produce a substantially different image. In this case no FtsZ filaments are initially observed after GTP addition (Fig. 5.4B), in contrast to what was observed on the EPC bilayer. The fuzziness of the images indicates that an amorphous protein layer covers the surface, even when GTP is present in the solution. It takes several minutes to condense and develop into well defined filamentous structures (see movie S6a in Supplementary Material documenting the process at approximately 4 minute intervals). GTP in the solution is required for the transformation of the unstructured surface into well defined polymers.

The condensation into curved flexible thicker structures occurs without prior formation of individual filaments as the ones formed on bare mica or on EPC. These aggregates are also extensively branched, in contrast to the straight structures observed on EPC. The assemblies display an active dynamic behavior that retains the same features previously described

for individual filaments: fragmentation (Fig. 5.5A), annealing, crosslinking (Fig. 5.5B), as well as lateral condensation (Fig. 5.5C). It is interesting to note that these short range local transient structural modifications do not destabilize the micrometer range features of the network (Supplementary Material, movie S6b).

The proximity of the FtsZ polymers to the membrane surface and their plasticity are affected by the lipid composition. Fig. 5.6 shows the height profiles of the polymers formed on mica, EPC and on EcPL lipid surfaces. The polymer bundles formed on mica and on EPC lipids stand away from the surface a short distance corresponding to one protein monolayer (Fig. 5.6

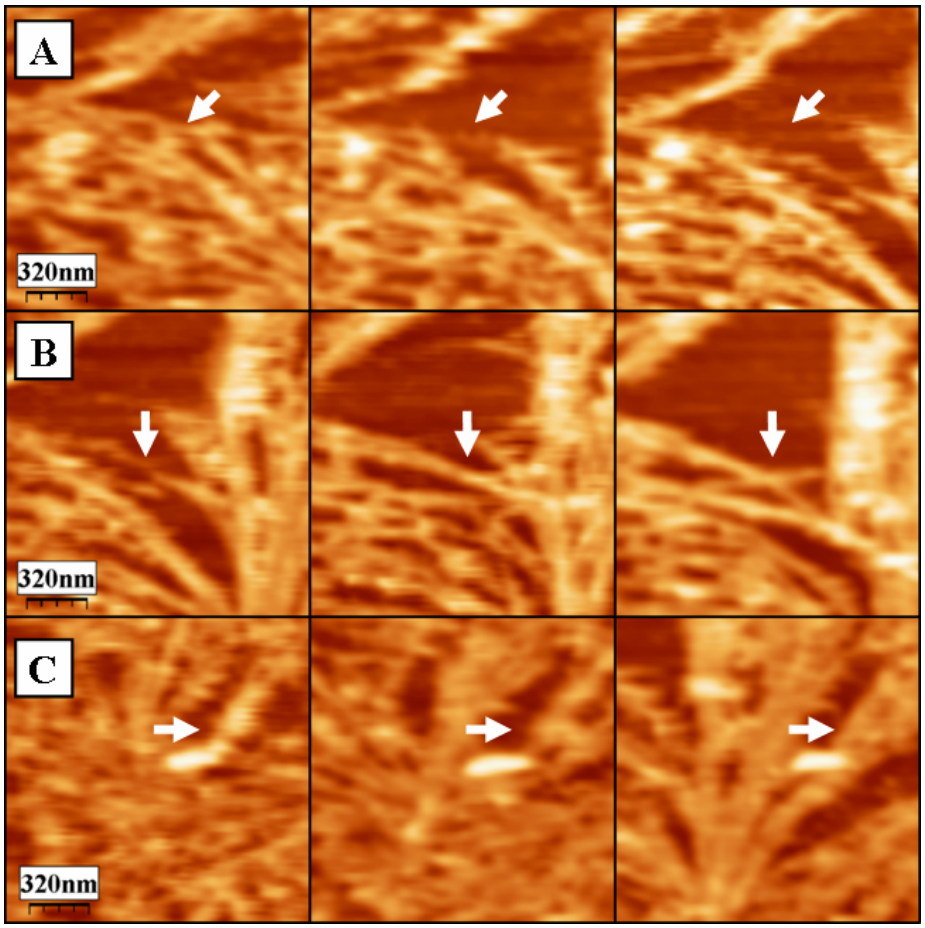

Figure 5.5 – Dynamics of FtsZ network on EcPL bilayer. Network shown in Fig. 4B was observed over the following 30 min. Upper row shows rupture, central sequence shows branching and annealing and lower sequence lateral condensation.

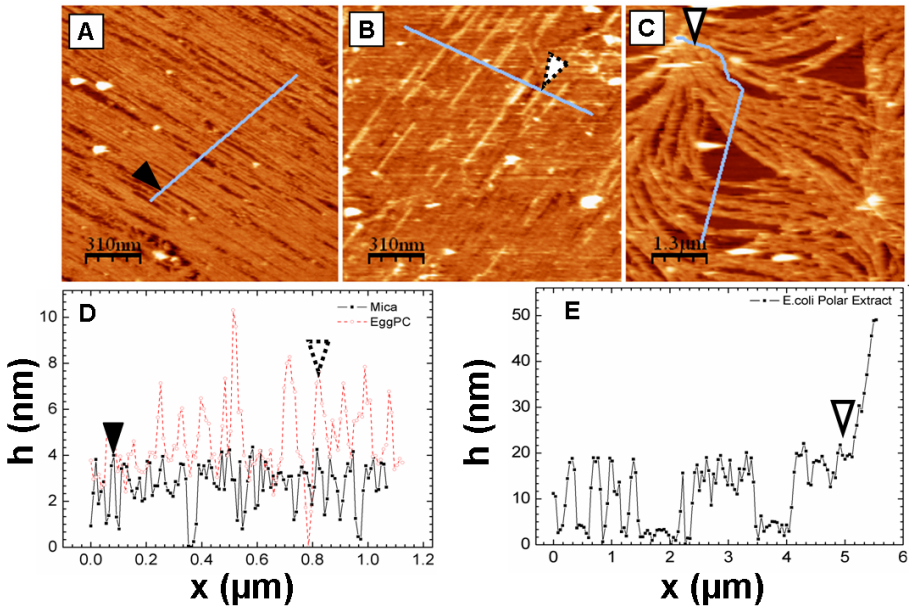

Figure 5.6 – Height profile of FtsZ polymers on different surfaces. sZipA-FtsZ bundles on mica (A), on EPC bilayer (B), and on EcPL (C) bilayer. D and E show the height profiles of filament bundles on the different surfaces.

A, B, D). In contrast, bundles formed on *E. coli* lipids stand further away from the surface and curve, both on and off plane, forming a highly interconnected network (Fig. 5.6 C, E). The bundle widths range from 100 to 150 nm and their average height over the surface is around 18 nm. The structures can also curve away from the surface, as is shown in Fig. 5.6E.

Straight and stiff bundles observed on EPC bilayers are similar to the ones observed on mica, whereas the sZipA-FtsZ bundles on EcPL bilayers are curved. The unstructured ZipA domain, including the charged N-terminal part [7], is expected to have nearly 8 nm end-to-end distance when relaxed, as measured in solution by FRET[127]. Considering that the size of the FtsZ monomer is approximately 4 nm in diameter[128] and the size of the carboxi globular domain of the ZipA[116] is roughly 3 nm, the height measured on EcPL can be interpreted as indicating that the sZipA non-structured domain is located between the FtsZ filaments and the membrane, whereas on the EPC lipid surface, it is probably lying parallel to the membrane surface intercalated within the longitudinally aligned FtsZ filaments, which is similar to what is observed on mica. Fig. 5.7 depicts a schematic of this interpretation. Figs. S1 and S2 in Supplementary Ma-

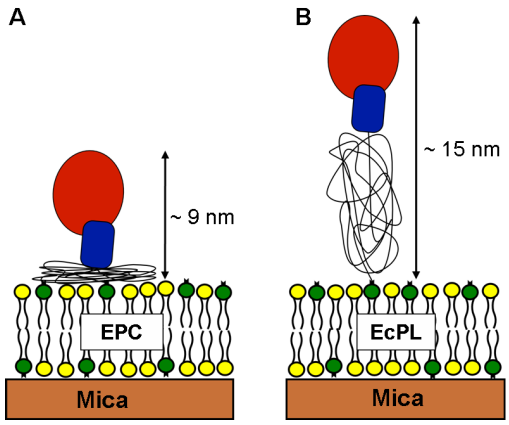

Figure 5.7 – Illustration of the lipid effect on the sZipA nonstructured domain. (A) EPC bilayer with no net charge does not repel the highly charged non-structured domain of sZipA, which then lies closer to the lipid surface. (B) The negatively charged EcPL bilayer could repel the sZipA charged region and expanding it, causing the increased height of the protein complexes.

terial show that the height difference of the protein complexes above the two lipid membranes is present before GTP addition. This suggests that the effect is mainly due to the sZipA interaction with the lipid surface and not to FtsZ polymerization state. A different degree of stretching of the non-structured ZipA P/Q domain induced by the lipid head charges could account for this effect.

5.4 Discussion

The goal of our work was to study the effect of ZipA on FtsZ polymerization on lipid membranes. In order to do this, we tethered the His-tagged sZipA to nickel chelating lipids incorporated to the membrane [129]. This experimental setup shares two important features with the situation found *in vivo*: sZipA is oriented on the membrane with the carboxi end exposed to the solution, and the protein is free to diffuse laterally on the fluid underlying lipid bilayer.

We found, unexpectedly, that the surface reorganization process and the shape of the filament aggregates were very sensitive to the type of lipid present in the bilayer. EPC and EcPL lipids greatly differ in their surface

charge. Whereas PC is a zwitterionic lipid, the phospholipid headgroups of the *E. coli* lipid extract include 30% of the negatively charged lipids cardiolipin and phosphatidylglycerol[122]. The non-structured domain of ZipA is highly charged. The 20 residues (aa 28-48) following the hystidine tag have a net charge of +8 followed by an acidic region (aa 49-65) with negative charge (−11) followed by another basic region of net positive charge of +4 (aa 66-75). The positive region closest to the membrane is likely to induce lipid segregation to recruit negatively charged lipid heads, which could then repel the neighboring negatively charged region causing the observed extension away from the membrane. Charged lipid segregation in fluid membranes has been proposed to play an important role in the subtle interplay between the various entropic and energetic contributions that determine the binding free energy of flexible charged polymers to mixed fluid membranes[130,131].

The surface distribution of membrane lipids in the bacterial membrane is known to change during cell division and CL is enriched in the septal region[121]. This lipid segregation could play an important role in modulating the flexible and charged region of ZipA to optimize FtsZ orientation and function on the surface[120]. FtsZ, having an isoelectric point of 4.9[132], could be charged under our experimental conditions. However the QCM results clearly indicate that at the pH and salt concentrations used in the experiments, in the absence of sZipA, there is no significant electrostatic interaction between FtsZ and the membrane.

There are two intriguing differences in the behavior of the polymers dependent on the underlying lipid composition: the shape of the final structures formed and their formation kinetics. On EPC, as well as on mica, the filament bundles evolve into predominantly straight structures whereas on EcPL lipids they adopt curved shapes. They also form immediately after GTP additions, indicating that any longitudinal interactions needed to form filaments occur immediately. On EcPL, however, this polymerization step takes several minutes. Both effects could be a consequence of the distance away from the surface at which ZipA holds the FtsZ, as observed from the height measurements. Their orientation could be less restricted, increasing the time required for their alignment to form filaments, but allowing enough flexibility to form curved aggregates.

Both longitudinal and lateral interactions between FtsZ monomers[86,133] appear to participate in the formation of the bundles observed on the surfaces. GTP is required to maintain the longitudinal monomer-monomer association, and the lateral interactions modulated by sZipA induce the

aggregation of individual filament into thicker bundles. Structures were observed to evolve with time on the different surfaces, indicating that diffusion on the plane of the membrane could contribute to tune the formation of the polymers on lipid surfaces. Our results provide strong evidence that ZipA acts not merely as a filament anchor but that its presence modulates the shape and aggregation state of the FtsZ filaments on the surface. This is also the first experimental evidence that ZipA acts as a flexible tether between the membrane and the C-terminal domain of FtsZ conferring a large plasticity to the membrane bound FtsZ polymers, as had been previously suggested[86,117]. Additionally, we observe that the presence of charged lipids on the underlying membrane is essential to increase the flexibility of the ZipA nonstructured domain.

Recently, theoretical calculations have proposed different ring formation and force generation mechanisms in bacteria[82,83,85–91,93,97,133–135]. They are based on different assumptions about FtsZ monomer interactions and filament attachment to the membrane. The results presented here address some of these assumptions. The increased flexibility, dynamism and interconnectivity of FtsZ bundles formed on EcPL bilayers, as well as the decreased on plane curvature and increased off plane curvature relative to the ones found on mica, are all compatible with recent models that pointed out that modulating these two parameters, on plane and off plane curvature, could favor the formation of rings on a cylindrical surface[86]. Our observations are also compatible with assumptions made by theoretical models based on the formation of cross-linked polymeric structures of FtsZ with healing ends after monomer removal[91], on condensation through the effect of lateral interactions[86,97,133] or on cross-linking and bundling between filaments to generate forces[89].

5.5 Conclusions

Oriented ZipA on lipid surfaces promoted the assembly of FtsZ polymers into higher order lateral condensed aggregates of individual filaments. Filaments on EPC bilayers formed immediately after GTP addition and aggregated into straight bundles, whereas on *E. coli* lipids, the polymers formed after a certain lag time, stayed further away from the membrane and were curved and dynamic. The presence of ZipA therefore affects differently the crosslinking, bundling, orientation, flexibility and curvature (on and off plane) of FtsZ polymers depending on the type of lipids present on the un-

derlying membrane. Supplementary materials related to this article can be found online at doi:10.1016/j.bbamem.2011.12.012.

5.6 Supplementary Materials

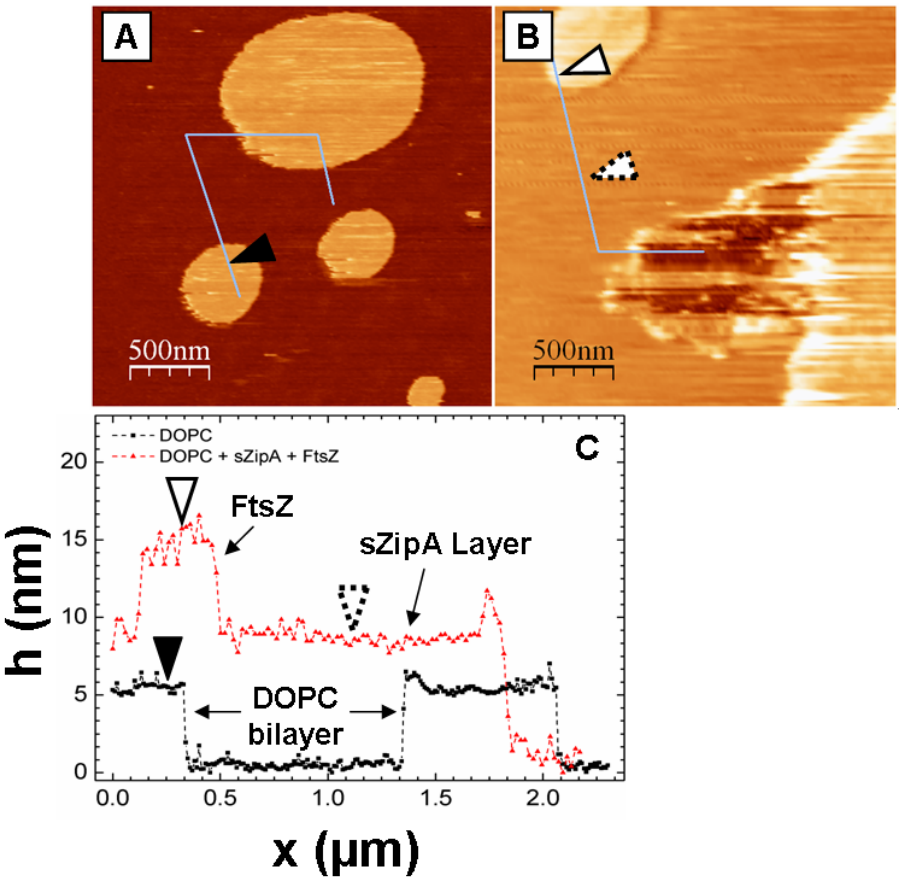

Figure 5.8 – Height profile of FtsZ before adding GTP on EPC. EPC bilayer patches (A), sZipA and FtsZ on EPC bilayer (B). (C) show the height profiles.

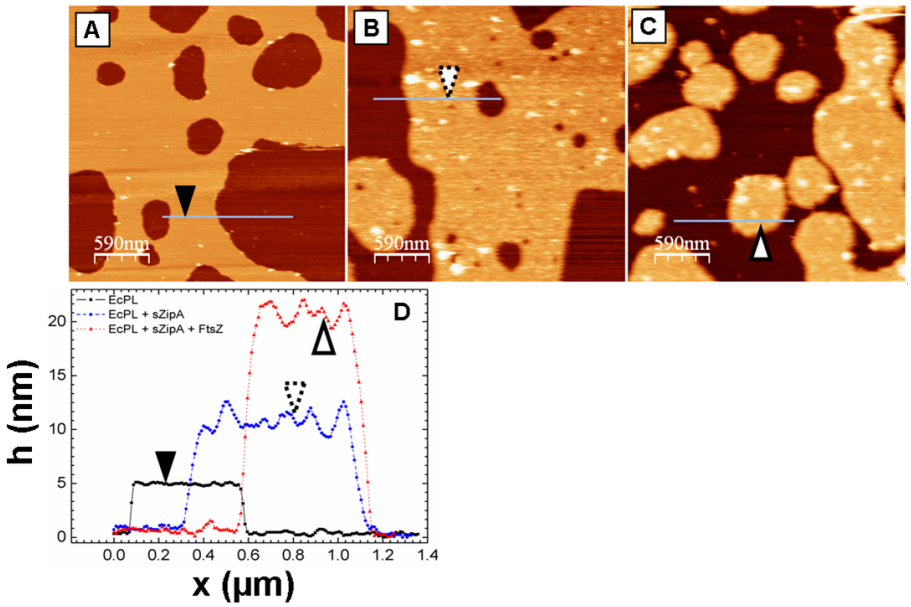

Figure 5.9 – Height profile of FtsZ before adding GTP on EcPL. EcPL incomplete bilayer (A), sZipA on EcPL bilayer (B) and sZipA-FtsZ complex on EcPL bilayer (C). (D) shows the height profiles.

5.6.1 Videos

The videos can be found in the web page:

http://www.sciencedirect.com/science/article/pii/S0005273611004391

FtsZ-ZipA bundles on mica

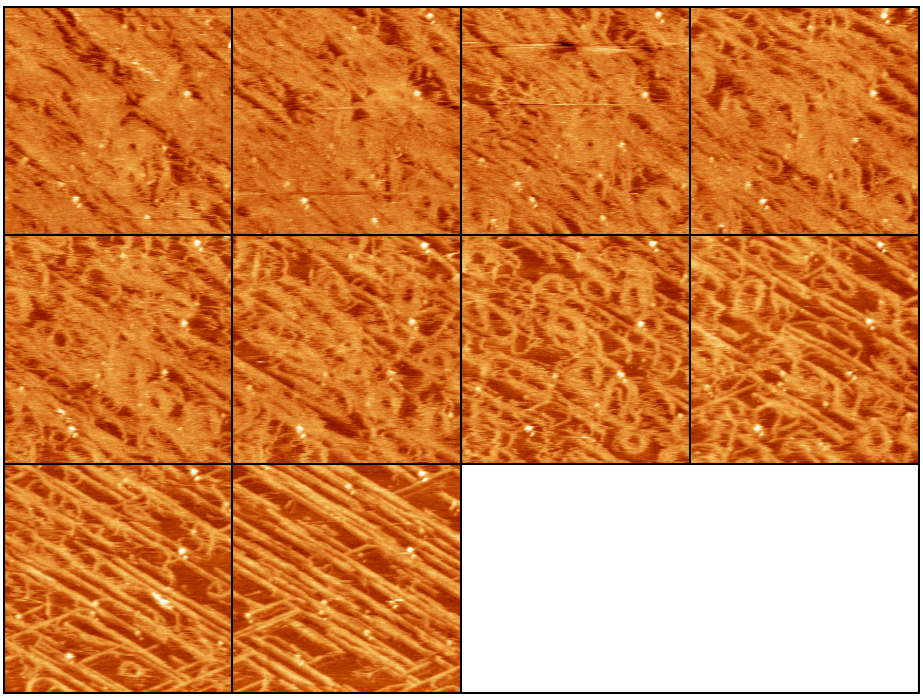

Figure 5.10 – Video S3 FtsZ-ZipA bundles on mica in buffer at pH 7.5 with GTP. Image size is 1.7 x 1.7 μm and time lapse between frames is $\sim$ 9 min

FtsZ-ZipA bundles on EPC lipid bilayer

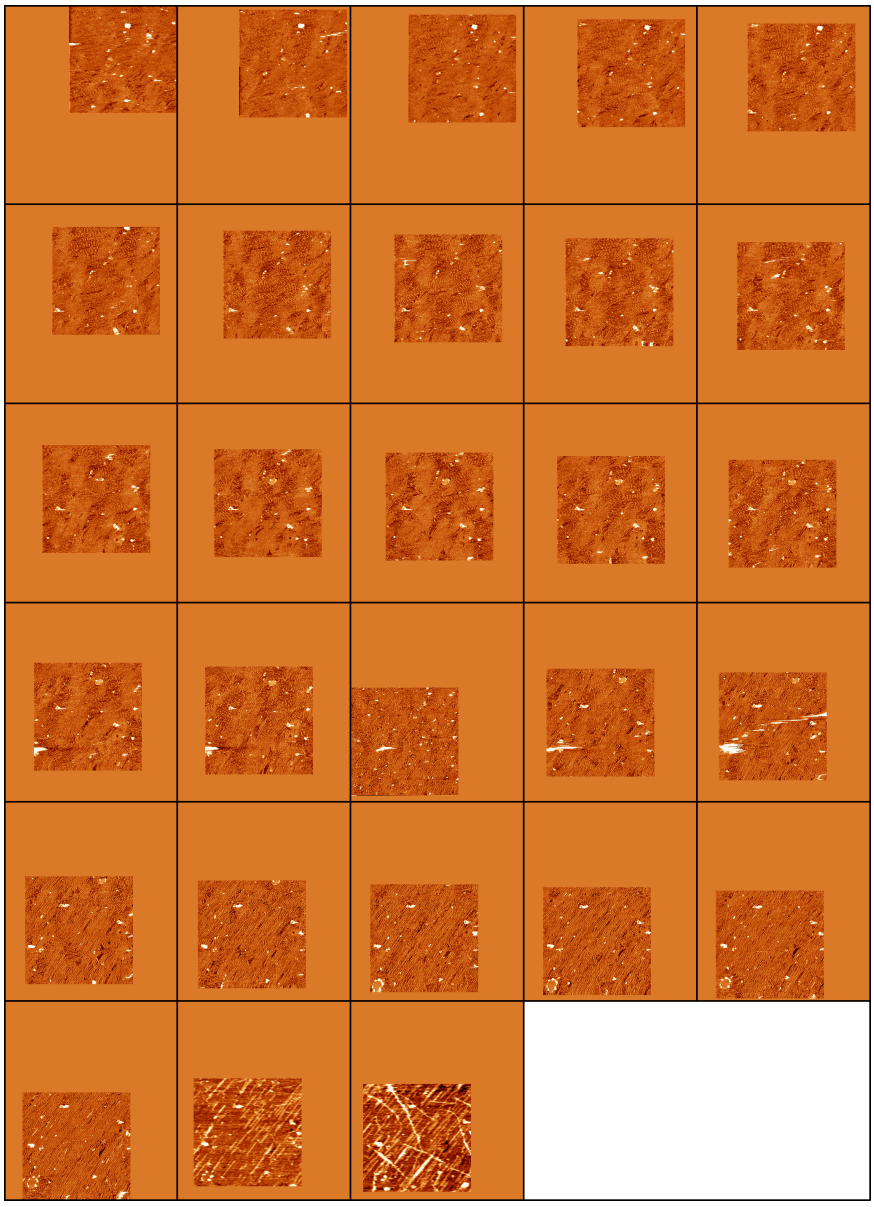

Figure 5.11 – Video S4 FtsZ-ZipA bundles on EPC bilayer in buffer at pH 7.5 with GTP. Image size is 1.8 x 1.8 μm and time lapse between frames is ∼4 min

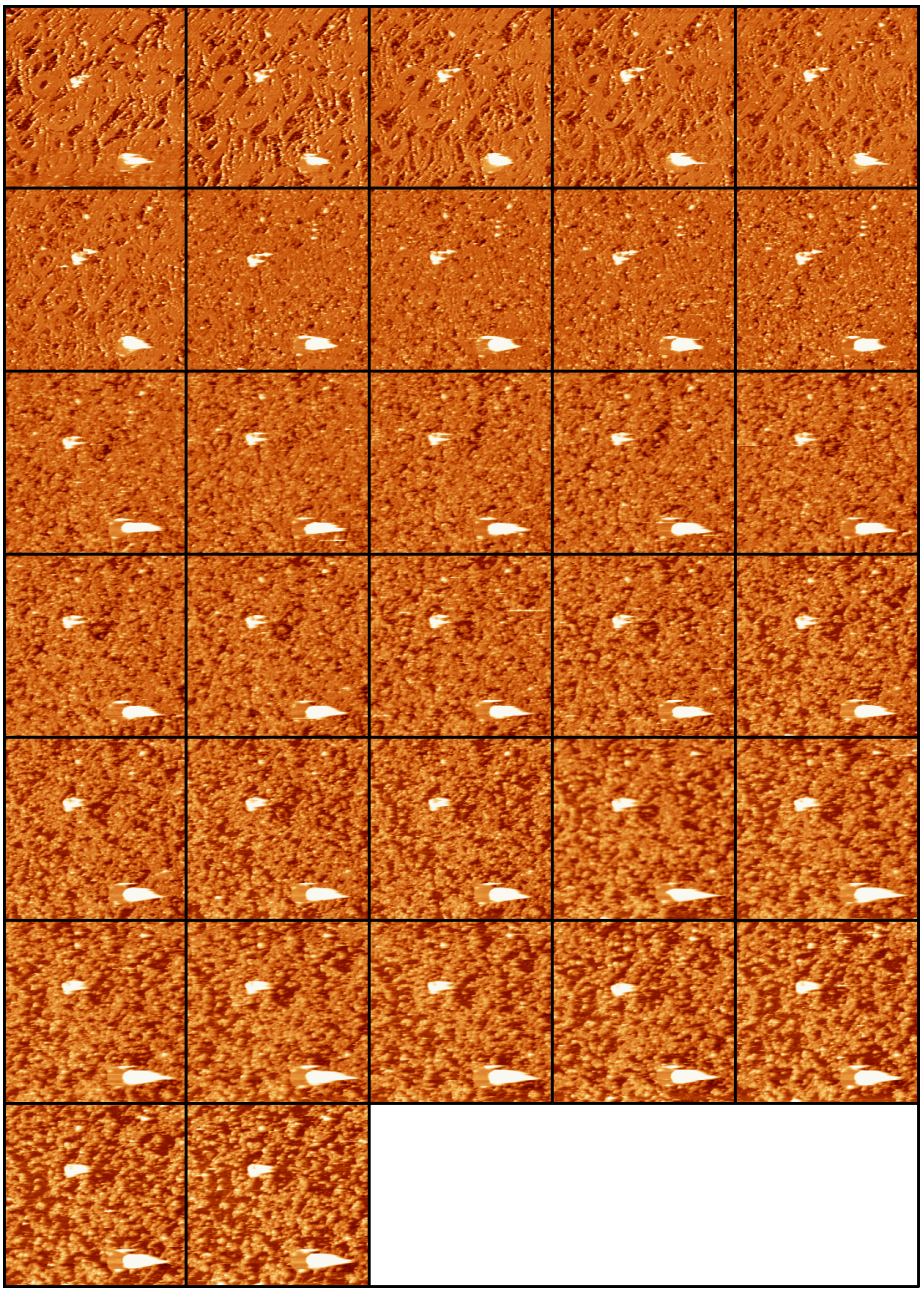

Figure 5.12 – Video S5 FtsZ-ZipA bundles on EPC bilayer in buffer at pH 7.5 in absence of GTP. Image size is 1.5 x 1.5 μm and time lapse between frames is ∼3 min 30 s

FtsZ-ZipA bundles on EcPL lipid bilayer

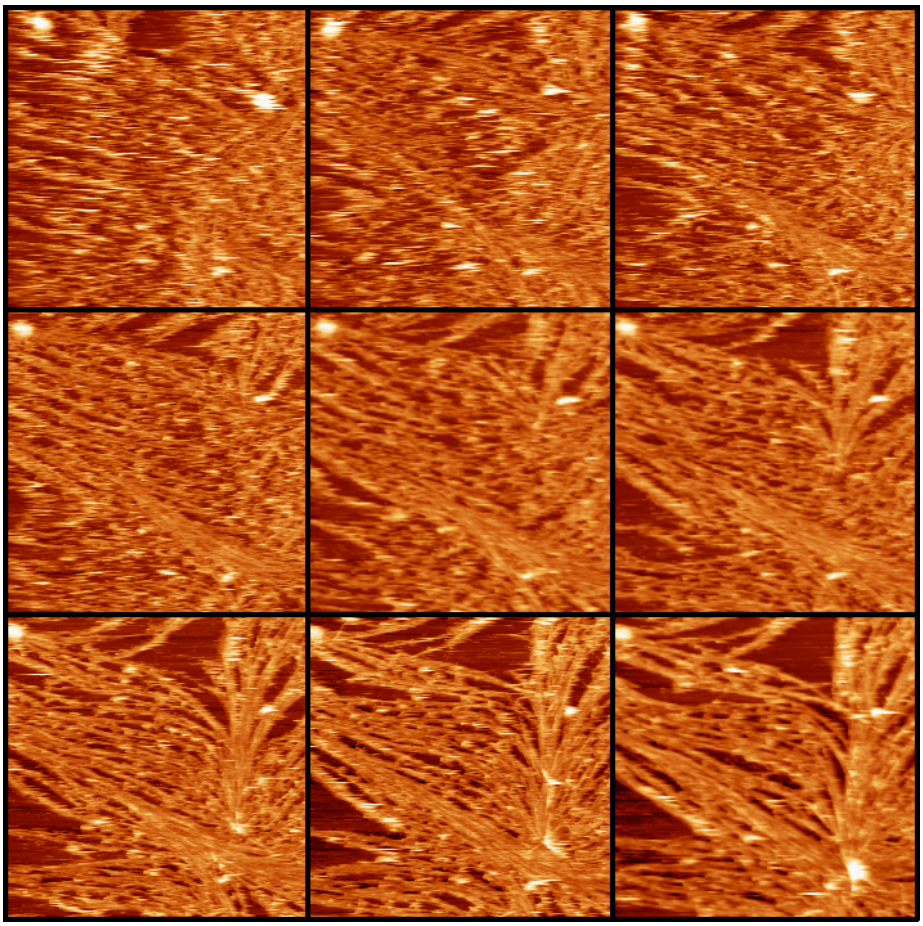

Figure 5.13 – Video S6a FtsZ-ZipA bundles on EcPL bilayer in buffer at pH 7.5 in presence of GTP. Image size is 4.2 x 4.2 μm and time lapse between frames is $\sim$4 min

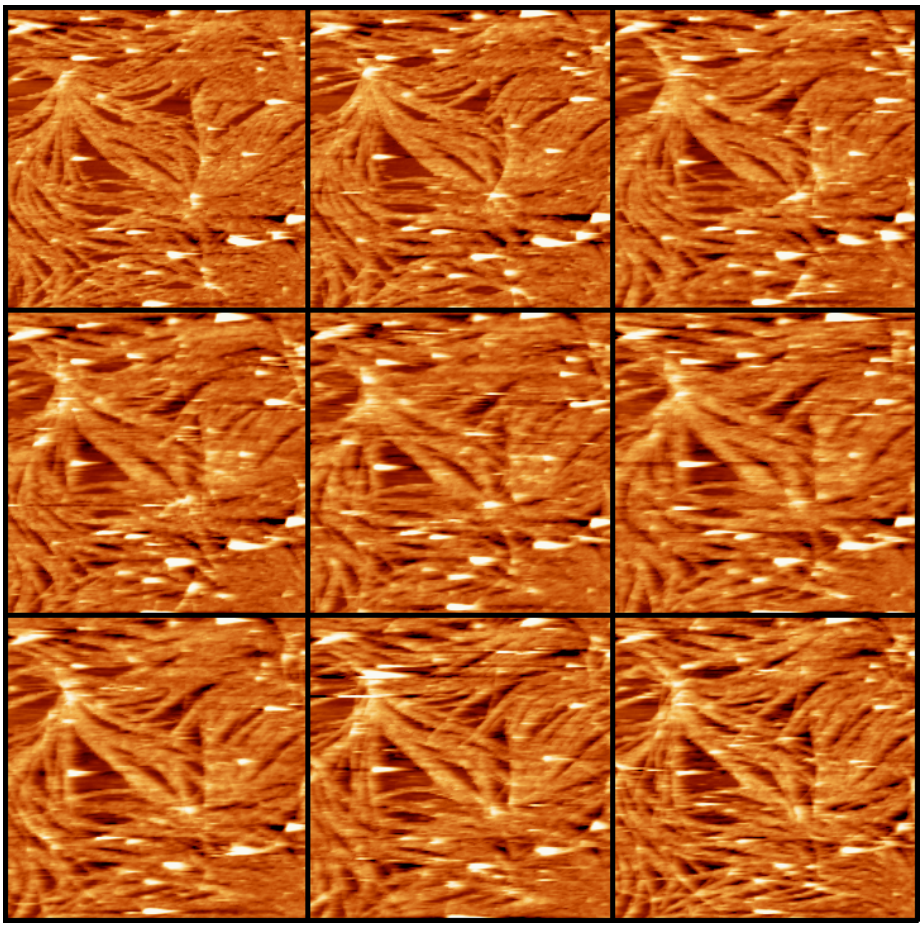

Figure 5.14 – Video S6b FtsZ-ZipA bundles on EcPL bilayer in buffer at pH 7.5 in presence of GTP. Image size is 9.4 x 9.4 μm and time lapse between frames is $\sim$4 min

Chapter 6

General Conclusions

In this PhD work we have looked at the structure and dynamics of filaments formed by the bacterial cell division protein FtsZ on 2D flat surfaces visualized with atomic force microscopy (AFM). The picture that emerges from AFM images is that filaments are highly dynamic exhibiting a rich structural polymorphism. We distinguish three hierarchical levels of organization. The simplest structures studied were single isolated protofilaments on mica. Larger protein surface density and lateral attraction between protofilaments led to the formation of aggregates and bundles. Finally, filaments aggregates might appeared interconnected forming networks. Interestingly, when FtsZ filaments were reconstituted onto lipid bilayers anchoring the polymers to the membrane through ZipA, a natural anchoring protein in the bacterial cell division machinery, also led to highly interconnected networks.

Sequences of AFM images registered in real-time under buffer solution allowed us to correlate structural information with dynamic behavior impossible to achieve simultaneously with other microscopes. Electron microscopy (EM) also provide high spatial resolution images able to discern FtsZ single stranded protofilaments but constitute a fixed snapshot of shapes and arrangements of FtsZ protofilaments and aggregates. EM images has been frequently complemented with spectroscopic techniques, such as light scattering or analytical ultracentrifugation, capable to follow in real-time the polymerization and aggregation of FtsZ but not a direct visualization of the structures formed. On the other hand, fluorescence microscopy is limited by light diffraction ($\sim 200\ nm$) and can not discern FtsZ

protofilaments.

6.1 FtsZ filament structures

AFM images of FtsZ filaments showed a rich structural polymorphism. FtsZ assembles into protofilaments, aggregates and networks. Surface density, ZipA and lipid composition were identified as modulators of the FtsZ filaments arrangements on 2D flat surfaces such as mica and supported lipid bilayers.

Comparison of AFM images with Monte Carlo simulations in Chapter 4 allowed to identify and estimate the interaction energies between FtsZ monomer that account for the structures observed experimentally. The basic features of the structural polymorphism of FtsZ filament arrangements are:

- **A strong polymeric bond with preferential curvature and high flexibility, and a weak lateral attraction govern the structure of FtsZ filaments and aggregates.** A fine balance of this four parameters modulates the length, curvature and lateral aggregation of FtsZ filaments.

- **FtsZ filaments are plastic and malleable.** For a fixed value of longitudinal bond energy, curvature, and flexibility, and lateral attraction FtsZ filaments arrangement depends on the surrounding environment. Surface protein density constituted a constrain for FtsZ filament arrangement. A layer of parallel and straight filaments is observed at high surface coverage whereas single isolated rings are formed at low surface coverage.

Reconstitution of FtsZ onto membrane model system in chapter 5 led to information about the role played by ZipA and bilayer lipid composition presented as followed:

- **ZipA modulates the curvature of FtsZ bundles.** On flat surfaces, either on mica or on supported lipid bilayers (SLBs), the spontaneous curvature of FtsZ filaments is canceled or reduced by ZipA.

- **Lipid composition modulates the structure of FtsZ bundles anchored to SLBs through ZipA.** The height, curvature, and de-

gree of interconnection of FtsZ bundles depend on the absence or presence of *E. coli* natural lipids in the bilayer.

6.2 FtsZ filament dynamics

FtsZ exhibited frequents rupture and formation of its polymeric bond at the three different levels of structural organization,i.e. protofilaments, filament aggregates, and networks. After rupture, the open ends can reanneal forming a new polymeric bond or lead to the irreversible release of a filament fragment. Our data have provided relevant insights in the role played by FtsZ GTPase activity and nucleotide exchange in this process.

The simplicity of FtsZ single isolated protofilaments studied in chapter 3 allowed to identify the basic traits of FtsZ protofilament dynamics and establishing a model for the role played by nucleotide hydrolysis and exchange presented as followed:

- **Rupture of longitudinal bonds occurs at random locations along the protofilaments.** Fragmentation and reannealing of longitudinal bonds were direct visualized at random positions. A linear correlation between length and life-time of FtsZ rings was observed, i.e. larger rings are opened earlier than smaller rings, supporting that rupture events are not coupled through adjacent interfaces.

- **Irreversible rupture frequency of longitudinal bond is correlated with nucleotide hydrolysis.** Although we don't measure directly GTPase activity of FtsZ, our data supports that nucleotide hydrolysis favor the fragmentation of filaments.

- **There is a high nucleotide turnover along the protofilaments.** Hydrolysis rate in solution is much faster than rupture rate measured by AFM indicating that many hydrolysis and nucleotide turnover cycles might occur at the same monomer-monomer interface before leading to an irreversible bond breakage.

- **Depolymerization is a size biased process, i.e. the release of small fragments from the protofilament is enhanced.** A mismatched of head-to-tail geometry of FtsZ prevents the formation of a new longitudinal bond. After nucleotide hydrolysis, higher surface mobility of free ends of smaller fragments increases the probability of an irreversible rupture.

In summary, FtsZ filament dynamics is governed by a balance between nucleotide hydrolysis (related with longitudinal bond fragmentation) and nucleotide turnover (related with reannealing of longitudinal bonds). The strong influence of protein surface mobility on the reannealing implies a relationship between the stability with the shape of FtsZ protofilaments and aggregates, i.e. structures with open ends are less stable.

6.3 Perspective and implications

The curvature of FtsZ filaments has been largely discussed (see section 1.2.2 in chapter 1). Evolution of isolated protofilaments forming closed rings supports a small curvature around $\sim$ 2-3° between adjacent monomers in the presence of GTP. On the other hand, curvature of FtsZ filaments is clearly dependent on the surrounding environment. The high flexibility exhibited by FtsZ filaments accounts for this plasticity. Assuming that a FtsZ polymer chain is able to diffuse laterally on the mica, the simplest and least constrained shape of a filament would be open isolated protofilaments. In this framework, cyclation, lateral aggregation, and volume exclusion would constrain the filaments out of its preferential curvature. The presence of ZipA, both on mica or on lipid bilayers, also modulates the curvature of FtsZ bundles. Interestingly constrained filaments could constitute a mechanism of mechanical energy storing to produce the contractile force necessary for cell division *in vivo*.

FtsZ single isolated protofilaments exhibited a strong tendency to form stable closed rings that shrink quickly once opened. At the next hierarchical level of structural organization, FtsZ filaments form curved and straight aggregates. The rolled closed aggregates appeared to be more stable than curved and straight open bundles. In this case lateral arrangement would also reduce surface mobility of FtsZ filaments due to spatial exclusion, favoring nucleotide turnover and preventing longitudinal bond irreversible ruptures. Both filament networks formed on mica and onto lipid bilayers are highly interconnected.

Although FtsZ filaments forming the Z-ring *in vivo* are modulated by other proteins of bacterial cell division machinery, our structural and dynamic data suggests that FtsZ filaments would arrange in a continuous structure minimizing the open ends, instead of a Z-ring structure made of many short filaments maximizing the open ends.

Chapter 7

Conclusiones generales

En éste trabajo de tesis hemos estudiado la estructura y la dinámica de los filamentos formados por la proteína de división bacteriana FtsZ en superficies bidimensionales planas mediante microscopia de fuerza atómica (AFM). El panorama que emerge de las imágenes de AFM es el de filamentos altamente dinámicos con un gran polimorfismo. Distinguimos tres niveles de organización jerárquica. Las estructuras más simples estudiadas fueron protofilamentos individuales y aislados sobre mica. El incremento de la densidad superficial proteica y la atracción lateral entre los protofilamentos dio lugar a la formación de agregados. Finalmente, los agregados de filamentos pueden aparecer interconectados formando redes. Es interesante que los filamentos de FtsZ reconstituidos en bicapas lipídicas también dieron lugar a la formación de redes altamente interconectadas al ser anclados a la bicapa mediante ZipA, un anclaje natural presente en la maquinaria de división bacteriana.

Las secuencias de imágenes registradas en tiempo real en medio líquido nos han permitido correlacionar la información estructural con el comportamiento dinámico, imposible de conseguir simultáneamente con otros microscopios. La microscopia electrónica (EM) permite la obtención de imágenes de alta resolución espacial siendo posible distinguir los protofilamentos individuales de FtsZ pero suponen una foto fija de las formas y la distribución de los protofilamentos y los agregados de FtsZ. Frecuentemente, las imágenes de EM han sido complementadas con técnicas espectroscópicas, tales como la dispersión de luz o la ultracentrifugación analítica, capaces de seguir en tiempo real la polimerización y la agregación de FtsZ pero no de

visualizar directamente las estructuras formadas. Por otro lado, la microscopia de fluorescencia está limitada por la difracción de la luz ($\sim 200\ nm$) y es incapaz de discernir los protofilamentos individuales de FtsZ.

7.1 Estructura de los filamentos de FtsZ

Las imágenes de AFM de los filamentos de FtsZ mostraron un gran polimorfismo. FtsZ se ensambla en protofilamentos, agregados y redes. La densidad superficial de proteína, ZipA y la composición lipídica fueron identificados como moduladores de la distribución de los filamentos de FtsZ en superficies planas bidimensionales tales como mica y bicapas lipídicas ancladas.

La comparación de las imágenes de AFM con simulaciones de Monte Carlo (MC) en el capítulo 4 permitieron identificar y estimar las energías de interacción presentes entre los monómeros de FtsZ que explican las estructuras observadas experimentalmente. Las características básicas que explican el polimorfismo estructural de los filamentos de FtsZ son:

- **El enlace polimérico fuerte, con una curvatura preferente y alta flexibilidad, y una atracción lateral débil controlan la estructura de los filamentos y agregados de FtsZ.** El fino balance entre éstos cuatro parámetros modula la longitud, curvatura y agregación lateral de los filamentos de FtsZ.

- **Los filamentos de FtsZ son plásticos y maleables.** Para un valor fijo de la energía del enlace longitudinal, su curvatura y flexibilidad, y de la atracción lateral, la distribución de los filamentos de FtsZ depende del entorno que les rodea. La densidad superficial de proteína constituye una ligadura sobre la distribución de los filamentos de FtsZ. Para altos recubrimientos de la superficie se observa una capa de filamentos rectos y paralelos mientras que para bajos recubrimientos los filamentos de FtsZ forman anillos aislados.

La reconstitución de FtsZ sobre un sistema modelo de membrana en el capítulo 5 dio información sobre el papel que juega ZipA y la composición lipídica de la bicapa. Las conclusiones obtenidas se presentan a continuación:

- **ZipA modula la curvatura de los agregados de FtsZ.** En superficies planas, tanto sobre mica como sobre bicapas ancladas (SLBs),

se canceló o redujo la curvatura espontánea de los filamentos de FtsZ en presencia de ZipA.

- **La composición lipídica modula la estructura de los agregados de FtsZ anclados a SLBs a través de ZipA.** La altura, curvatura y el grado de interconexión de los agregados de FtsZ dependen de la ausencia o presencia de los lípidos de *E. coli* el las SLBs.

7.2 Dinámica de los filamentos de FtsZ

FtsZ muestra frecuentemente la ruptura y formación de su enlace polimérico en los tres diferentes niveles de organización estructural, i.e. protofilamentos, agregados de filamentos y redes de agregados. Después de una ruptura, los extremos abiertos pueden realinearse formando de nuevo el enlace polimérico o se puede dar lugar a la pérdida irreversible de un fragmento de filamento. Nuestros datos han proporcionado un conocimiento relevante en el papel que juegan la actividad GTPasa de FtsZ y el intercambio de nucleótido en éste proceso.

La simplicidad de los protofilamentos aislados e individuales de FtsZ estudiados en el capítulo 3 permitieron la identificación de los aspectos básicos de la dinámica de los protofilamentos de FtsZ estableciéndose un modelo para el papel jugado por la hidrólisis y el intercambio de nucleótido que se presenta a continuación:

- **La ruptura de los enlaces longitudinales ocurre en posiciones aleatorias a lo largo del protofilamento.** Se visualizó directamente la fragmentación y el realineamiento de los enlaces longitudinales en posiciones aleatorias. La correlación lineal entre la longitud y el tiempo de vida de los anillos de FtsZ, i.e. los anillos largos se abren antes que los anillos cortos, apoya que los eventos de ruptura no se encuentran acoplados a través de las interfaces adyacentes.

- **La ruptura irreversible del enlace longitudinal está correlacionada con la hidrólisis del nucleótido.** Aunque no medimos directamente la actividad GTPasa de FtsZ, nuestros datos apoyan que la hidrólisis del nucleótido favorece la fragmentación de los filamentos.

- **Hay un alto intercambio de nucleótido a lo largo de los protofilamentos.** La velocidad de hidrólisis en solución es mucho

mayor que la velocidad de fragmentación medida por AFM indicando que muchos ciclos de hidrólisis e intercambio de nucleótido pueden ocurrir en la misma interfaz monómero-monómero antes de dar lugar a una ruptura irreversible del enlace.

- **La despolimerización es un proceso sesgado por el tamaño, i.e. la pérdida de pequeños fragmentos del protofilamento está favorecida.** La pérdida de la orientación cabeza-cola de FtsZ previene la formación de un nuevo enlace longitudinal. Después de la hidrólisis del nucleótido, una mayor difusión lateral de los extremos abiertos de una interfaz monómero-monómero incrementa la probabilidad de ruptura de fragmentos más cortos.

En resumen, la dinámica de los filamentos de FtsZ está gobernada por un equilibrio entre la hidrólisis del nucleótido (relacionada con la fragmentación del enlace longitudinal) y el intercambio de nucleótido (relacionado con el realineamiento del enlace longitudinal). La fuerte influencia de la difusión lateral en el realineamiento implica una relación entre la estabilidad y la forma de los protofilamentos y los agregados de FtsZ, i.e. estructuras con extremos abiertos son menos estables.

7.3 Perspectiva e implicaciones

La curvatura de los filamentos de FtsZ ha sido largamente discutida (ver sección 1.2.2 en el capítulo 1). La evolución de protofilamentos aislados que forman anillos cerrados apoya una curvatura de $\sim$ 2-3° entre monómeros adyacentes en presencia de GTP. Por otra parte, la curvatura de los filamentos de FtsZ es claramente dependiente del entorno que les rodea. La alta flexibilidad que exhiben los filamentos de FtsZ explican ésta plasticidad. Asumiendo que un polímero de FtsZ es capaz de difundir lateralmente sobre la mica, la forma más simple y menos constreñida de un filamento sería un filamento aislado y abierto. En éste contexto, la el cierre en forma de anillo, la agregación lateral y la exclusión de volumen constreñirían los filamentos fuera de su curvatura preferente. La presencia de ZipA, tanto en mica o sobre bicapas lipídicas, también modulan la curvatura de los agregados de FtsZ. Es interesante resaltar que los filamentos constreñidos podrían constituir un mecanismo de almacenamiento de energía mecánica para producir la fuerza necesaria para la división celular *in vivo*.

Los protofilamentos aislados de FtsZ muestran una fuerte tendencia a formar anillos cerrados estables que despolimerizan rápidamente una vez abiertos. En el siguiente nivel jerárquico de organización estructural, los filamentos de FtsZ forman agregados curvos y rectos. Los agregados enrollados y cerrados son más estables que los agregados abiertos ya sean curvos o rectos. En éste caso la distribución lateral también reduciría la movilidad superficial de los filamentos de FtsZ debido a la exclusión espacial, favoreciendo el intercambio de nucleótido y evitando la ruptura irreversible de los enlaces longitudinales.

Aunque los filamentos de FtsZ que forman el anillo-Z *in vivo* son modulados por otras proteínas de la maquinaria de división celular bacteriana, nuestros datos estructurales y dinámicos sugieren una distribución de los filamentos en una estructura continua minimizando los extremos abiertos, en vez de un anillo-Z formado por muchos filamentos cortos maximizando los extremos abiertos.

Bibliography

[1] W. Margolin, "FtsZ and the division of prokaryotic cells and organelles.," *Nat Rev Mol Cell Biol*, vol. 6, pp. 862–871, Nov 2005.

[2] R. Carballido-López and J. Errington, "A dynamic bacterial cytoskeleton.," *Trends Cell Biol*, vol. 13, pp. 577–583, Nov 2003.

[3] D. W. Adams and J. Errington, "Bacterial cell division: assembly, maintenance and disassembly of the Z-ring.," *Nat Rev Microbiol*, vol. 7, pp. 642–653, Sep 2009.

[4] M. Vicente and A. I. Rico, "The order of the ring: assembly of *Escherichia coli* cell division components.," *Mol Microbiol*, vol. 61, pp. 5–8, Jul 2006.

[5] J. Löwe and L. A. Amos, "Crystal structure of the bacterial cell-division protein Ftsz.," *Nature*, vol. 391, pp. 203–206, Jan 1998.

[6] C. Lu, J. Stricker, and H. P. Erickson, "FtsZ from Escherichia coli, Azotobacter vinelandii, and Thermotoga maritima–quantitation, GTP hydrolysis, and assembly.," *Cell Motil Cytoskeleton*, vol. 40, no. 1, pp. 71–86, 1998.

[7] T. M. Sossong, M. R. Brigham-Burke, P. Hensley, and K. H. Pearce, "Self-activation of guanosine triphosphatase activity by oligomerization of the bacterial cell division protein FtsZ.," *Biochemistry*, vol. 38, pp. 14843–14850, Nov 1999.

[8] M. Tadros, J. M. González, G. Rivas, M. Vicente, and J. Mingorance, "Activation of the Escherichia coli cell division protein FtsZ by a low-affinity interaction with monovalent cations.," *FEBS Lett*, vol. 580, pp. 4941–4946, Sep 2006.

[9] J. Mendieta, A. I. Rico, E. López-Viñas, M. Vicente, J. Mingorance, and P. Gómez-Puertas, "Structural and functional model for ionic (K+/Na+) and ph dependence of GTPase activity and polymerization of FtsZ, the prokaryotic ortholog of tubulin.," *J Mol Biol*, vol. 390, pp. 17–25, Jul 2009.

[10] G. Rivas, A. López, J. Mingorance, M. J. Ferrándiz, S. Zorrilla, A. P. Minton, M. Vicente, and J. M. Andreu, "Magnesium-induced linear self-association of the FtsZ bacterial cell division protein monomer. The primary steps for FtsZ assembly.," *J Biol Chem*, vol. 275, pp. 11740–11749, Apr 2000.

[11] A. Mukherjee and J. Lutkenhaus, "Guanine nucleotide-dependent assembly of FtsZ into filaments.," *J Bacteriol*, vol. 176, pp. 2754–2758, May 1994.

[12] J. Mingorance, M. Tadros, M. Vicente, J. M. González, G. Rivas, and M. Vélez, "Visualization of single Escherichia coli FtsZ filament dynamics with atomic force microscopy.," *J Biol Chem*, vol. 280, pp. 20909–20914, May 2005.

[13] A. Mukherjee and J. Lutkenhaus, "Analysis of FtsZ assembly by light scattering and determination of the role of divalent metal cations.," *J Bacteriol*, vol. 181, pp. 823–832, Feb 1999.

[14] L. Romberg, M. Simon, and H. P. Erickson, "Polymerization of FtsZ, a bacterial homolog of tubulin. Is assembly cooperative?," *J Biol Chem*, vol. 276, pp. 11743–11753, Apr 2001.

[15] X. C. Yu and W. Margolin, "Ca2+-mediated GTP-dependent dynamic assembly of bacterial cell division protein FtsZ into asters and polymer networks *in vitro*.," *EMBO J*, vol. 16, pp. 5455–5463, Sep 1997.

[16] J. Löwe and L. A. Amos, "Helical tubes of FtsZ from *Methanococcus jannaschii*.," *Biol Chem*, vol. 381, no. 9-10, pp. 993–999, 2000.

[17] C. A. Hale, A. C. Rhee, and P. A. J. de Boer, "Zipa-induced bundling of FtsZ polymers mediated by an interaction between C-terminal domains," *Journal of Bacteriology*, vol. 182, pp. 5153–5166, Sept. 2000.

[18] J. M. González, M. Jiménez, M. Vélez, J. Mingorance, J. M. Andreu, M. Vicente, and G. Rivas, "Essential cell division protein FtsZ

assembles into one monomer-thick ribbons under conditions resembling the crowded intracellular environment.," *J Biol Chem*, vol. 278, pp. 37664–37671, Sep 2003.

[19] D. Popp, M. Iwasa, A. Narita, H. P. Erickson, and Y. Mada, "FtsZ condensates: an *in vitro* electron microscopy study.," *Biopolymers*, vol. 91, pp. 340–350, May 2009.

[20] C. Lu, M. Reedy, and H. P. Erickson, "Straight and curved conformations of FtsZ are regulated by GTP hydrolysis.," *J Bacteriol*, vol. 182, pp. 164–170, Jan 2000.

[21] R. Marrington, E. Small, A. Rodger, T. R. Dafforn, and S. G. Addinall, "Ftsz fiber bundling is triggered by a conformational change in bound GTP.," *J Biol Chem*, vol. 279, pp. 48821–48829, Nov 2004.

[22] S. Huecas and J. M. Andreu, "Energetics of the cooperative assembly of cell division protein FtsZ and the nucleotide hydrolysis switch.," *J Biol Chem*, vol. 278, pp. 46146–46154, Nov 2003.

[23] J. M. González, M. Vélez, M. Jiménez, C. Alfonso, P. Schuck, J. Mingorance, M. Vicente, A. P. Minton, and G. Rivas, "Cooperative behavior of Escherichia coli cell-division protein FtsZ assembly involves the preferential cyclization of long single-stranded fibrils.," *Proc Natl Acad Sci U S A*, vol. 102, pp. 1895–1900, Feb 2005.

[24] Y. Chen, K. Bjornson, S. D. Redick, and H. P. Erickson, "A rapid fluorescence assay for ftsz assembly indicates cooperative assembly with a dimer nucleus.," *Biophys J*, vol. 88, pp. 505–514, Jan 2005.

[25] K. A. Michie and J. Löwe, "Dynamic filaments of the bacterial cytoskeleton.," *Annu Rev Biochem*, vol. 75, pp. 467–492, 2006.

[26] A. Dajkovic and J. Lutkenhaus, "Z ring as executor of bacterial cell division.," *J Mol Microbiol Biotechnol*, vol. 11, no. 3-5, pp. 140–151, 2006.

[27] J. Mingorance, S. Rueda, P. Gómez-Puertas, A. Valencia, and M. Vicente, "*Escherichia coli* FtsZ polymers contain mostly GTP and have a high nucleotide turnover.," *Mol Microbiol*, vol. 41, pp. 83–91, Jul 2001.

[28] L. Romberg and T. J. Mitchison, "Rate-limiting guanosine 5'-triphosphate hydrolysis during nucleotide turnover by FtsZ, a prokaryotic tubulin homologue involved in bacterial cell division.," *Biochemistry*, vol. 43, pp. 282–288, Jan 2004.

[29] Y. Chen and H. P. Erickson, "FtsZ filament dynamics at steady state: subunit exchange with and without nucleotide hydrolysis.," *Biochemistry*, vol. 48, pp. 6664–6673, Jul 2009.

[30] E. Salvarelli, M. Krupka, G. Rivas, M. Vicente, and J. Mingorance, "Independence between GTPase active sites in the Escherichia coli cell division protein ftsz," *Febs Letters*, vol. 585, pp. 3880–3883, Dec. 2011.

[31] G. Fu, T. Huang, J. Buss, C. Coltharp, Z. Hensel, and J. Xiao, "In vivo structure of the E. coli FtsZ-ring revealed by photoactivated localization microscopy (PALM).," *PLoS One*, vol. 5, no. 9, p. e12682, 2010.

[32] H. P. Erickson, D. W. Taylor, K. A. Taylor, and D. Bramhill, "Bacterial cell division protein FtsZ assembles into protofilament sheets and minirings, structural homologs of tubulin polymers.," *Proc Natl Acad Sci U S A*, vol. 93, pp. 519–523, Jan 1996.

[33] M. Osawa, D. E. Anderson, and H. P. Erickson, "Reconstitution of contractile FtsZ rings in liposomes.," *Science*, vol. 320, pp. 792–794, May 2008.

[34] P. L. Navajas, G. Rivas, J. Mingorance, P. Mateos-Gil, I. Hrger, E. Velasco, P. Tarazona, and M. Vlez, "In vitro reconstitution of the initial stages of the bacterial cell division machinery.," *J Biol Phys*, vol. 34, pp. 237–247, Apr 2008.

[35] G. Binnig, H. Rohrer, C. Gerber, and E. Weibel, "Tunneling through a controllable vacuum gap," *Applied Physics Letters*, vol. 40, no. 2, pp. 178–180, 1982.

[36] G. Binnig, H. Rohrer, C. Gerber, and E. Weibel, "Surface studies by scanning tunneling microscopy," *Phys. Rev. Lett.*, vol. 49, pp. 57–61, Jul 1982.

[37] A. M. Baró, R. Miranda, J. Alamán, N. García, G. Binnig, H. Rohrer, C. Gerber, and J. L. Carrascosa, "Determination of surface topography of biological specimens at high resolution by scanning tunnelling microscopy.," *Nature*, vol. 315, no. 6016, pp. 253–254, 1985.

[38] G. Binnig, C. F. Quate, and C. Gerber, "Atomic force microscope," *Phys. Rev. Lett.*, vol. 56, pp. 930–933, Mar 1986.

[39] A. Engel, "Biological applications of scanning probe microscopes.," *Annu Rev Biophys Biophys Chem*, vol. 20, pp. 79–108, 1991.

[40] O. Marti, B. Drake, and P. K. Hansma, "Atomic force microscopy of liquid-covered surfaces: Atomic resolution images," *Applied Physics Letters*, vol. 51, no. 7, pp. 484–486, 1987.

[41] F. A. Schabert and A. Engel, "Reproducible acquisition of Escherichia coli porin surface topographs by atomic force microscopy.," *Biophys J*, vol. 67, pp. 2394–2403, Dec 1994.

[42] D. J. Müller, G. Bldt, and A. Engel, "Force-induced conformational change of bacteriorhodopsin.," *J Mol Biol*, vol. 249, pp. 239–243, Jun 1995.

[43] S. Scheuring, J. Seguin, S. Marco, D. Lvy, B. Robert, and J.-L. Rigaud, "Nanodissection and high-resolution imaging of the rhodopseudomonas viridis photosynthetic core complex in native membranes by afm. atomic force microscopy.," *Proc Natl Acad Sci U S A*, vol. 100, pp. 1690–1693, Feb 2003.

[44] S. Scheuring and J. N. Sturgis, "Chromatic adaptation of photosynthetic membranes.," *Science*, vol. 309, pp. 484–487, Jul 2005.

[45] S. García-Manyes, G. Oncins, and F. Sanz, "Effect of ion-binding and chemical phospholipid structure on the nanomechanics of lipid bilayers studied by force spectroscopy.," *Biophys J*, vol. 89, pp. 1812–1826, Sep 2005.

[46] P. J. de Pablo, I. A. T. Schaap, F. C. MacKintosh, and C. F. Schmidt, "Deformation and collapse of microtubules on the nanometer scale.," *Phys Rev Lett*, vol. 91, p. 098101, Aug 2003.

[47] C. Carrasco, A. Carreira, I. A. T. Schaap, P. A. Serena, J. Gómez-Herrero, M. G. Mateu, and P. J. de Pablo, "DNA-mediated

anisotropic mechanical reinforcement of a virus.," *Proc Natl Acad Sci U S A*, vol. 103, pp. 13706–13711, Sep 2006.

[48] M. Rief, M. Gautel, F. Oesterhelt, J. M. Fernandez, and H. E. Gaub, "Reversible unfolding of individual titin immunoglobulin domains by AFM.," *Science*, vol. 276, pp. 1109–1112, May 1997.

[49] M. Carrión-Vázquez, A. F. Oberhauser, S. B. Fowler, P. E. Marszalek, S. E. Broedel, J. Clarke, and J. M. Fernández, "Mechanical and chemical unfolding of a single protein: a comparison.," *Proc Natl Acad Sci U S A*, vol. 96, pp. 3694–3699, Mar 1999.

[50] P. Hinterdorfer and Y. F. Dufrêne, "Detection and localization of single molecular recognition events using atomic force microscopy.," *Nat Methods*, vol. 3, pp. 347–355, May 2006.

[51] F. Moreno-Herrero, M. de Jager, N. H. Dekker, R. Kanaar, C. Wyman, and C. Dekker, "Mesoscale conformational changes in the DNA-repair complex Rad50/Mre11/Nbs1 upon binding DNA.," *Nature*, vol. 437, pp. 440–443, Sep 2005.

[52] N. Kodera, T. Kinoshita, T. Ito, and T. Ando, "High-resolution imaging of myosin motor in action by a high-speed atomic force microscope.," *Adv Exp Med Biol*, vol. 538, pp. 119–127, 2003.

[53] P.-E. Milhiet, D. Yamamoto, O. Berthoumieu, P. Dosset, C. L. Grimellec, J.-M. Verdier, S. Marchal, and T. Ando, "Deciphering the structure, growth and assembly of amyloid-like fibrils using high-speed atomic force microscopy.," *PLoS One*, vol. 5, no. 10, p. e13240, 2010.

[54] T. Ando, "High-speed atomic force microscopy coming of age.," *Nanotechnology*, vol. 23, p. 062001, Feb 2012.

[55] J. Israelachvili, *Intermolecular and Surface Forces: Revised Third Edition*. Academic Press, Academic Press, 2011.

[56] B. Cappella and G. Dietler, "Force-distance curves by atomic force microscopy," *Surface Science Reports*, vol. 34, no. 13, pp. 1 – 104, 1999.

[57] G. Sauerbrey, "Verwendung von schwingquarzen zur wagung dunner schichten und zur mikrowagung," *Zeitschrift Fur Physik*, vol. 155, no. 2, pp. 206–222, 1959.

[58] C. Lu and A. Czanderna, *Applications of Piezoelectric Quartz Crystal Microbalances*. Methods and phenomena, their applications in science and technology, Elsevier Science Limited, 1984.

[59] T. Nomura and M. Okuhara, "Frequency shifts of piezoelectric quartz crystals immersed in organic liquids," *Analytica Chimica Acta*, vol. 142, no. 0, pp. 281 – 284, 1982.

[60] K. Keiji Kanazawa and J. G. Gordon II, "The oscillation frequency of a quartz resonator in contact with liquid," *Analytica Chimica Acta*, vol. 175, no. 0, pp. 99–105, 1985.

[61] S. J. Martin, V. E. Granstaff, and G. C. Frye, "Characterization of a quartz crystal microbalance with simultaneous mass and liquid loading," *Analytical Chemistry*, vol. 63, no. 20, pp. 2272–2281, 1991.

[62] M. V. Voinova, M. Rodahl, M. Jonson, and B. Kasemo, "Viscoelastic acoustic response of layered polymer films at fluid-solid interfaces: Continuum mechanics approach," *Physica Scripta*, vol. 59, no. 5, p. 391, 1999.

[63] W. Y. X. Peh, E. Reimhult, H. F. Teh, J. S. Thomsen, and X. Su, "Understanding ligand binding effects on the conformation of estrogen receptor alpha-DNA complexes: a combinational quartz crystal microbalance with dissipation and surface plasmon resonance study.," *Biophys J*, vol. 92, pp. 4415–4423, Jun 2007.

[64] T. H. Nguyen and M. Elimelech, "Adsorption of plasmid DNA to a natural organic matter-coated silica surface: kinetics, conformation, and reversibility.," *Langmuir*, vol. 23, pp. 3273–3279, Mar 2007.

[65] T. H. Nguyen and K. L. Chen, "Role of divalent cations in plasmid DNA adsorption to natural organic matter-coated silica surface.," *Environ Sci Technol*, vol. 41, pp. 5370–5375, Aug 2007.

[66] T. H. Nguyen and M. Elimelech, "Plasmid dna adsorption on silica: kinetics and conformational changes in monovalent and divalent salts.," *Biomacromolecules*, vol. 8, pp. 24–32, Jan 2007.

[67] C. R. Wittmer, J. A. Phelps, W. M. Saltzman, and P. R. V. Tassel, "Fibronectin terminated multilayer films: protein adsorption and cell attachment studies.," *Biomaterials*, vol. 28, pp. 851–860, Feb 2007.

[68] L. Scheideler, F. Rupp, H. P. Wendel, S. Sathe, and J. Geis-Gerstorfer, "Photocoupling of fibronectin to titanium surfaces influences keratinocyte adhesion, pellicle formation and thrombogenicity.," *Dent Mater*, vol. 23, pp. 469–478, Apr 2007.

[69] A. Welle, M. Krger, M. Dring, K. Niederer, E. Pindel, and I. S. Chronakis, "Electrospun aliphatic polycarbonates as tailored tissue scaffold materials.," *Biomaterials*, vol. 28, pp. 2211–2219, Apr 2007.

[70] A. A. Feiler, A. Sahlholm, T. Sandberg, and K. D. Caldwell, "Adsorption and viscoelastic properties of fractionated mucin (BSM) and bovine serum albumin (BSA) studied with quartz crystal microbalance (qcm-d).," *J Colloid Interface Sci*, vol. 315, pp. 475–481, Nov 2007.

[71] G. V. Lubarsky, M. R. Davidson, and R. H. Bradley, "Hydration-dehydration of adsorbed protein films studied by AFM and QCM-D.," *Biosens Bioelectron*, vol. 22, pp. 1275–1281, Feb 2007.

[72] C. A. Keller and B. Kasemo, "Surface specific kinetics of lipid vesicle adsorption measured with a quartz crystal microbalance.," *Biophys J*, vol. 75, pp. 1397–1402, Sep 1998.

[73] R. P. Richter, J. L. K. Him, B. Tessier, C. Tessier, and A. R. Brisson, "On the kinetics of adsorption and two-dimensional self-assembly of annexin A5 on supported lipid bilayers.," *Biophys J*, vol. 89, pp. 3372–3385, Nov 2005.

[74] R. P. Richter, K. K. Hock, J. Burkhartsmeyer, H. Boehm, P. Bingen, G. Wang, N. F. Steinmetz, D. J. Evans, and J. P. Spatz, "Membrane-grafted hyaluronan films: a well-defined model system of glycoconjugate cell coats.," *J Am Chem Soc*, vol. 129, pp. 5306–5307, May 2007.

[75] P. M. Wolny, S. Banerji, C. Gounou, A. R. Brisson, A. J. Day, D. G. Jackson, and R. P. Richter, "Analysis of CD44-hyaluronan interactions in an artificial membrane system: insights into the distinct binding properties of high and low molecular weight hyaluronan.," *J Biol Chem*, vol. 285, pp. 30170–30180, Sep 2010.

[76] N. B. Eisele, S. Frey, J. Piehler, D. Grlich, and R. P. Richter, "Ultrathin nucleoporin phenylalanine-glycine repeat films and their interac-

tion with nuclear transport receptors.," *EMBO Rep*, vol. 11, pp. 366–372, May 2010.

[77] A. C. Hillier and M. D. Ward, "Scanning electrochemical mass sensitivity mapping of the quartz crystal microbalance in liquid media," *Analytical Chemistry*, vol. 64, no. 21, pp. 2539–2554, 1992.

[78] Janshoff, Galla, and Steinem, "Piezoelectric mass-sensing devices as biosensors-an alternative to optical biosensors?," *Angew Chem Int Ed Engl*, vol. 39, pp. 4004–4032, Nov 2000.

[79] M. Rodahl, F. Hook, A. Krozer, P. Brzezinski, and B. Kasemo, "Quartz crystal microbalance setup for frequency and Q-factor measurements in gaseous and liquid environments," *Review of Scientific Instruments*, vol. 66, no. 7, pp. 3924–3930, 1995.

[80] H. L. Bandey, S. J. Martin, R. W. Cernosek, and A. R. Hillman, "Modeling the responses of thickness-shear mode resonators under various loading conditions," *Analytical Chemistry*, vol. 71, no. 11, pp. 2205–2214, 1999.

[81] M. Osawa and H. P. Erickson, "Inside-out Z-rings–constriction with and without GTP hydrolysis.," *Mol Microbiol*, vol. 81, pp. 571–579, Jul 2011.

[82] H. P. Erickson, "Modeling the physics of FtsZ assembly and force generation," *Proceedings of the National Academy of Sciences of the United States of America*, vol. 106, pp. 9238–9243, June 2009.

[83] J. F. Allard and E. N. Cytrynbaum, "Force generation by a dynamic Z-ring in Escherichia coli cell division," *Proceedings of the National Academy of Sciences of the United States of America*, vol. 106, pp. 145–150, Jan. 2009.

[84] G. Lan, B. R. Daniels, T. M. Dobrowsky, D. Wirtz, and S. X. Sun, "Condensation of Ftsz filaments can drive bacterial cell division.," *Proc Natl Acad Sci U S A*, vol. 106, pp. 121–126, Jan 2009.

[85] I. V. Surovtsev, J. J. Morgan, and P. A. Lindahl, "Kinetic modeling of the assembly, dynamic steady state, and contraction of the FtsZ ring in prokaryotic cytokinesis," *Plos Computational Biology*, vol. 4, p. e1000102, July 2008.

[86] A. Paez, P. Mateos-Gil, I. Hrger, J. Mingorance, G. Rivas, M. Vicente, M. Vlez, and P. Tarazona, "Simple modeling of ftsz polymers on flat and curved surfaces: correlation with experimental in vitro observations.," *PMC Biophys*, vol. 2, no. 1, p. 8, 2009.

[87] B. Ghosh and A. Sain, "Origin of contractile force during cell division of bacteria.," *Phys Rev Lett*, vol. 101, p. 178101, Oct 2008.

[88] J. Mingorance, G. Rivas, M. Vélez, P. Gómez-Puertas, and M. Vicente, "Strong FtsZ is with the force: mechanisms to constrict bacteria," *Trends In Microbiology*, vol. 18, pp. 348–356, Aug. 2010.

[89] S. X. Sun, S. Walcott, and C. W. Wolgemuth, "Cytoskeletal crosslinking and bundling in motor-independent contraction," *Current Biology*, vol. 20, pp. R649–R654, Aug. 2010.

[90] E. Fischer-Friedrich and N. Gov, "Modeling FtsZ ring formation in the bacterial cell-anisotropic aggregation via mutual interactions of polymer rods.," *Phys Biol*, vol. 8, p. 026007, Apr 2011.

[91] D. A. Drew, G. A. Koch, H. Vellante, R. Talati, and O. Sanchez, "Analyses of mechanisms for force generation during cell septation in Escherichia coli," *Bulletin of Mathematical Biology*, vol. 71, pp. 980–1005, May 2009.

[92] A. Mukherjee and J. Lutkenhaus, "Dynamic assembly of FtsZ regulated by GTP hydrolysis.," *EMBO J*, vol. 17, pp. 462–469, Jan 1998.

[93] A. Paez, P. Tarazona, P. Mateos-Gil, and M. Vélez, "Self-organization of curved living polymers: Ftsz protein filaments," *Soft Matter*, vol. 5, no. 13, pp. 2625–2637, 2009.

[94] F. Moreno-Herrero, P. J. de Pablo, R. Fernández-Sánchez, J. Colchero, J. Gómez-Herrero, and A. M. Baró, "Scanning force microscopy jumping and tapping modes in liquids," *Applied Physics Letters*, vol. 81, pp. 2620–2622, Sept. 2002.

[95] L. Hamon, D. Panda, P. Savarin, V. Joshi, J. Bernhard, E. Mucher, A. Mechulam, P. A. Curmi, and D. Pastre, "Mica surface promotes the assembly of cytoskeletal proteins," *Langmuir*, vol. 25, pp. 3331–3335, Mar. 2009.

[96] A. A. Hyman, S. Salser, D. N. Drechsel, N. Unwin, and T. J. Mitchison, "Role of GTP hydrolysis in microtubule dynamics - information from a slowly hydrolyzable analog, gmpcpp," *Molecular Biology of the Cell*, vol. 3, pp. 1155–1167, Oct. 1992.

[97] I. Hörger, E. Velasco, J. Mingorance, G. Rivas, P. Tarazona, and M. Vélez, "Langevin computer simulations of bacterial protein filaments and the force-generating mechanism during cell division," *Physical Review E*, vol. 77, p. 011902, Jan. 2008.

[98] S. Huecas, C. Schaffner-Barbero, W. Garcia, H. Yebenes, J. M. Palacios, J. F. Diaz, M. Menendez, and J. M. Andreu, "The interactions of cell division protein FtsZ with guanine nucleotides," *Journal of Biological Chemistry*, vol. 282, pp. 37515–37528, Dec. 2007.

[99] F. Martín-García, E. Salvarelli, J. I. Mendieta-Moreno, M. Vicente, J. Mingorance, J. Mendieta, and P. Gómez-Puertas, "Molecular dynamics simulation of GTPase activity in polymers of the cell division protein FtsZ.," *FEBS Lett*, vol. 586, pp. 1236–1239, Apr 2012.

[100] R. H. Wade, "On and around microtubules: An overview," *Molecular Biotechnology*, vol. 43, pp. 177–191, Oct. 2009.

[101] H. Y. Kueh and T. J. Mitchison, "Structural plasticity in actin and tubulin polymer dynamics," *Science*, vol. 325, pp. 960–963, Aug. 2009.

[102] P. Mateos-Gil, I. Mrquez, P. Lpez-Navajas, M. Jimnez, M. Vicente, J. Mingorance, G. Rivas, and M. Vlez, "Ftsz polymers bound to lipid bilayers through zipa form dynamic two dimensional networks.," *Biochim Biophys Acta*, vol. 1818, pp. 806–813, Mar 2012.

[103] J. Stricker, P. Maddox, E. D. Salmon, and H. P. Erickson, "Rapid assembly dynamics of the Escherichia coli Ftsz-ring demonstrated by fluorescence recovery after photobleaching," *Proceedings of the National Academy of Sciences of the United States of America*, vol. 99, pp. 3171–3175, Mar. 2002.

[104] I. Hörger, E. Velasco, G. Rivas, M. Vélez, and P. Tarazona, "Ftsz bacterial cytoskeletal polymers on curved surfaces: the importance of lateral interactions.," *Biophys J*, vol. 94, pp. L81–L83, Jun 2008.

[105] F. Gittes, B. Mickey, J. Nettleton, and J. Howard, "Flexural rigidity of microtubules and actin filaments measured from thermal fluctuations in shape.," *J Cell Biol*, vol. 120, pp. 923–934, Feb 1993.

[106] A. Dajkovic, G. Lan, S. X. Sun, D. Wirtz, and J. Lutkenhaus, "MinC spatially controls bacterial cytokinesis by antagonizing the scaffolding function of FtsZ.," *Curr Biol*, vol. 18, pp. 235–244, Feb 2008.

[107] G. Lan, A. Dajkovic, D. Wirtz, and S. X. Sun, "Polymerization and bundling kinetics of Ftsz filaments.," *Biophys J*, vol. 95, pp. 4045–4056, Oct 2008.

[108] N. Dyer, "Tubulin and its prokaryotic homologue FtsZ: a structural and functional comparison," *Science Progress*, vol. 92, pp. 113–137, July 2009.

[109] N. W. Goehring, M. D. Gonzalez, and J. Beckwith, "Premature targeting of cell division proteins to midcell reveals hierarchies of protein interactions involved in divisome assembly," *Molecular Microbiology*, vol. 61, no. 1, pp. 33–45, 2006.

[110] S. Pichoff and J. Lutkenhaus, "Unique and overlapping roles for ZipA and FtsA in septal ring assembly in Escherichia coli," *Embo Journal*, vol. 21, pp. 685–693, Feb. 2002.

[111] M. E. G. Aarsman, A. Piette, C. Fraipont, T. M. F. Vinkenvleugel, M. Nguyen-Disteche, and T. den Blaauwen, "Maturation of the Escherichia coli divisome occurs in two steps," *Molecular Microbiology*, vol. 55, pp. 1631–1645, Mar. 2005.

[112] C. A. Hale and P. A. J. de Boer, "Recruitment of ZipA to the septal ring of Escherichia coli is dependent on FtsZ and independent of FtsA," *Journal of Bacteriology*, vol. 181, pp. 167–176, Jan. 1999.

[113] C. A. Hale and P. A. J. deBoer, "Direct binding of FtsZ to ZipA, an essential component of the septal ring structure that mediates cell division in E. coli," *Cell*, vol. 88, pp. 175–185, Jan. 1997.

[114] S. Pichoff and J. Lutkenhaus, "Tethering the Z-ring to the membrane through a conserved membrane targeting sequence in FtsA," *Molecular Microbiology*, vol. 55, pp. 1722–1734, Mar. 2005.

[115] S. A. Haney, E. Glasfeld, C. Hale, D. Keeney, Z. Z. He, and P. de Boer, "Genetic analysis of the Escherichia coli FtsZ center dot ZipA interaction in the yeast two-hybrid system - characterization of FtsZ residues essential for the interactions with ZipA and with FtsA," *Journal of Biological Chemistry*, vol. 276, pp. 11980–11987, Apr. 2001.

[116] L. Mosyak, Y. Zhang, E. Glasfeld, S. Haney, M. Stahl, J. Seehra, and W. S. Somers, "The bacterial cell-division protein ZipA and its interaction with an FtsZ fragment revealed by X-ray crystallography," *Embo Journal*, vol. 19, pp. 3179–3191, July 2000.

[117] T. Ohashi, C. A. Hale, P. A. J. de Boer, and H. P. Erickson, "Structural evidence that the P/Q domain of ZipA is an unstructured, flexible tether between the membrane and the C-terminal FtsZ-binding domain," *Journal of Bacteriology*, vol. 184, pp. 4313–4315, Aug. 2002.

[118] Z. Liu, A. Mukherjee, and J. Lutkenhaus, "Recruitment of ZipA to the division site by interaction with FtsZ," *Molecular Microbiology*, vol. 31, pp. 1853–1861, Mar. 1999.

[119] F. J. Moy, E. Glasfeld, L. Mosyak, and R. Powers, "Solution structure of ZipA, a crucial component of Escherichia coli cell division," *Biochemistry*, vol. 39, pp. 9146–9156, Aug. 2000.

[120] H. P. Erickson, "The FtsZ protofilament and attachment of ZipA - structural constraints on the FtsZ power stroke," *Current Opinion In Cell Biology*, vol. 13, pp. 55–60, Feb. 2001.

[121] K. Matsumoto, J. Kusaka, A. Nishibori, and H. Hara, "Lipid domains in bacterial membranes," *Molecular Microbiology*, vol. 61, pp. 1110–1117, Sept. 2006.

[122] C. R. H. Raetz and W. Dowhan, "Biosynthesis and function of phospholipids in Escherichia coli," *Journal of Biological Chemistry*, vol. 265, pp. 1235–1238, Jan. 1990.

[123] A. Martos, C. Alfonso, P. López-Navajas, R. Ahijado-Guzman, J. Mingorance, A. P. Minton, and G. Rivas, "Characterization of self-association and heteroassociation of bacterial cell division proteins FtsZ and ZipA in solution by composition gradient-static light scattering," *Biochemistry*, vol. 49, pp. 10780–10787, Dec. 2010.

[124] R. Richter, A. Mukhopadhyay, and A. Brisson, "Pathways of lipid vesicle deposition on solid surfaces: A combined QCM-D and AFM study," *Biophysical Journal*, vol. 85, pp. 3035–3047, Nov. 2003.

[125] Y. Chen and H. P. Erickson, "Rapid in vitro assembly dynamics and subunit turnover of ftsz demonstrated by fluorescence resonance energy transfer.," *J Biol Chem*, vol. 280, pp. 22549–22554, Jun 2005.

[126] H. Celia, E. Wilson-Kubalek, R. A. Milligan, and L. Teyton, "Structure and function of a membrane-bound murine MHC class I molecule," *Proceedings of the National Academy of Sciences of the United States of America*, vol. 96, pp. 5634–5639, May 1999.

[127] T. Ohashi, S. D. Galiacy, G. Briscoe, and H. P. Erickson, "An experimental study of GFP-based FRET, with application to intrinsically unstructured proteins," *Protein Science*, vol. 16, no. 7, pp. 1429–1438, 2007.

[128] J. Löwe, "Crystal structure determination of FtsZ from Methanococcus jannaschii," *Journal of Structural Biology*, vol. 124, pp. 235–243, Dec. 1998.

[129] D. J. Montefusco, A. E. Asinas, and R. M. Weis, "Liposome-mediated assembly of receptor signaling complexes.," *Methods Enzymol*, vol. 423, pp. 267–298, 2007.

[130] S. Tzlil and A. Ben-Shaul, "Flexible charged macromolecules on mixed fluid lipid membranes: Theory and Monte Carlo simulations," *Biophysical Journal*, vol. 89, pp. 2972–2987, Nov. 2005.

[131] S. Tzlil, D. Murray, and A. Ben-Shaul, "The "electrostatic-switch" mechanism: Monte Carlo study of MARCKS-membrane interaction," *Biophysical Journal*, vol. 95, pp. 1745–1757, Aug. 2008.

[132] Q. M. Yi and J. Lutkenhaus, "The nucleotide-sequence of the essential cell-division gene ftsz of Escherichia coli," *Gene*, vol. 36, no. 3, pp. 241–247, 1985.

[133] G. Lan, B. R. Daniels, T. M. Dobrowsky, D. Wirtz, and S. X. Sun, "Condensation of FtsZ filaments can drive bacterial cell division," *Proceedings of the National Academy of Sciences of the United States of America*, vol. 106, pp. 121–126, Jan. 2009.

[134] H. P. Erickson, D. E. Anderson, and M. Osawa, "Ftsz in bacterial cytokinesis: Cytoskeleton and force generator all in one," *Microbiology and Molecular Biology Reviews*, vol. 74, pp. 504–528, Dec. 2010.

[135] R. Shlomovitz and N. S. Gov, "Membrane-mediated interactions drive the condensation and coalescence of FtsZ rings.," *Phys Biol*, vol. 6, no. 4, p. 046017, 2009.